

Summary

This thesis is part of a project within the formula student organization, Revolve NTNU. The project's aim is to find out how compliance in the suspension system plays a role towards the overall performance of the vehicle, in competition. This thesis is a continuation of the work done during the fall of 2018 by the 2019 Revolve NTNU team. This can be read about in the project thesis: "*Validation of Finite Element Analysis using strain gauges, of the suspension system of a Formula student car*" [1]. In the project thesis, an effort was made to compare finite element analysis to real values in race conditions. The project showed that a holistic comparison, looking at the entire car, is unfeasible, and a more simplistic approach is needed to fully understand the errors in the results obtained. In this master thesis, a single suspension member has been evaluated with finite element analysis, and compared to experimental tensile test data. It has aided the identification of deviations between experiment and simulation. Strain data showed a deviation ranging from 12,6% to 48,8% at a maximum load of 7 kN. Load-displacement data was shown to deviate with 12% at 7 kN.

An attempt has been made to analyze the effects of compliance through a model, named *the compliance model*. The compliance model uses the results from the aforementioned FE-model, of the single suspension member, and estimates the change in the wheel angles, camber and toe. The FE-model of the suspension rod has been deemed too uncertain, thus not obtaining any results from the compliance model.

Note

All paragraphs directly quoted from the project thesis: "*Validation of Finite Element Analysis using strain gauges, of the suspension system of a Formula student car*" have [1] stated in the section title. These sections are also indented towards the middle of the page.

Preface

This thesis marks the end of my two years at NTNU, which in reality have been more like two years at Revolve NTNU. I want to thank the organization and all people involved the past two years. It has truly been the most rewarding years towards the completion of my degree.

Contents

Abstract	i
List of Figures	ix
List of Tables	x
Abbreviations	xi
1 Introduction	1
1.1 Goals and Limitations	2
2 Theory and Background	3
2.1 Suspension Members	3
2.1.1 A-Arm Assemblies	5
2.2 Spherical bearings	7
2.3 Carbon fibre reinforced polymer composites	8
2.3.1 Material properties of CFRP composites	9
2.3.2 Filament Winding	11
2.3.3 Winding Pattern and Layup	12
2.4 Joining of CFRP and Aluminium	13
2.4.1 Adhesive Bonding	13
2.4.2 Mechanics of Adhesion	13
2.5 Compliance and Vehicle Control [1]	15
2.5.1 Camber Angle[1]	16
2.5.2 Toe Angle [1]	17
2.5.3 Force paths	18
2.5.4 Tire Behaviour	20
3 State of the Art	21
3.1 Modelling of spherical plain bearings	21
3.2 Modelling of CFRP composites	22
3.3 Modelling of adhesive joints	23
4 Methods	25
4.1 Finite element modelling of A-arm	26

4.2	Modelling of Strain Gauges	27
4.3	Tensile Testing of Rods	28
4.3.1	Mounting of strain gauges	30
4.3.2	Load application and data analysis	31
4.4	Compliance Model	32
4.5	FE-modelling of the Compliance Model	33
5	Results	34
5.0.1	Summary	38
6	Discussion	39
6.1	Main Findings	39
6.2	A-arm finite element model	39
6.2.1	CFRP Rod modelling	39
6.2.2	Spherical Bearing modelling	41
6.2.3	Adhesive joint modelling	43
6.3	Experiment	43
7	Conclusion and Future Work	45
7.1	Conclusion	45
7.1.1	Compliance FEA	46
7.2	Future Work	46
7.2.1	Testing of CFRP rod	46
7.2.2	Testing of spherical bearing	46
7.2.3	Strain Gauge Use	46
Appendix		52
A	A-Arm Finite Element Model	53
A.1	Parts	53
A.2	Material Properties	55
A.3	CFRP material properties	55
A.4	CFRP Layup	56
A.5	Assembly and steps	58
A.6	Interaction	60
A.7	Loads and Boundary Conditions	63

A.8	Mesh	66
A.9	Results	68
B	The Compliance Model	70
B.1	Input Variables	70
B.2	mainRearLocal_Condition.py	72
B.3	functionsRearLocal_Condition.py	73
C	Data sheets	78
C.1	T700s Fiber	78
C.2	UF3369 Resin	78
C.3	Araldite 4859	78
C.4	HBM Quantum MX1615	78
C.5	TML FLAB-3-11-3LJCT-F	78
C.6	ASKF GE8C	78
C.7	Sarma XRL	78
D	Project Thesis	93

List of Figures

1.1	The 2019 contender, Nova	2
2.1	Suspension members	3
2.2	In-wheel suspension design	4
2.3	A-arm rods	6
2.4	A-arm bonding surfaces	6
2.5	Spherical bearing in angle lock	6
2.6	Lower rear aft A-arm member	6
2.7	Spherical bearing	7
2.8	Cut section of spherical plain bearing	7
2.9	Woven vs.unidirectional [6]	8
2.10	Unidirectional composite cross section [3]	8
2.11	Micro-mechanical model simplification of UD composite [3]	9
2.12	Filament winding process [7]	11
2.13	Winding patterns [8]	12
2.14	Contact angle of a droplets [11]	13
2.15	Adsorption [11]	14
2.16	Diffusion [11]	14
2.17	Rear toe compliance in FS-car [15]	15
2.18	Camber and toe angle [16]	16
2.19	Illustration of the castor trail and pneumatic trail [17]	18
2.20	Top view - Toe angle change with longitudinal load application	19
2.21	Rear view - Camber angle change due to lateral load application	19
2.22	Slip angle = 8 degrees	20
3.1	Contact area of Revolve 2019 angle lock	23
3.2	Simplified shear approach [25]	24
3.3	Differential shear approach [25]	24
4.1	Work flow	25
4.2	A-arm assembly in Abaqus CAE	26
4.3	Simplified FE-model for strain gauge placement	27
4.4	Instron 1342	28
4.5	HBM 1615 data aquisition unit	28
4.6	Equipment used for testing	29
4.7	Strain gauge bonded to angle lock	30

4.8	Load application 7000 N	30
4.9	Identified data points plotted in orange for waned load in orange	31
4.10	A-arm member as springs in series model	32
4.11	Model of suspension with members as springs. The a-arms and the tie rod can be seen in pink. The wheel assembly can be seen as the dashed lines	33
5.1	Raw load-displacement curves. A drift in zero point is observed	34
5.2	Angle lock strain gauge results at each load level. A small offset in the load increment of 1 kN is observed.	35
5.3	Rod strain gauge results at each load level. A small offset in the load increment of 1 kN is observed.	35
5.4	Rod end strain gauge results at each load level. A small offset in the load increment of 1 kN is observed.	36
5.5	Load-displacement comparison, error ranging from -6% to 12 %	36
5.6	Angle lock strain gauge comparison, error ranging from 7,1 % to 19,4% . . .	37
5.7	Rod strain gauge comparison, error ranging -44,2% to -54,4%	37
5.8	Rod end strain comparison, error ranging from 18,7 % to 48,8%	38
6.1	Displacement vs. shifting of ply layup angle from 6°to 14°	40
6.2	Displacement vs. adding one ply at the time extra to the layup	41
6.3	Only clevis and insert rod end was assembled. 6,8 kN of preload was applied. load was set to 7 kN	42
6.4	The zero point for the load-displacements have been adjusted	43
7.1	Expanding Arbor assembly	47
7.2	Advised test method to determine compliance in spherical bearing	48
A.1	Geometry simplification	53
A.2	Parts in simulation	54
A.3	Layup in Abaqus CAE	56
A.4	Rod layup CSYS and ply stack plot	57
A.5	Assembly of A-arm rod in Abaqus CAE	58
A.6	Steps	58
A.7	Step settings	59
A.8	Contact behaviour	60
A.9	Tie Constraints	61
A.10	Kinematic coupling	62
A.11	Bolt Load	63

A.12 Clevis BC	64
A.13 Retaining ring BC	65
A.14 Meshed assembly	66
A.15 Refinement around clevis hole	67
A.16 Displacement along rod axis 7 kN load applied	68
B.1 Suspension pickup points	71

List of Tables

4.1	A-arm in tensile test machine	29
4.2	Assembly steps of A-arm assembly	29
A.1	Material properties	55
A.2	Material properties CFRP rod	55
A.3	Layup orientation for CFRP rod	56
A.4	Mesh characteristics of assembly	66
B.1	Loads at contact patch	70
B.2	Stiffness values for suspension members	70

Abbreviations

CAD	Computer Aided Design
CAE	Computer Aided Engineering
DAQ	Data Acquisition
FE	Finite Element
FEA	Finite Element Analysis
FS	Formula Student
FSG	Formula Student Germany
ODB	Output Data Base
SAE	Soceiety Of Automotive Engineers
SG	Strain Gauge

1 Introduction

This master thesis is written as an embedded project within Revolve NTNU, a *formula student (FS)* organization. Formula Student is the worlds largest engineering competition for students. The competition is now at a level where each incremental performance gain is of the outmost importance. Revolve NTNU was in 2018 one of the top teams with a second place at the most prestigious competition, Formula Student Germany (FSG).

The key to the success of Revolve NTNU, is the focus on designing and building components in-house, and to not rely on external suppliers. Every year, more competence is built up by tailoring mechanical parts, high voltage electronics and software. The overall goal is to get a holistic understanding of the car, and how performance can be gained. A strong tie between fundamental theoretical knowledge and how it can be applied in praxis is indispensable in this regard.

Quoted from the project thesis [1]:

Since the start of the organization, a hard question to answer has been: "How stiff is stiff enough?". Stiffness is a sought after characteristic in motor sport, as lack thereof can be a major troublemaker when it comes to vehicle handling and control. An increase in stiffness is often closely related to an increase in weight. An increase in weight is a direct performance parameter. A higher weight will require an increase in force to accelerate the vehicle. To answer the question stated, a foundation must be laid. This thesis will act as a starting point for the work in answering this question.

Based on work done in the project thesis [1], it was found beneficial to simplify the approach. In the project thesis an attempt was made to compare FE-models of different suspension components to experimental values. These experimental values were obtained by making a custom force applicator, and applying controlled loads at the wheel. Strain gauges were attached to the components of interest. A simplification to this approach was needed, as it was hard identify what caused erroneous results. Some factors which made for these uncertainties were: tolerances in self made equipment, inexperience with strain gauges and a large number of components in the experiment.

1.1 Goals and Limitations

It has been decided to focus on a smaller part of the suspension assembly, and conduct testing with professional lab equipment. To continue the work done towards answering the question stated in the quote above, and the work done in the project thesis, the following goals have been set:

- Test and validate suspension members from one corner of the car, using strain gauges and a tensile test machine
- Compare results to FE model and define deviations/impacts to experiments
- Create method for calculating compliance in suspension members
- **Bonus:** Find camber and toe variation due to suspension members compliance on one corner of the vehicle

It was found out at an early stage that validating and testing all members from one corner of the car would be time consuming, and yield no real benefit towards completing the goals set in the thesis. The decision was made to test one member in one load direction, and make an approach applicable to the other suspension members.



Figure 1.1: The 2019 contender, Nova.

2 Theory and Background

2.1 Suspension Members

Suspension members connect the wheel assembly (tire, rim, upright, motor) to the monocoque. See figure. 2.1 The suspension members used by Revolve NTNU have since 2014 been made from *carbon fibre reinforced polymer (CFRP)* rods bonded together with aluminium. Depending on the suspension member, these aluminium parts vary in geometry. There are in total three different types of members at each corner of the vehicle. These can be seen illustrated in figure. 2.1.

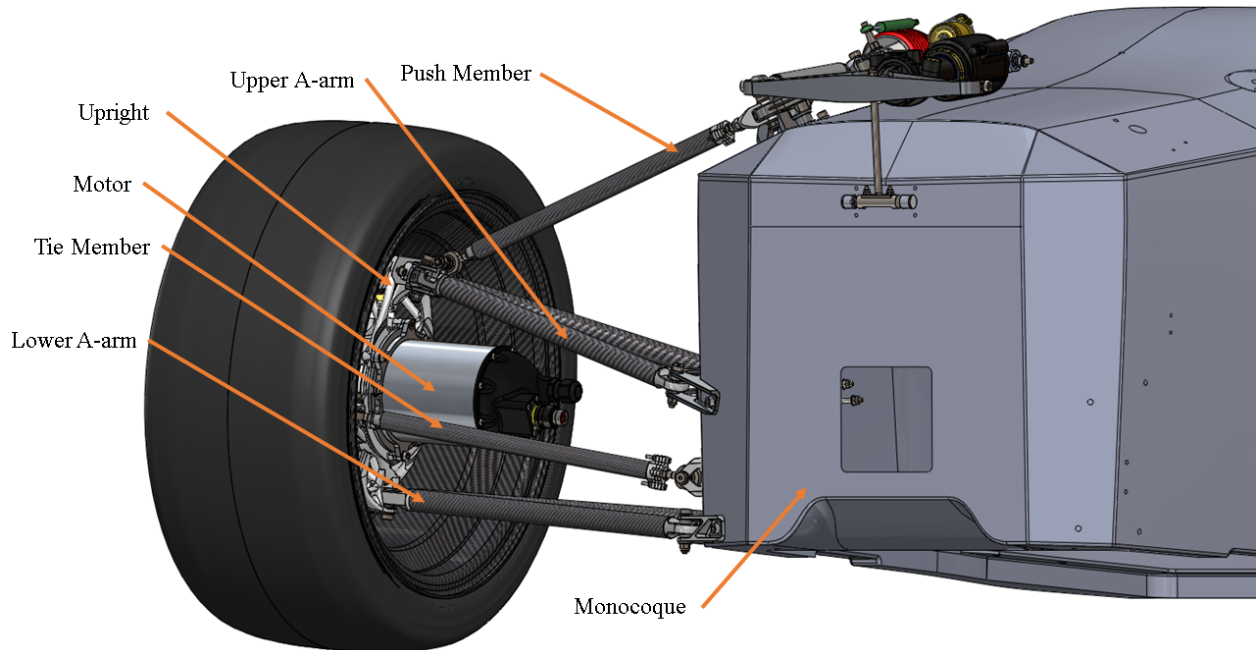


Figure 2.1: Suspension members

2. THEORY AND BACKGROUND

In figure. 2.2, the in-wheel assembly is presented (without the wheel). This shows how the suspension members interact with the adjacent assemblies. The upright is at the center of the in-wheel assembly. It functions as a gearbox housing, motor/brake mounting point and a junction point for all suspension members.

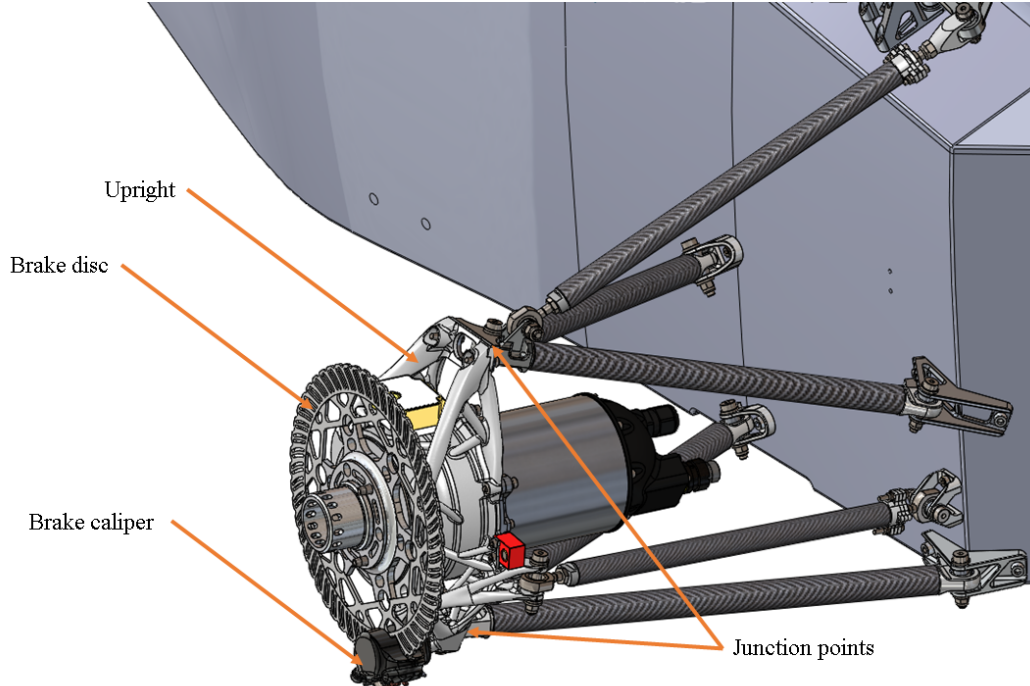


Figure 2.2: In-wheel suspension design

All of the suspension members work together to control the movement of the wheels, as designed by the vehicle dynamics engineers. How each rod handles the forces can be read in section 2.5.

2.1.1 A-Arm Assemblies

There are two A-Arm assemblies at each corner of the car, upper and lower. The A-Arms are connected to the uprights (top and bottom) at one end, and to the monocoque chassis at the other end. See figure. 2.1. At the upright, the A-arm assembly is connected via an *angle lock*. The angle lock is a junction point for each A-arm. The angle locks vary in size and shape depending on their location on the car. The angle lock also functions as a housing for a *spherical bearing*. The angle lock is bonded together with two CFRP rods. These rods connect to their *insert rod ends* each, which in turn connect to brackets each. The insert rod end also houses a spherical bearing. Both spherical bearings are retained by a circlip. The brackets serve as the final load bearing structure before the chassis. See figure. 2.2. The A-arms are the only rod assemblies where no adjustments can be made after their manufacturing. How the A-arms handles the forces applied can be read about in section 2.6. The A-arms are the main subject for experiment and FE-modelling. This is because the A-arm members are thought to be the greatest contributor to compliance of the three suspension members. The most important reasons are:

- Members absorb the highest forces
- Are the longest members in the suspension system.
- The A-arm count on the car totals in eight rods, compared to four tie members and four push rods. This means a greater benefit for the team in gaining knowledge on these assemblies.

The lower aft A-arm has been chosen for further investigation. See figure. 2.6. The choice to use this member for testing was made based on it being the only member available at the time of testing. The rest of the member had been assembled to the 2019 vehicle.

Three different sections of the A-arm have been chosen as areas of interest:

- Spherical Bearings.
- CFRP rod.
- Adhesive joint.

These areas have been chosen based on the limited knowledge of modelling these parts and their behaviour, within Revolve NTNU. It was also noticed that in the case of the spherical bearings, limited literature found.

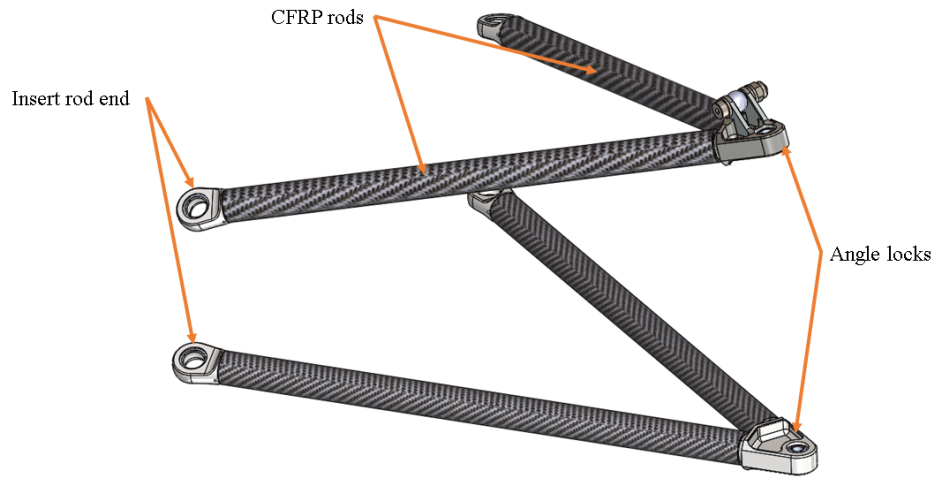


Figure 2.3: A-arm rods



Figure 2.4: A-arm bonding surfaces

Figure 2.5: Spherical bearing in angle lock



Figure 2.6: Lower rear aft A-arm member

2.2 Spherical bearings

As mentioned, each end of the A-arm houses a *spherical bearing*, also known as a *spherical plain bearing*. A spherical bearing is a mechanical component consisting of an inner ring with a spherical convex outer diameter, and an outer ring with an adjacent concave inner diameter [2]. There are two main types of spherical bearings, *maintenance free* and regular. In this thesis the maintenance free spherical bearing will be further discussed. The spherical bearings let suspension members articulate, without transferring any moment through the intended suspension motion. The spherical bearings used by Revolve NTNU in the A-arm assembly are called *SKF GE8C* and *Sarma XRL 6*.



Figure 2.7: Spherical bearing

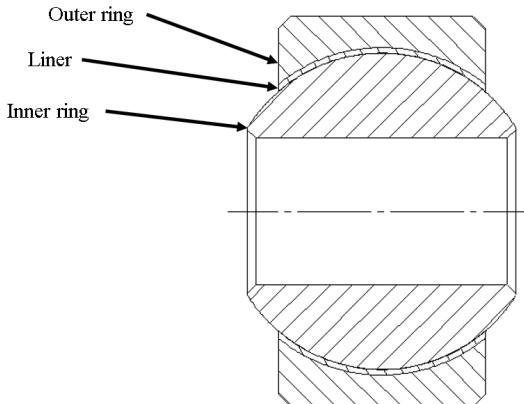


Figure 2.8: Cut section of spherical plain bearing

The housing and the outer ring of the spherical plain bearing is made from hardened steel. There is a low-friction layer separating them. This surface is usually referred to as a *liner*. The liner employed by the spherical bearings varies in material. The liner yields a coefficient of friction between 0.05-0.25 [2]. Dependent on the manufacture, the bearing liner can be made of different materials. Composite materials are often observed. The GE8C bearing is made with a PTFE-Bronze sintered lining, while the XRL bearing is made using a special PTFE-Resin liner [2]

2.3 Carbon fibre reinforced polymer composites

Carbon fibre reinforced polymer composites (CFRP composites) consists of two or more materials. These are often referred to as phases. In this thesis the CFRP composite will consist of a carbon fibre phase and an epoxy resin phase, the latter often referred to as the *epoxy matrix*. [3]. The suspension rods are made up of *unidirectional (UD)* fibres arranged in a specific *winding pattern*. The difference between UD fibres and other woven fibres can be seen in figure. 2.9. The UD fibre sheet has all its fibres aligned in one direction, while the woven fibre has a 90 degree pattern, usually called a *weave*. With UD fibres, parts can gain a higher stiffness and strength value in the required direction [4] [5]. This comes at a low weight penalty, since the fibres can be oriented as the designer's intend. This is the main reason UD carbon composites make for a good choice for making the suspension rods.

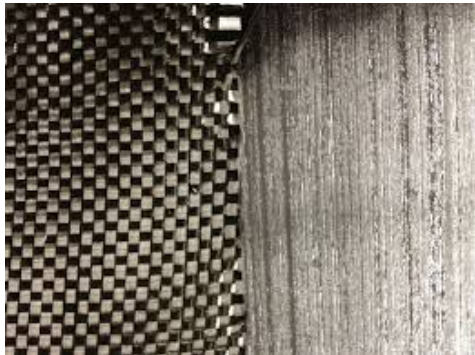


Figure 2.9: Woven vs.unidirectional [6]

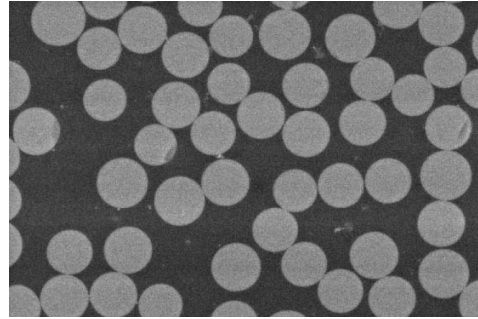


Figure 2.10: Unidirectional composite cross section [3]

The fibres in a UD composite are randomly distributed in the epoxy matrix (figure. 2.10, with some areas more packed with fibres than others [3]. This can greatly affect the material properties. The amount of epoxy vs. fibre is also the fundamental factor for how the composite material constants are calculated.

2.3.1 Material properties of CFRP composites

The calculations of the material properties of the composite starts by establishing the correct amount of fibre vs. epoxy in the composite in terms of volume i.e. *the volume fraction*. This is done by first calculating the *fibre volume fraction* and the *matrix volume fraction*. This is done through equations 1 and 2 [3].

$$V_f + V_m = 1 \quad (1) \quad V_f = \frac{m_f * \rho_m}{m_f * \rho_m + m_m * \rho_f} \quad (2)$$

This leads to the use of micro-mechanical models which uses the volume fraction of fibre and epoxy to estimate *longitudinal modulus*, *transverse modulus*, *poisson ratio* and *shear modulus*. The model uses traditional stress-strain relationship to derive these material properties. These models are simplifications and make assumptions surrounding how the fibres are oriented in the epoxy matrix [3].

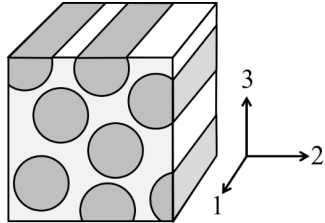


Figure 2.11: Micro-mechanical model simplification of UD composite [3]

An assumption is made that the strain in the matrix and fibre is equal to the overall strain in the composite.

$$\epsilon_{1f} = \epsilon_{1m} = \epsilon_1 \quad (3)$$

A force F_1 will be distributed between the fibre and the matrix, resulting in the following distribution:

$$F_1 = F_{1f} = F_{1m} \quad (4)$$

This equates to the following in equation 5 with stress and cross sectional area.

$$\begin{aligned} A\sigma_1 &= A_f\sigma_{1f} + A\sigma_{1m} \\ \sigma_1 &= \frac{A_f}{A}\sigma_{1f} + \frac{A_m}{A}\sigma_{1m} = V_f\sigma_{1f} + V_m\sigma_{1m} \end{aligned} \quad (5)$$

This can be rewritten by Hook's law for definition of modulus to yield the longitudinal modulus E_1

$$\begin{aligned} \frac{\sigma_1}{\epsilon_1} &= V_f \frac{\sigma_{1f}}{\epsilon_1} + V_m \frac{\sigma_{1m}}{\epsilon_1} = V_f \frac{\sigma_{1f}}{\epsilon_{1f}} + V_m \frac{\sigma_{1m}}{\epsilon_{1m}} \\ E_1 &= V_f E_{f1} + V_m E_m \\ E_1 &= V_f E_{f1} + (1 - V_f)E_m \end{aligned} \quad (6)$$

The most simple approach to finding the transverse modulus is to assume that the strain in the composite is the same in the fibre and matrix. This gives equation 7

$$\begin{aligned} \frac{1}{E_2} &= \frac{V_f}{E_{f2}} + \frac{1 - V_f}{E_m} \\ E_2 &= \frac{E_{2f}E_m}{V_fE_m + V_mE_{2f}} \end{aligned} \quad (7)$$

This equation tends to underestimate the value significantly. This leads to a modification of the matrix modulus according to equation 8. Where E' is the modified modulus and v_m is the poisons ratio of the matrix.

$$E' = \frac{E_m}{1 - v_m^2} \quad (8)$$

This gives the equation for the transverse modulus :

$$E_2 = \frac{E_{2f}E'_m}{V_fE_m + V_mE_{2f}} \quad (9)$$

Poisson's ratio v_{12} and shear modulus (G_{12}) can like E_1 and E_2 be found through calculations. These are also good approximations compared to experimental testing.

$$v_{12} = V_f v_{12} + (1 - V_f) * v_M \quad (10)$$

$$G_{12} = \frac{G_{12} G_m}{V_f G_m + V_m G_{12f}} \quad (11)$$

2.3.2 Filament Winding

Filament winding (FW) is the preferred manufacturing technique for the suspension rods. FW is commonly used for fibre reinforced polymers, where axis symmetry is required. The process involves winding the fibre around a *mandrel*. The mandrels external shape determined the internal shape of the finished part. The process can be seen in fig (2.12). The fibre is pulled through a resin bath before being guided through the carriage and onto the mandrel, which is rotated by the drive box. The carriage can move from side to side making different winding angles onto the mandrel possible. By varying what angle the layers are wound onto the mandrel, the properties of the finished component can be varied. [7]

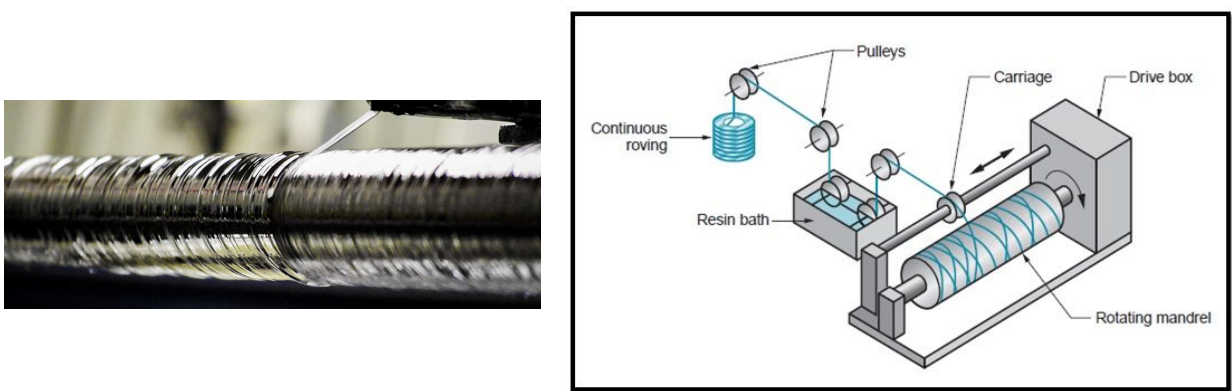


Figure 2.12: Filament winding process [7]

When the fibre is pulled through the epoxy resin in the manner described above, the process is given the name of *wet winding* or *wet impregnating* (wetpregging). The fibres can be impregnated with fibre before being wound. This is referred to as *prepreg winding*. [7]. The process used for the suspension rods is prepreg winding. The process is the same as for the wetpreg example, but without pulling the fibre through the epoxy resin. In some cases, the mandrel is pre-heated so the prepreg fibre sticks better.

2.3.3 Winding Pattern and Layup

There are three different winding patterns used in FW, *polar windings*, *helical windings* and *hoop windings*. Helical windings are made when the fibre is wound around the mandrel in a spiral fashion. The angle of the winding to the longitudinal axis is called the *helix angle*. When this angle approaches 90° the winding is called a *hoop winding*. Polar windings are obtained by winding the fibre as close to the longitudinal axis as possible [7]. Polar windings can not be wound perfectly parallel to the center axis, as the mandrel is fixed at each side in the spindle, and drive box.

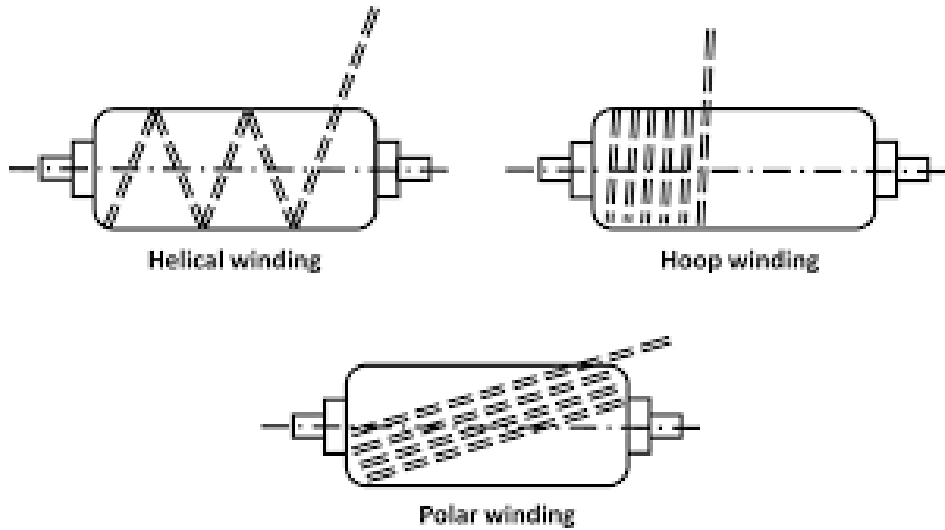


Figure 2.13: Winding patterns [8]

The suspension rods use a combination of hoop windings and polar windings. The main force carrier are the polar windings. The hoop windings are added to obtain some strength against crushing loads. This combination of windings is referred to as the *layup*. When modelling composites each winding will be referred to as one *ply*, thus making one layup consist of multiple plies.

2.4 Joining of CFRP and Aluminium

There are several ways of joining CFRP and aluminium components. The most common being adhesive bonding, self-piercing rivets, bolted connections and clinching [9]. The connection mentioned above are all suitable in joining of plated structures, but for joining of circular sections adhesive bonding is the most efficient and prevalent method.

2.4.1 Adhesive Bonding

Adhesive bonding is when two *adherents* (also known as *substrates*) are bonded together using an *adhesive* [7]. An adhesive is a non metallic substance, which is usually a polymer [7]. When an adhesive joint is made, a certain time period is required for the adhesive to react with the substrates. This time is referred to as *curing time*, and the process is referred to as *curing*.

2.4.2 Mechanics of Adhesion

A good adhesive joint will need an adhesive with a lower surface tension than that of CFRP and aluminium [9] [10]. This property will decide the wetting capabilities of the adhesive i.e. how the adhesive spreads out onto the adherents [11]. The general rule is to have the contact angle between the adhesive and the adherents of less than 90 degrees [11]. This is made such that the adhesive does not create droplets on the adherent, and thus does not uniformly spread onto the adherent, decreasing the strength of the joint.

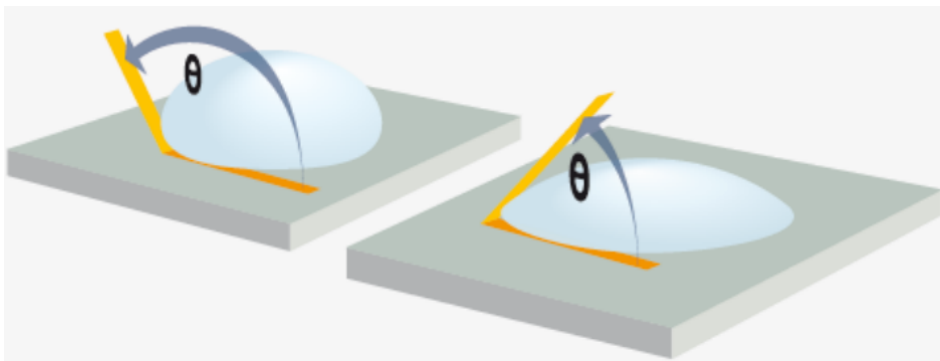


Figure 2.14: Contact angle of a droplets [11]

2. THEORY AND BACKGROUND

Among the most prevalent adhesion theories are: *adsorption*, *diffusion* and *mechanical locking* [9] [11]. In *adsorption theory* strong van der Waal and Lewis acid-base interactions occurs. How these bonds are made is largely dependent on the liquid-solid interaction of the adhesive and adherent. This is why good wetting capabilities are needed, as they determine how uniformly the adhesive is spread onto the adherent [11] [9]. In diffusion theory the adhesion strength is due to the diffusion of the adhesive into the adherent. In the case of CFRP joints, the polymer chains of the adhesive and that of the CFRP will diffuse into each other, essentially locking the two together. [9] [11].

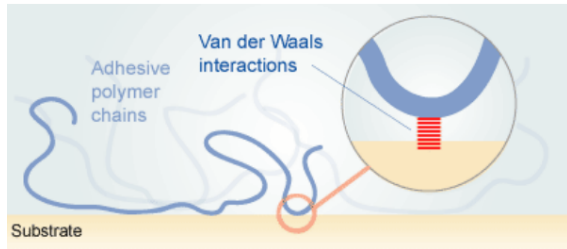


Figure 2.15: Adsorption [11]

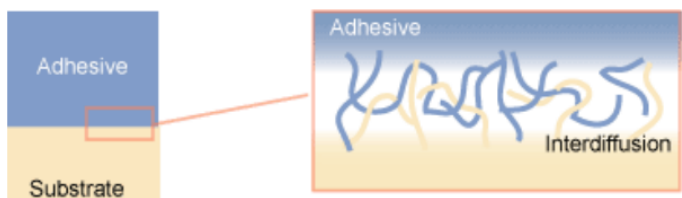


Figure 2.16: Diffusion [11]

2.5 Compliance and Vehicle Control [1]

Stiffness is defined as the ability of an elastic object to resist deformation under a given load. [12] Compliance is the inverse of stiffness [13]. As forces are reacted through the suspension, compliant effects occur. The different forces applied at the contact patch of the tire will result in deformation of various parts in the suspension system. This deformation accumulates and will alter the angle the tires have in relation to the ground. The two main compliant effects are stated below:

- Toe compliance (steer compliance) - Forces acting on the wheel affect the angle of the wheel relative to the direction of vehicle.
- Camber compliance - Change in camber angle of the wheel as forces act on it.

The different compliant effects can lead to *understeer* or *oversteer* in a vehicle. An easy way to think of this effect, is to visualize a car in a turn with fixed velocity and a slightly increasing acceleration. The driver must control the steering angle to keep a constant radius. Compliant understeer will make the vehicle travel along a larger circle [13]. For a driver, compliance can be a major issue in terms of vehicle control, this with special regard to rear toe compliance. Rear toe compliance can not be controlled by the driver. It is hard to quantify how big an influence it will have on performance, but it will lead to oversteer. Oversteer is a more unstable condition for the vehicle and driver control [14].



Figure 2.17: Rear toe compliance in FS-car [15]

It is important to add the following to the above paragraph: When the kinematic design of the suspension is done, the suspension members and parts are infinitely stiff. This will give inaccuracies which affect a wide range of systems. Torque vectoring, adaptive dampers, launch control are amongst these.

2.5.1 Camber Angle[1]

The camber angle is defined as the angle, ϕ , between a tilted wheel plane and the vertical. [13] A positive camber is described as the top of the wheel is tilting away from the vehicle, negative vice versa. Camber plays a role in force generation between the tire and the road as the tire will produce a force in the direction it is tilted. As the car goes through a turn the tire is subjected to a lateral force causing lateral tire wall deflection. As the side wall deflects in a negative cambered wheel, the deflection can zero out the positive camber and keep the wheel more perpendicular to the ground. Resulting in a maximization of lateral grip [16]. The opposite will result in a reduction in lateral grip.

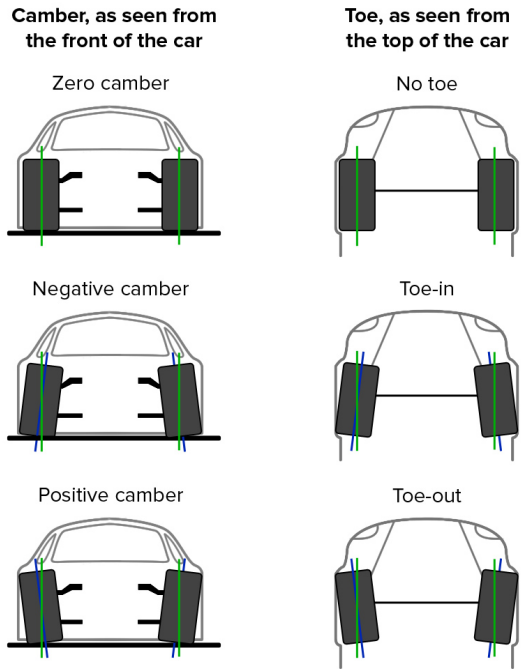


Figure 2.18: Camber and toe angle [16]

2.5.2 Toe Angle [1]

The toe angle is defined as the angle between the tires center plane as the tires are rotated around its center axis [16]. The toe angle is viewed from above, see fig. 2.18. A cambered tire will not follow a straight line as it is free rolled. Two tires angled with the same camber angle will create an equal force opposing each other. This will lead to a heat build up and excessive wear and tear of the tire [13]. An appropriate toe-out angle can negate these effects. Toeing of the rear wheels can be used to introduce under- or oversteer effects. Toe-out leads to oversteer and toe-in creates understeer [16].

2.5.3 Force paths

To understand what role the suspension rods play when forces are applied at the contact patch, two separate views have been chosen for illustrative purposes. Figure 2.20 shows the vehicle in top view. As a load is applied at the contact patch the A-arms reaction force can be seen. Compliance in these members will result in a toe angle change. In figure 2.21 a lateral load is applied. And showing the change in camber angle. When looking at the forces translated through the tie rod the contact patch needs to be looked at. Because of the offset between the upper and lower mounting point there is an offset between the axis through these two points and the center of the contact patch. This is referred to *castor trail*, or *mechanical trail*. Due to how the tire transfers load, *pneumatic trail* occurs. This phenomena takes place because the resultant force between the tire and the road is located offset by some distance rear of the geometrical contact patch of the tire [17]. More on the force paths can be read about in the project thesis [1].

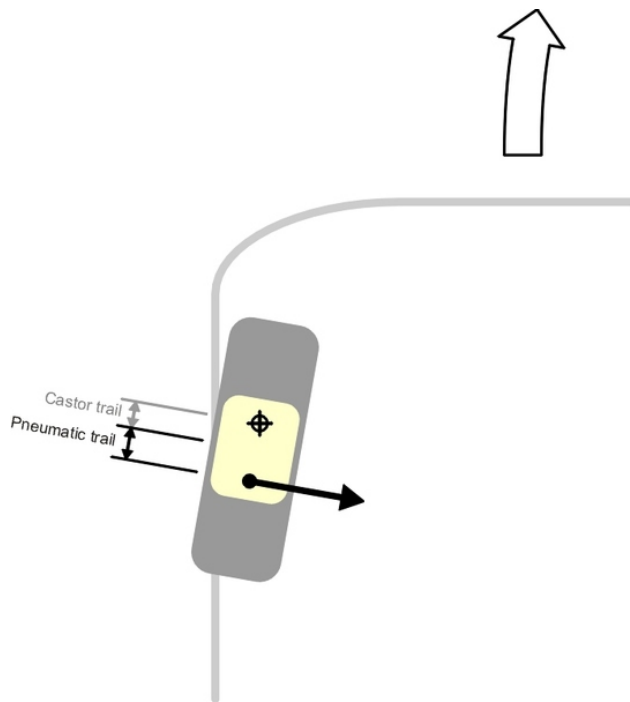


Figure 2.19: Illustration of the castor trail and pneumatic trail [17]

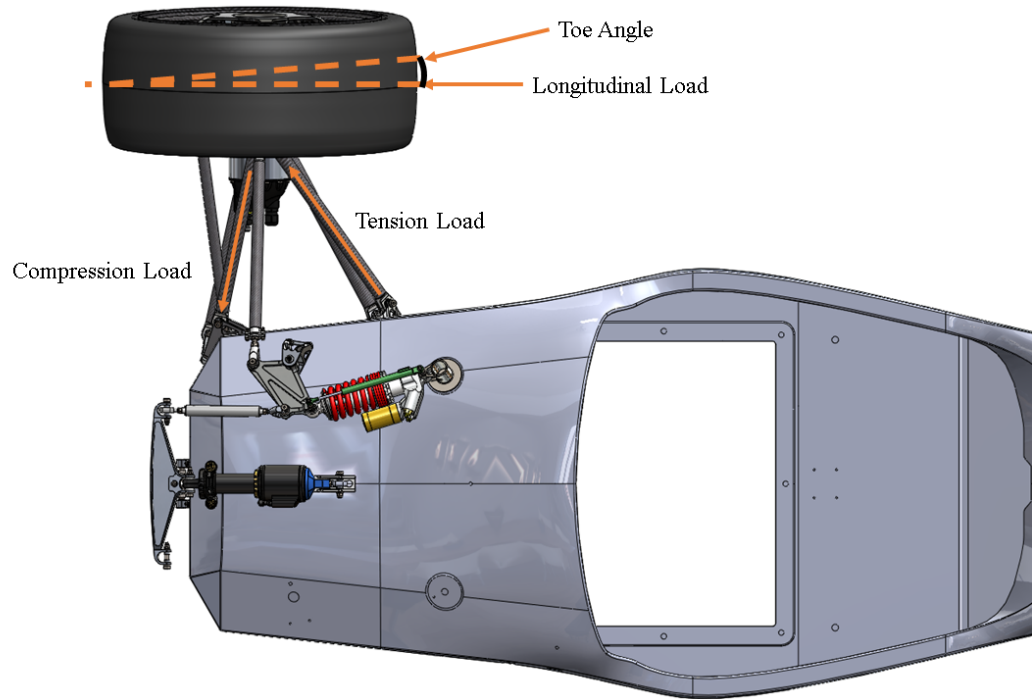


Figure 2.20: Top view - Toe angle change with longitudinal load application

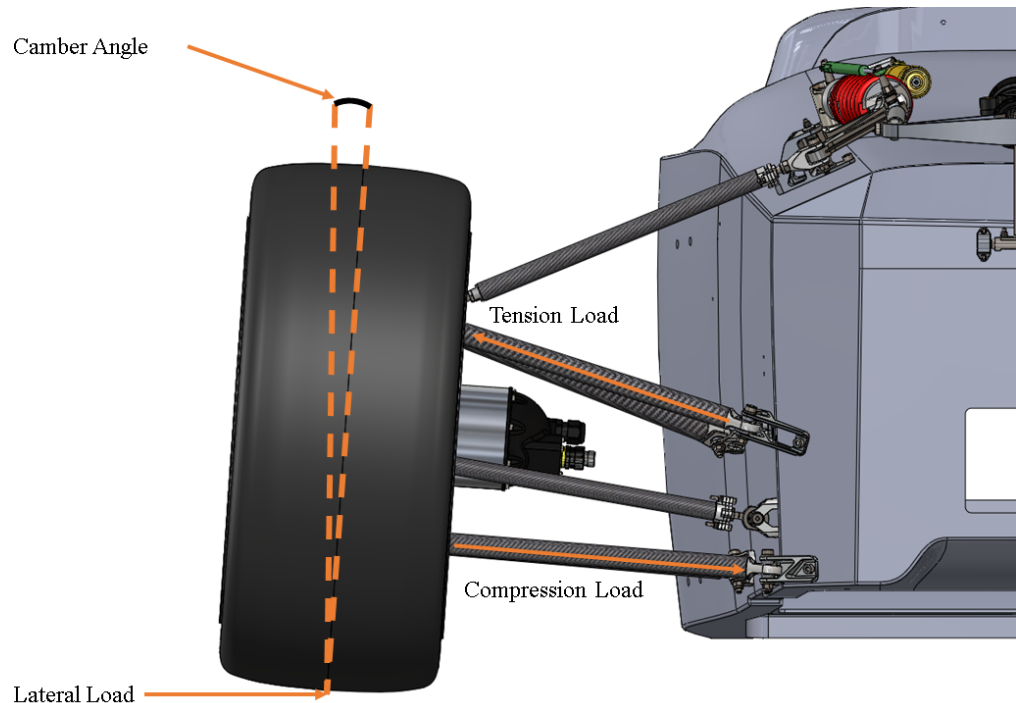


Figure 2.21: Rear view - Camber angle change due to lateral load application

2.5.4 Tire Behaviour

To evaluate the performance change due to compliance, tire properties and how the tires interact with the traction surface have been looked at. Compliance in the suspension system will result in camber and toe variations. The effects of camber variation is directly related to performance, as camber change will result in a change of the lateral force generation of the tires. This can be seen in figure 2.22. The graph has been generated using the Continental C19 FS tire documentation [18]. It shows how inclination angle affects the lateral load capacity of the tire, at differing normal loads (F_z). At a higher normal load, the effect of the inclination angle is greater. It is important to note that inclination angle γ is not the same as camber angle ϕ . Inclination angle is used when isolated tire testing is performed on tire testers [13]. The inclination angle is positive when the tire is tilted to the right when looking at the wheel from behind [13] [19]. This means that a tire tilted to the right on the left hand side of the car yields a *positive* inclination angle, but a *negative* camber angle. While on the right hand side, camber angle and inclination angle have the same sign. Performance affects of a toe angle change are harder to quantify, as these are greatly related to driver confidence and feeling.

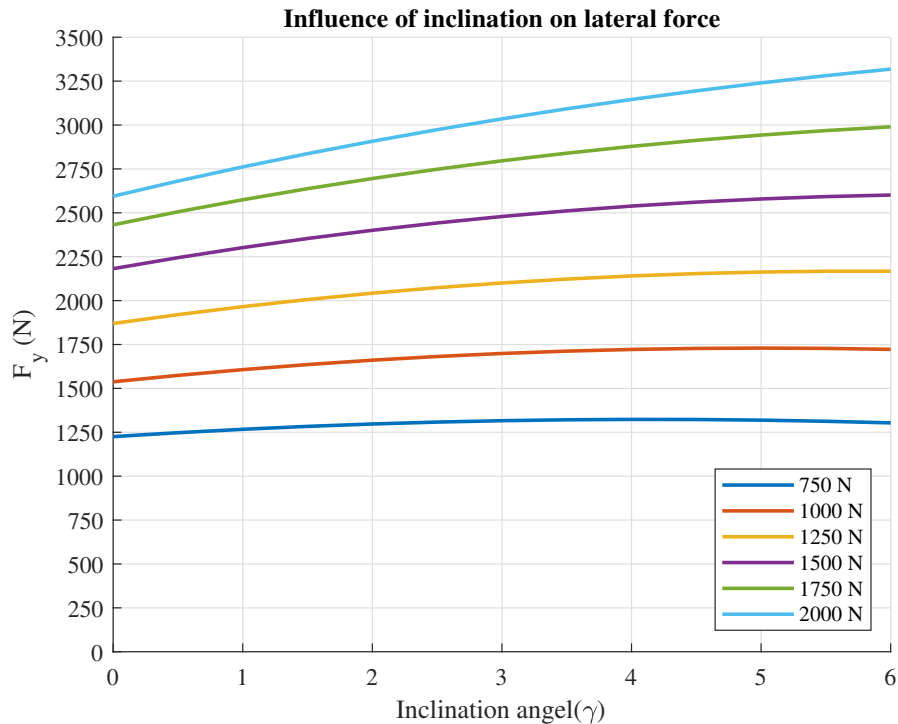


Figure 2.22: Slip angle = 8 degrees

3 State of the Art

This section will give an insight in the literature found surrounding the modelling of spherical bearings, composites and adhesives.

3.1 Modelling of spherical plain bearings

Analytical models for spherical bearings only exist for special cases [20]. This is greatly due to the mechanical properties of the liner in the spherical bearings. Yang et. al [21] showed the liner materials properties to be well fitting with a hyperelastic material model. This makes numerical models the best option for determining the behaviour of these mechanical components. Li et. al [20] presented results correlating FE-modelling and physical testing of spherical plain bearings. Their findings show a deviation of 5 % between experimental and simulated results, thus proving accurate simulations are obtainable. They obtained these results without modelling the liner. This is not a trivial simulation due to the fact that the material properties of the liner are not readily available. Nonlinear effects due to contact interaction between the parts add complexity. The liners' effect on the results was found to have substantial effect on contact stress in the study by Yang et. al [21]. They noted a difference in maximum contact stress of 240 MPa for a bearing with liner, compared to almost 550 MPa for a bearing without liner. In both papers, they do not state if the liner has any impact on the displacement of the component.

3.2 Modelling of CFRP composites

Although modelling of composites is more studied than the modelling of spherical bearings, it is still

Modelling of composite structures is done by applying *Classic laminate theory (CLT)*. CLT makes several assumptions simplifying the calculations of the composite. For the following assumption to be correct the length and width must be substantially greater than the thickness [22].

The following list of assumptions are quoted from the NTNU course "TMM4175 Polymer Composites" [3]:

- *Plys are perfectly bonded*
- *Each layer is homogeneous*
- *Individual layer properties can be isotropic, transverse or orthotropic*
- *Each layer is in a state of plane stress*
- *The laminate deforms according to Kirchoff assumptions.*

In FE-modelling of composites is greatly dependant on what kind of post-processing output is wanted. When looking at the composite at a *micromechanical level*, the composite needs to be described in terms of its composition and microstructure [22]. Results regarding the stress and strain internally in the epoxy matrix and fibres can be modeled at this level. This includes modelling of how the fibres are oriented in the composite, and what role this plays. At a *macromechanical level* (lamina level [22]) the above CLT assumptions are employed. Here the CFRP part can modelled with thin shell elements, disregarding transverse shear effects [22].

3.3 Modelling of adhesive joints

Although not thought to be a great contributor to the compliance in the member, the adhesive joints are an uncertainty and need closer attention. Dependent on what is wanted from the simulation, different levels of detail can be obtained [23] [24]. Analytical approaches are suitable for establishing early joint strength and making initial decisions regarding the joint. With regards to the A-Arms a suitable calculation is the shear stress equivalent of a single lap joint. $\tau = \frac{P}{DL}$ [25]. Where P is the applied load, D is the diameter of the rod and L is the length of the adhesive bonding surface. See 3.1.

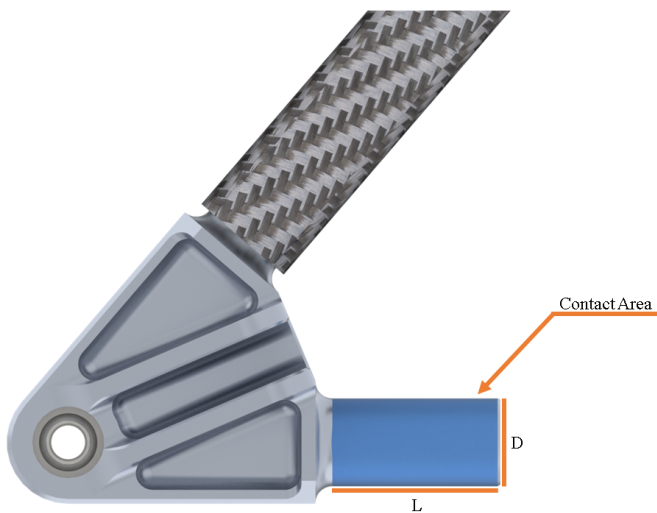


Figure 3.1: Contact area of Revolve 2019 angle lock

In this simplistic approach the adhesive is assumed to be deforming uniformly through the cross section. See figure . 3.2 This calculation can be interpreted as the average shear stress of the adhesive. This is not an accurate calculation as the adhesive deforms elastically [25]. See figure. 3.3.

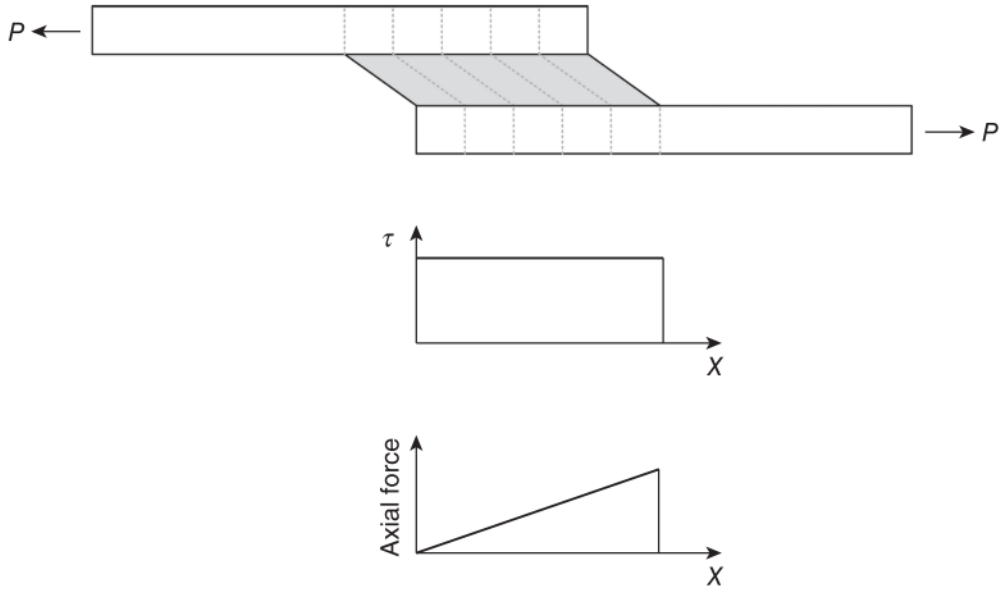


Figure 3.2: Simplified shear approach [25]

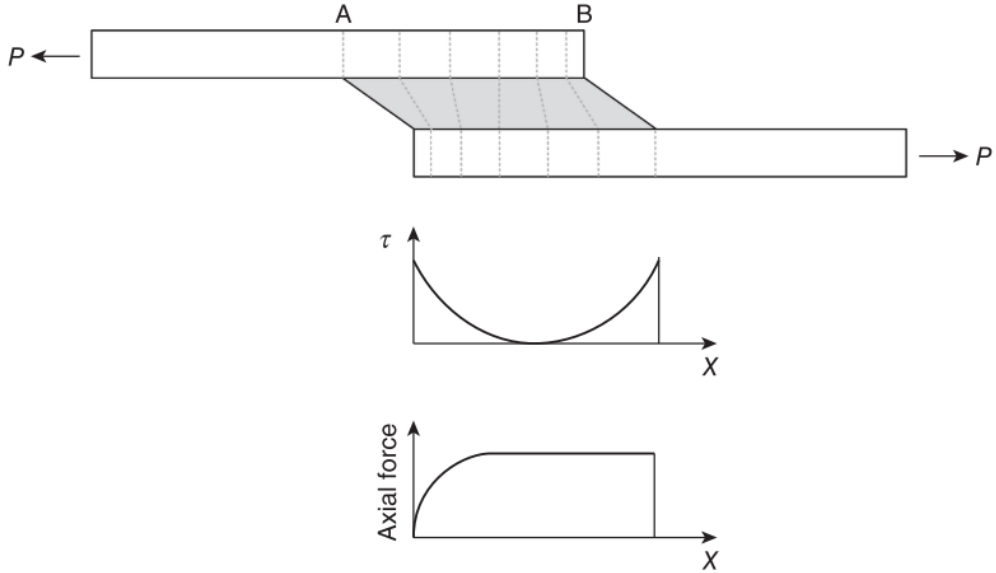


Figure 3.3: Differential shear approach [25]

For a numerical approach when determining failure, *Cohesive Zone Models (CZM)* are used [25][23][24]. These types of models are based on traction-separation laws and require material data that has to be determined experimentally. This is not something that will be further looked into, as these data were unobtainable, and the point of failure is not of interest in this thesis. The modelling of the joint is explained in the appendix. A.

4 Methods

To compare finite element (FE) simulations to experimental testing, strain gauge (SG) data and load-displacement data will be compared. The strain gauges give a measurement locally, while the load displacement data gives a better view on a global scale. A model within an acceptable deviation with regards to the displacement of the experimental tests, can be changed to work with other suspension members on the vehicle. This means keeping the same modelling parameters for adhesive, CFRP rods, spherical bearings and boundary conditions, but changing geometry. The model must agree both locally and globally (strain gauges and load-displacement). Results from FE-models of all suspension members can then be used to analyse how compliance affects the vehicle in the compliance FE-model. It must be noted that only small deviations are acceptable for both SG data and load-displacement data, for extrapolating the results to other suspension members. The total approach is illustrated in the flow chart below in figure 4.1.

Note: ALL CAD modelling is done in Solidworks (Dassault Systèmes, France), all FE-modelling is done with Abaqus CAE 2017 (Dassault Systèmes, France). Data analysis was done in Matlab R2018b (Mathworks, USA).

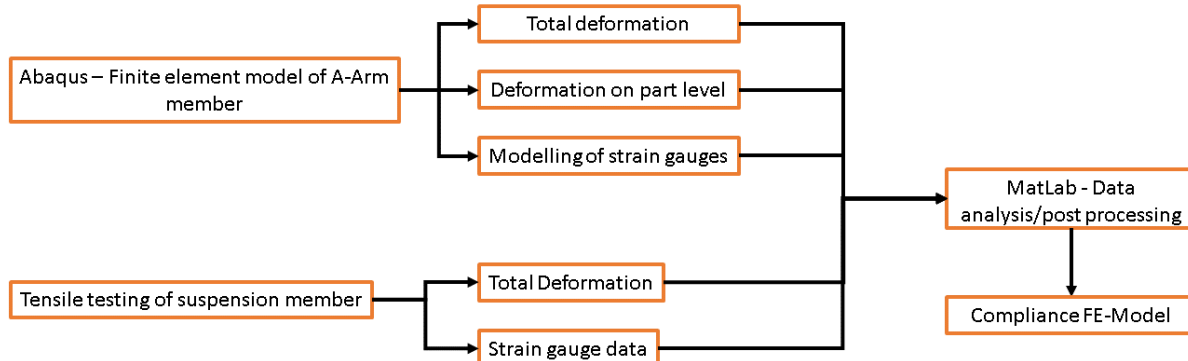


Figure 4.1: Work flow

4.1 Finite element modelling of A-arm

A simplified FE-model was first made to find strained areas for strain gauge placement. The final FE-model consisted of thirteen parts. Geometry was imported from Solidworks CAD to the Abaqus CAE environment as a .stp file. Material properties used were found through the suppliers, or in literature [26]. Modelling of the CFRP rod was done with the Abaqus layup module. For the rod, a conventional shell section was chosen, while all other parts in the simulation were simulated as solids. The adhesive joint was simplified to a tie constraint. This was due to its thickness only being 0.1 mm. Assuming the compliant affect to be negligible. Contact interaction between adjacent parts, was modelled using the general contact behaviour. With contact predominantly between steel and aluminium one contact property was made. This contact property was modeled with a penalty friction of 0.5 tangentially, and hard (no penetration) normally. The coefficient of friction used, is based on values found in literature [27]. The spherical bearings are modelled as solid steel rings, meaning without liner and outer and inner ring in one piece. A detailed description of the FE-model can be found in the appendix A.

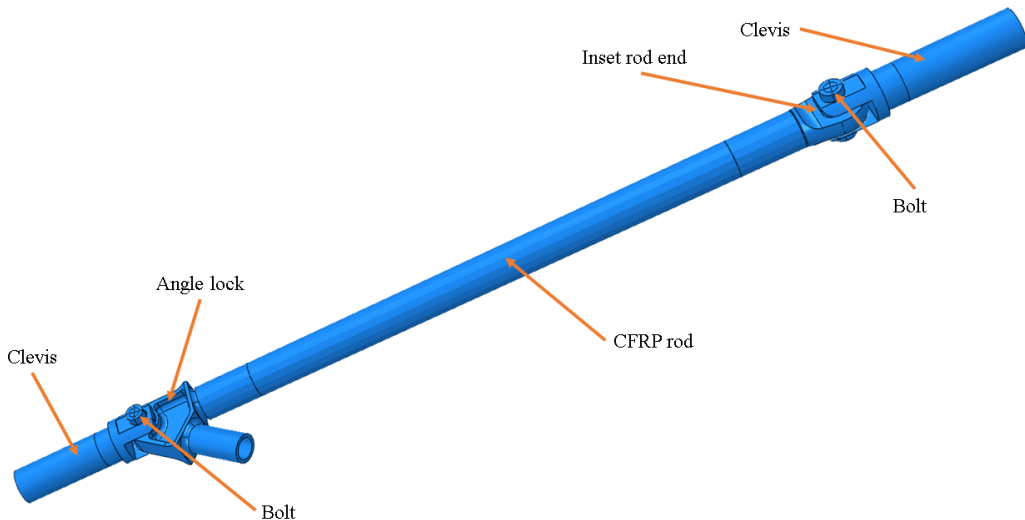


Figure 4.2: A-arm assembly in Abaqus CAE

4.2 Modelling of Strain Gauges

A technique for modelling strain gauges was presented in the project thesis [1]. The strain gauge was modelled as an independent surface and then assembled in its correct position. This was done in Solidworks. With this method, close attention was needed when making the gauge, as it needed to fit the geometry of the adherent surface perfectly. The surface then needed to be constrained to its surface after being imported into Abaqus CAE. All the aforementioned steps made it easier to introduce more errors into the simulation. For this reason, and the process being too tedious, a different method has been used. In the FE-model of the A-arm, each strain gauge has been made by partitioning the face, where the strain gauge sits. This has been done in Solidworks. The partition has the same area as the strain gauge's measuring grid. The partition have then been made into a geometry *set* in Abaqus CAE. Data points were then extracted from all the integration points within the set, and averaged. This was then compared to experimental data. The method did not require any definition of constraints between the strain gauge and the part it is attached to. The area of the strain gauge was given a refined mesh to give more data points. The placements of the strain gauges can be seen in figure 4.3. It must be noted that on the angle lock there was a strain field with higher values. This can be seen in figure 4.3. It was decided not to place a gauge here. The reason for this is the location and size of the area. It would have made accurate placement of the SG difficult.

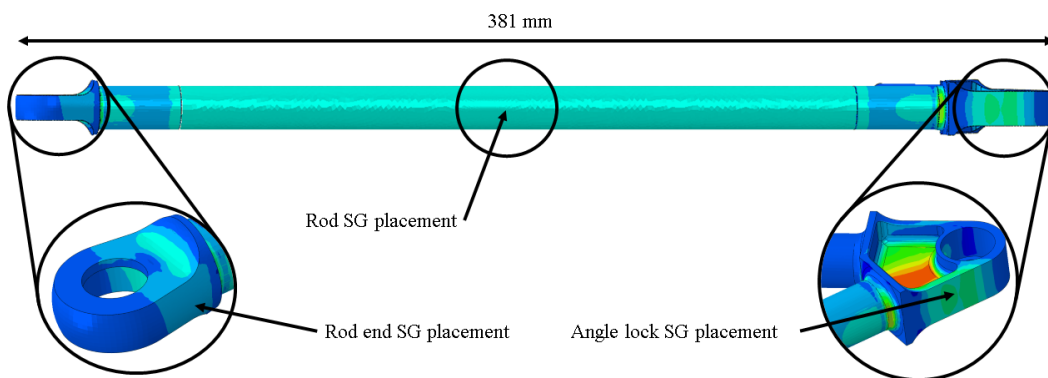


Figure 4.3: Simplified FE-model for strain gauge placement

4.3 Tensile Testing of Rods

The tensile test machine used was an Instron Model 1342 100 kN (fig. 4.4). With 19 mm to 27 grips. Rods were installed ensuring that no pre-strain was introduced. First the machine was lifted to accommodate the rod length. One side of the rod was loosely secured to the clevis. This end was then clamped into the tensile test machine, in the bottom clamp. The other clevis was secured into the top clamp of the machine. The top clevis was then lowered manually until it was possible to secure the clevis to the rod. Shoulder bolts and fitting spacers were used between clevis and rod, to avoid any unwanted compliance. Bolt were tightened to 7.5 Nm. Clevises were marked at the edge of clamp. A HBM MX1615 DAQ (fig.4.5) was used. A sample frequency of 300Hz was used for data acquisition using the standard filtration settings of the DAQ. Rest of the equipment used can be seen in figure. 4.6. All rods were assembled according to steps stated in table. 4.2.



Figure 4.4: Instron 1342



Figure 4.5: HBM 1615 data aquisition unit

**Table 4.1:** A-arm in tensile test machine

Assembly Steps	
1	Cleaning of CFRP rod, angle lock and insert rod end with acetone.
2	Sanding of CFRP rod with 80 grit sandpaper to remove epoxy film.
3	Grit blasting aluminium parts to remove oxide layer.
4	Cleaning all parts with acetone again.
5	Mixing and applying adhesive.
6	Assembling rods and adjusting to correct length.
7	3 hours in oven at 60 degrees Celsius.

Table 4.2: Assembly steps of A-arm assembly**Figure 4.6:** Equipment used for testing

4. METHODS

4.3.1 Mounting of strain gauges

Strain gauges were mounted before mounting the rod in the tensile test machine. Strain gauges used were Tokyo Measuring Instrument Company (TML) FLAB-3-11-3LJCT-F. These are three wire, one axis, 120 ohm strain gauges. Each area was cleaned with acetone, abraded with 400 grit paper, cleaned with acetone and marked. All cleaning was done using cotton swabs dipped in acetone. Cleaning was stopped when no visible contaminates could be seen after rubbing the mounting area. Two drops of TML CN Cyanoacrylate adhesive were applied to the gauge, before mounting it according to the marked area. Thumb pressure was applied holding release paper on top of the gauge. A piece of tape was used to hold the lead wires in place. Before mounting the rods in the tensile test machine, the lead wires were connected to a phoenix connector.



Figure 4.7: Strain gauge bonded to angle lock

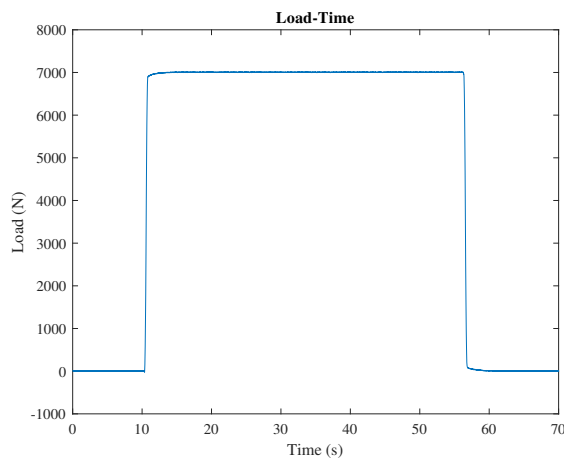


Figure 4.8: Load application 7000 N

4.3.2 Load application and data analysis

Load was applied by setting specific set-points. The load was held for a minimum of 30 seconds before a set point of zero load was set. This was done with 1000 N increments, up to 7000 N. Load application can be seen in fig. 4.8. The machine was not re-calibrated in between increments

For data extraction the time data points corresponding to the load of interest, were identified. This can be seen in figure. 4.9. A time vector with these points was made and the strain values for the three gauges at the correct load could then be identified. These values were then averaged and further used for comparison to simulated values.

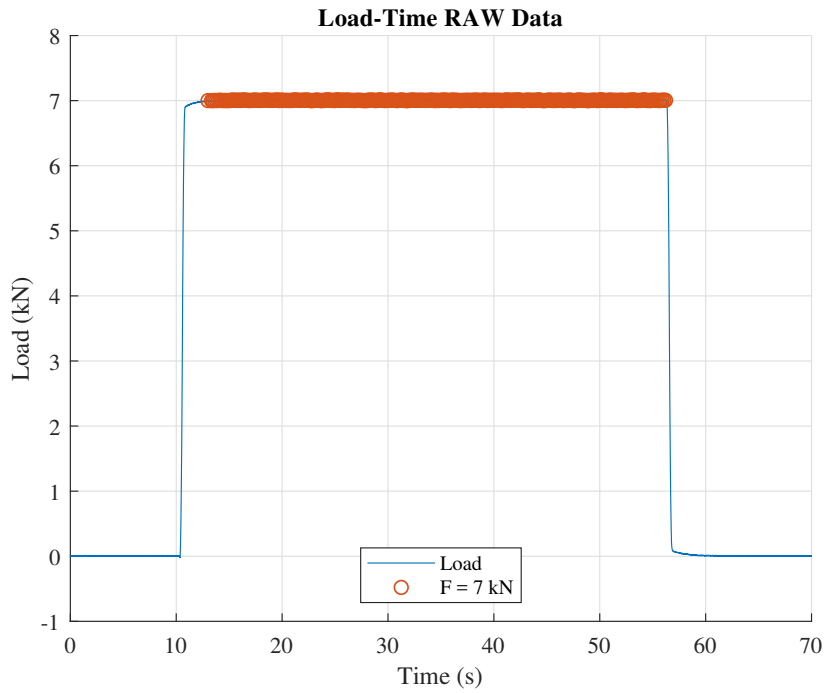


Figure 4.9: Identified data points plotted in orange for waned load in orange

Error percentage values have been calculated through the following formula:

$$Er\% = \left(\frac{Experimental - Simulated}{Simulated} \right) * 100 \quad (12)$$

4.4 Compliance Model

An effort has been made to evaluate how compliance in the suspension rods affect the wheel angles (toe and camber angle). This approach has been made to accommodate adding parts in the future, as compliance test data is accumulated. The approach simplifies each suspension member to being a single spring. The equivalent stiffness of one suspension member (K_{eq}) can be calculated through equation 13. This equations simplifies the the suspension member to a series of springs, where each part of the assembly has its own spring constant k_n . A graphical representation of this model can be seen in figure. 4.10.

$$K_{eq} = \left(\sum_{n=1}^n \frac{1}{k_n} \right)^{-1} \quad (13)$$

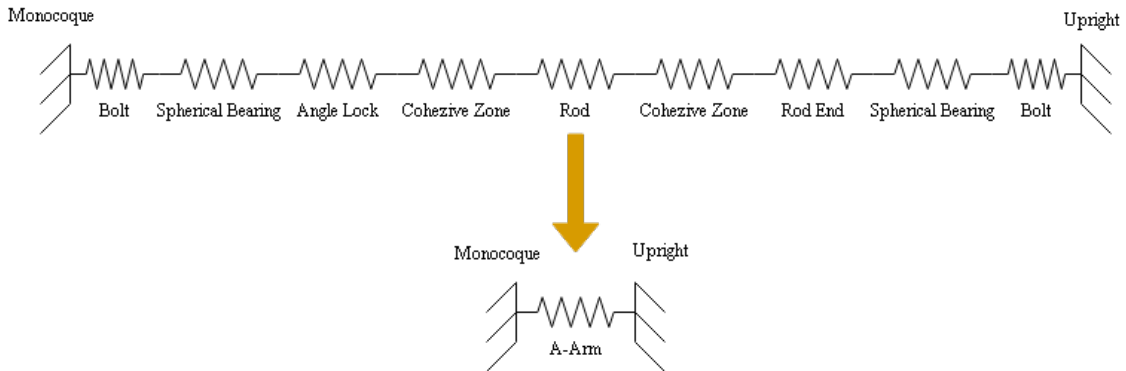


Figure 4.10: A-arm member as springs in series model

The model can be used to verify the global stiffness of whole assemblies towards smaller FE-models and testing of specific parts.

4.5 FE-modelling of the Compliance Model

The FE-model for the compliance analysis is made using the Python scripting interface in Abaqus. The script auto generates the suspension members from one corner of the vehicle. The input variables are the suspension pickup points and the spring constants calculated from the FE-model of the suspension member and loads at the contact patch. The suspension members are connected to a link structure, which functions as the wheel assembly (upright, rim and tire). There are a total number of three junction points in this beam structure. The upper upright mounting point, the lower upright mounting point and outboard tie rod mounting point. Displacement is tracked at these three points through the entire simulation. This is then compared to the initial position of the three points. This data makes it possible to estimate the wheels' movement due to compliance as the load is applied at the contact patch. The script can be seen in the appendix.

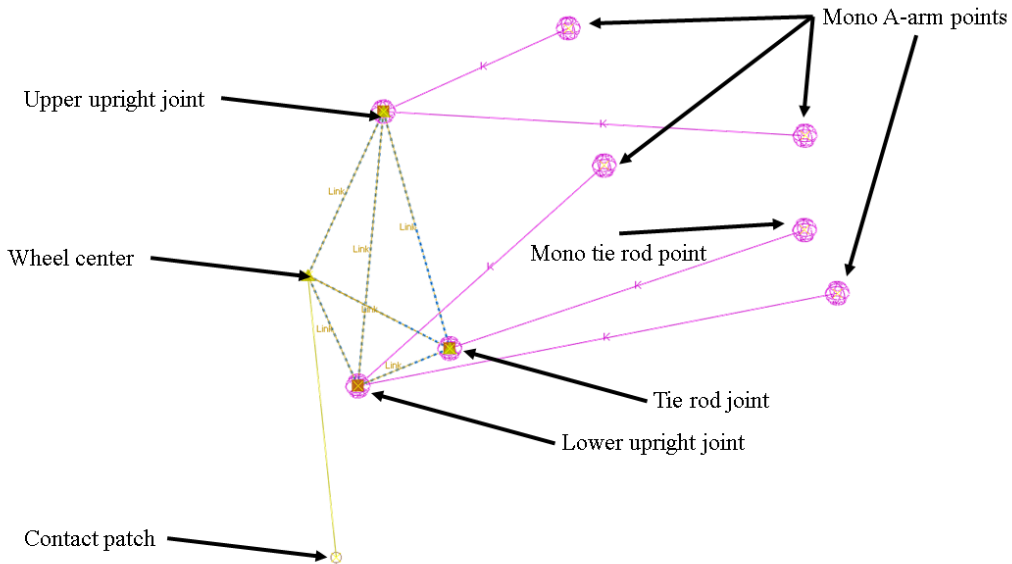


Figure 4.11: Model of suspension with members as springs. The a-arms and the tie rod can be seen in pink. The wheel assembly can be seen as the dashed lines

5 Results

The results presented in the following section are raw data from the tensile testing of the A-arm member. Load-displacement data for all loads is presented. Maximum load-displacement values have been compared as well. Strain gauge data is presented at all loads. A plot for each gauge has also been generated with a plot comparing averaged strain data from experiment, towards average strain data simulated.

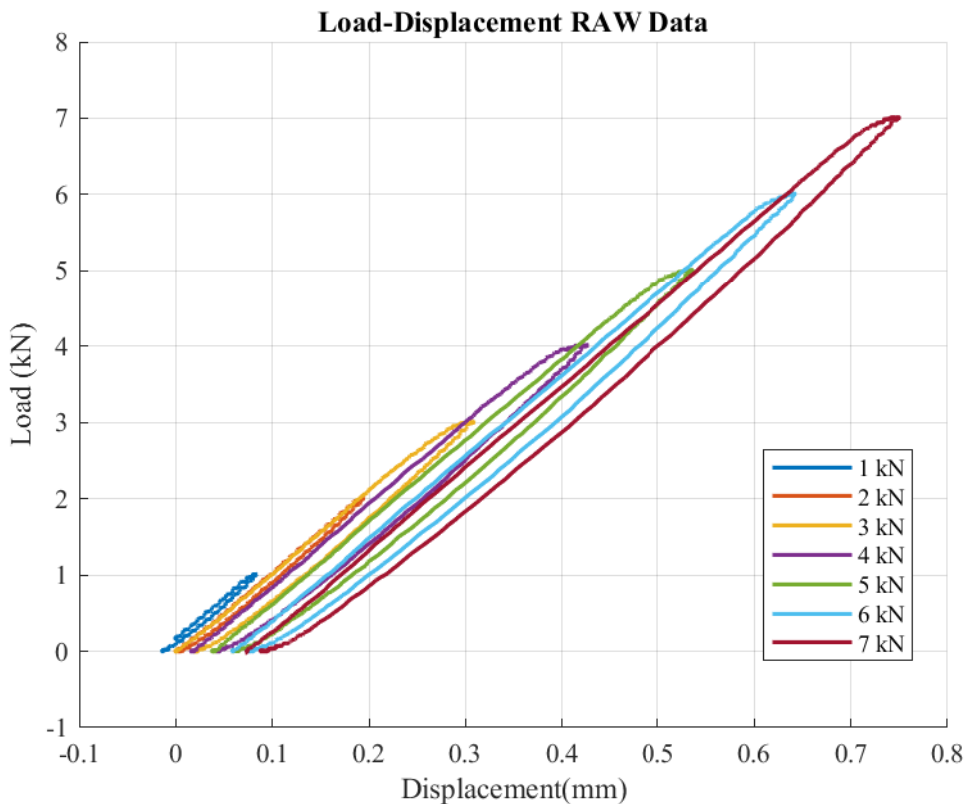


Figure 5.1: Raw load-displacement curves. A drift in zero point is observed

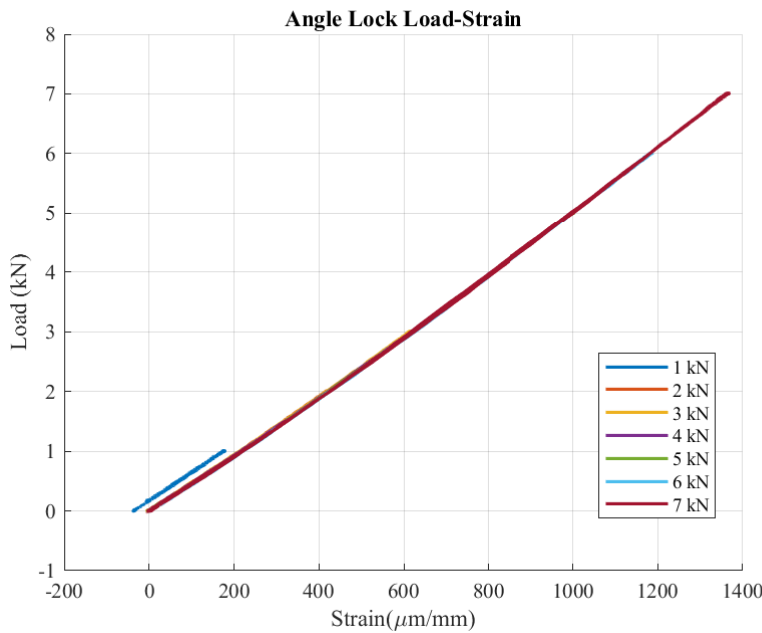


Figure 5.2: Angle lock strain gauge results at each load level. A small offset in the load increment of 1 kN is observed.

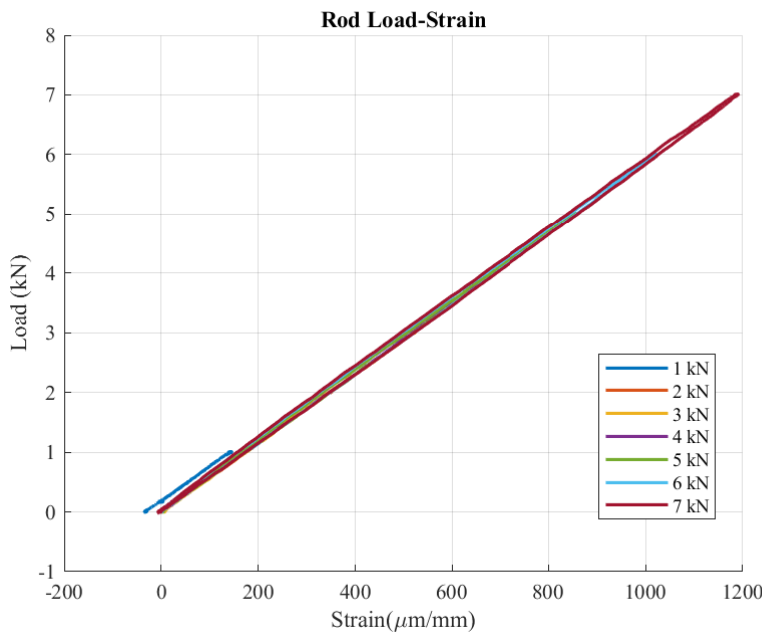


Figure 5.3: Rod strain gauge results at each load level. A small offset in the load increment of 1 kN is observed.

5. RESULTS

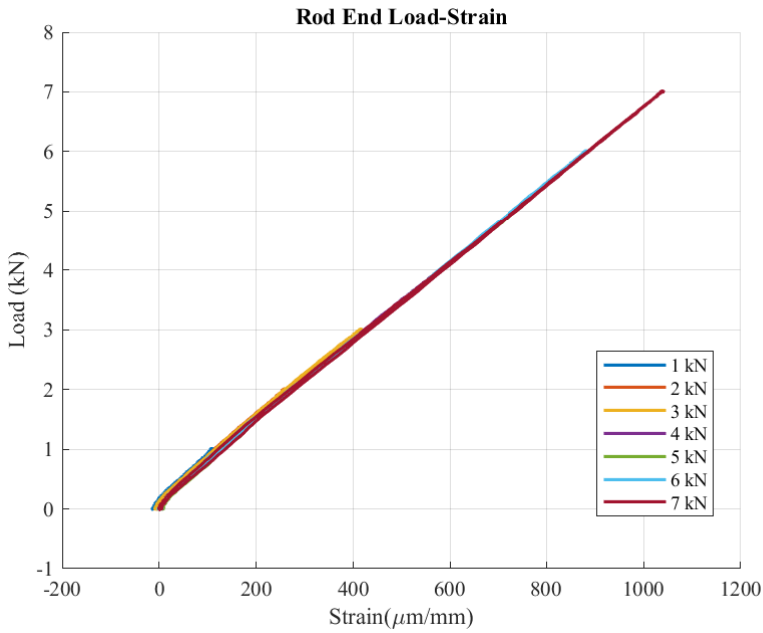


Figure 5.4: Rod end strain gauge results at each load level. A small offset in the load increment of 1 kN is observed.

Load-Displacement Comparison			
Load (kN)	Exp. mm	Sim. mm	Dev. (%)
1	0,09	0,11	-10,1
2	0,19	0,22	-10,7
3	0,31	0,33	-6
4	0,41	0,44	-6,2
5	0,49	0,55	-9,2
6	0,58	0,66	-11,4
7	0,67	0,77	12

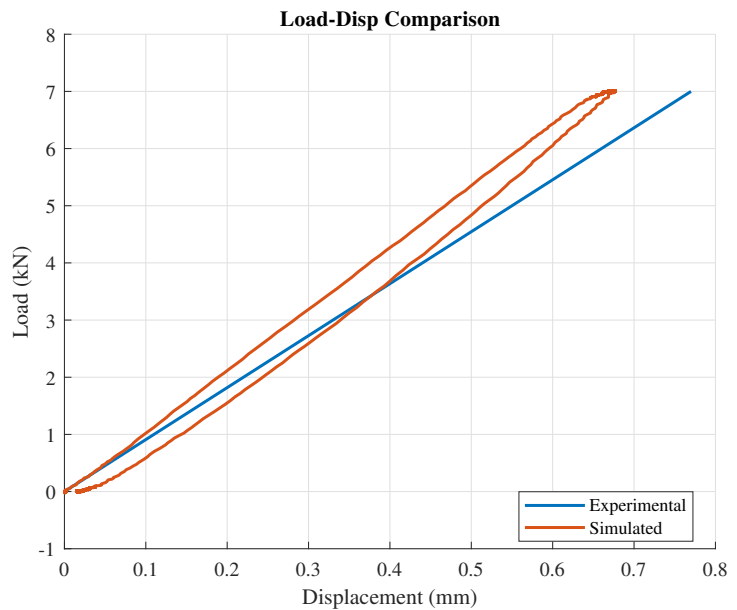


Figure 5.5: Load-displacement comparison, error ranging from -6% to 12 %

Angle Lock Strain Gauge			
Load (kN)	Exp. $\frac{\mu m}{mm}$	Sim. $\frac{\mu m}{mm}$	Dev. %
1	175,82	164,23	7,1
2	418,38	339,77	23,1
3	614,38	514,47	19,4
4	810,29	688,85	17,6
5	999,26	895,22	15,8
6	1184,52	1037,56	14,2
7	1364,42	1211,72	12,6

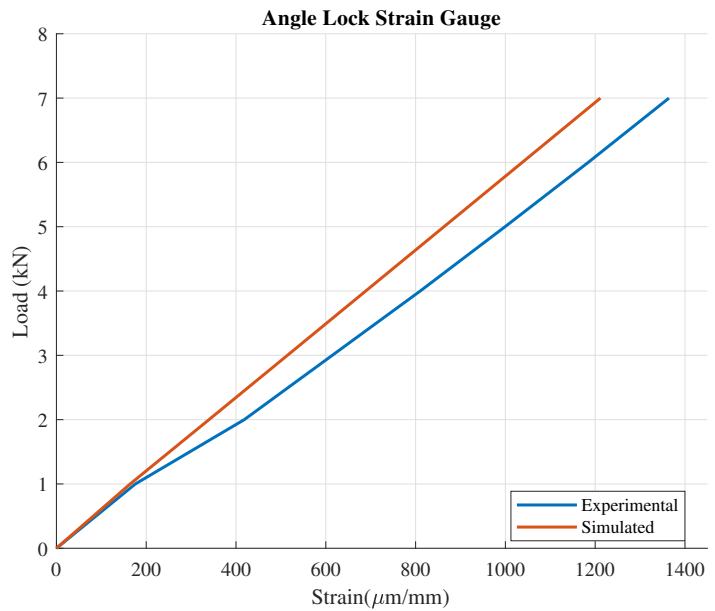


Figure 5.6: Angle lock strain gauge comparison, error ranging from 7,1 % to 19,4%

Rod Strain Gauge			
Load (kN)	Exp. $\frac{\mu m}{mm}$	Sim. $\frac{\mu m}{mm}$	Dev. %
1	141,78	311,22	-54,4
2	347,72	623,43	-44,2
3	520,57	935,73	-44,4
4	681,6	1247,96	-45,4
5	854,61	1560,19	-45,2
6	1018,57	1872,5	-45,6
7	1187,49	2184,81	-45,6

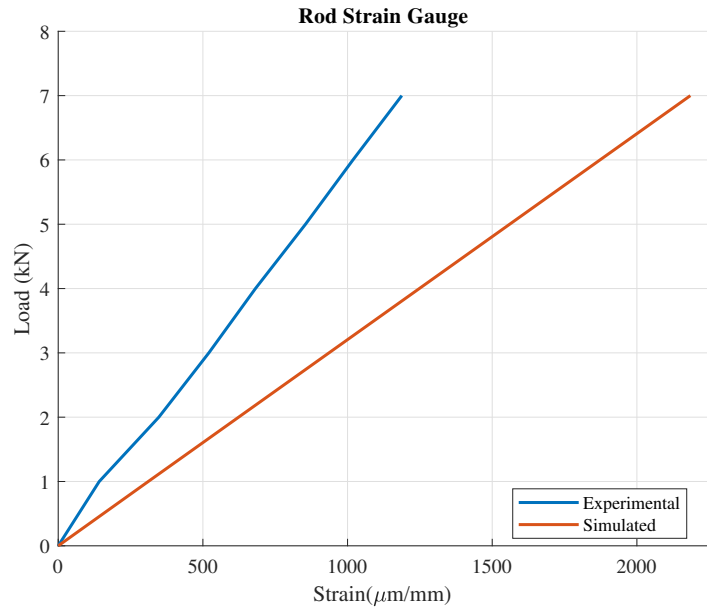


Figure 5.7: Rod strain gauge comparison, error ranging -44,2% to -54,4%

Rod End Strain Gauge			
Load (kN)	Exp. $\frac{\mu m}{mm}$	Sim. $\frac{\mu m}{mm}$	Dev. %
1 kN	108,1	91	18,7
2 kN	258,5	197,47	35
3 kN	415,1	291,64	42,3
4 kN	580,2	392,69	47,8
5 kN	735,7	494,23	48,9
6 kN	882,9	595,83	48,2
7 kN	1038,2	697,6	48,8

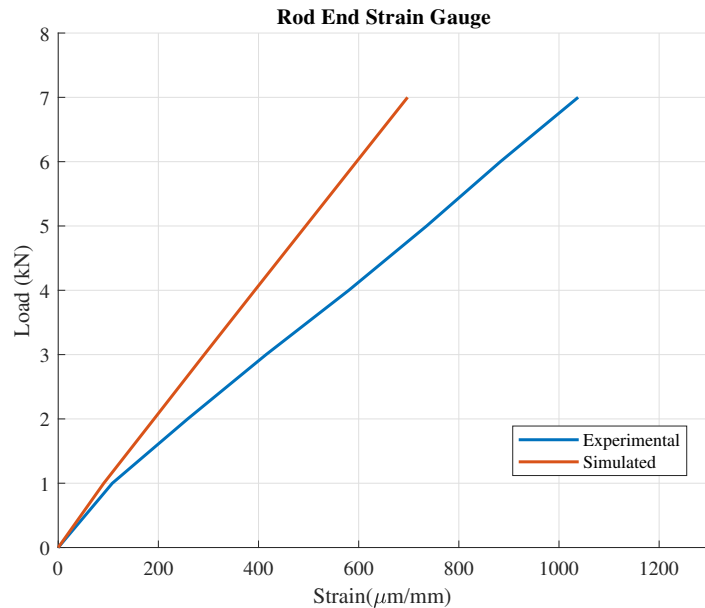


Figure 5.8: Rod end strain comparison, error ranging from 18,7 % to 48,8%

5.0.1 Summary

Comparing load-displacement data from experiment to simulation shows the error range to be within **-10%** to **12%**. The largest deviation can be found at a load of 7 kN. Looking at the strain gauges individually, the angle lock strain gauge proved to be the within **25%** at all loads and within **12,6%** at 7 kN. The rod strain gauge was steady at **44%** to **55%**, and within **45,6%** at 7 kN. The rod end strain gauge stayed within **50%** at all loads, with **48,8%** at 7 kN.

6 Discussion

6.1 Main Findings

When comparing the FE-model to the experimental values, the load-displacement results are within an acceptable error (maximum of 12% at 7 kN). When looking at the strain gauge data, the percentage of deviation is greater (maximum of 48,8% at 7kN). The simplifications in the FE-model (spherical bearings, adhesive joint) should have made the simulation, "stiffer" than the experiment. No material errors in FEA also speaks for stiffer results. It is also a fairly simple experiment. An assembly with few non-complex parts, uniaxial loading and defined input loads and boundary conditions. This should have made for better agreement between simulated and experimental values. As there is not a sufficient agreement between the local results (strain gauge) and the global results (load-disp.) it is not rendered wise to change the models geometry to fit other suspension members. Therefore the results have been rendered too inaccurate to be used in the compliance FE-model.

6.2 A-arm finite element model

The results compared show the overall trend that the finite element model is "softer" than the experimental values. As there are no material deviations (impurities, production flaws) in the FE-model it is expected to see the FE-model being "stiffer". Simplifications made to the adhesive joint, spherical bearing and the assumed coefficient of friction (0.5) between parts were thought to contribute to a stiffer assembly.

Reasons for the final results are discussed in the following section. It is clear that rod is a big contributor to this discrepancy, as it is the longest part in the assembly, and the strain gauge comparison is not coinciding.

6.2.1 CFRP Rod modelling

Since the CFRP rod is the longest single part in the assembly, it is most likely the part accountable for most of the compliance in the system. The CFRP rod strain gauge shows correlation between the simulated values and the experimental values within 55%. The making of the rod relies heavily on the production technique, equipment and over all crafts-

6. DISCUSSION

manship of the operator. This introduces potential inaccuracies. To see if deviations can be seen due to extra ply layers, or the angle of the different plies, two sensitivity studies have been performed. Both studies show the load-displacement of the rod isolated. In the first study, the fibre orientation of the longitudinal fibres were shifted starting at 0 degrees (parallel to center axis) and ending up at 14 degrees. The results can be seen in figure. 6.1. In the other study, the layup orientation of the longitudinal plies were kept at 6 degrees, but extra 6 degree plies were added to the original layup. The results of this can be seen in figure. 6.2. The results show that an operator error due to the layup angle will not change the results from the experiment drastically. It must be noted that these simulations were performed with different material properties, but the same layup.

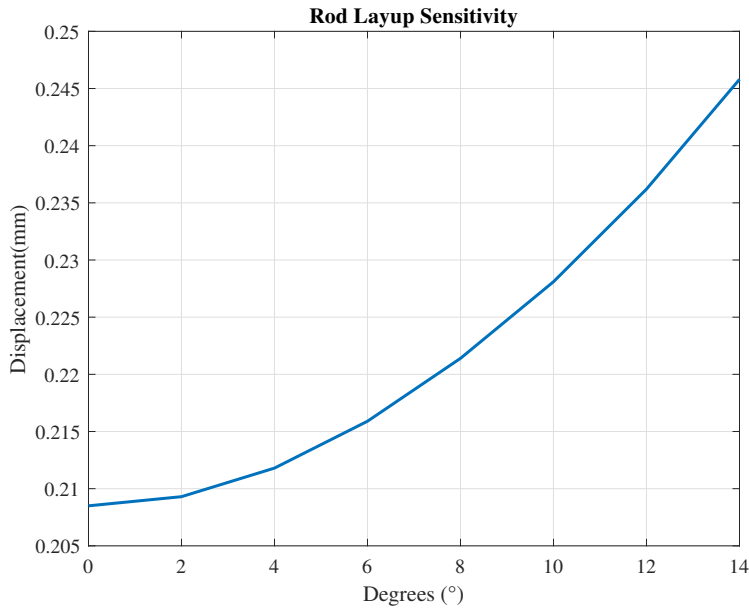


Figure 6.1: Displacement vs. shifting of ply layup angle from 6° to 14°

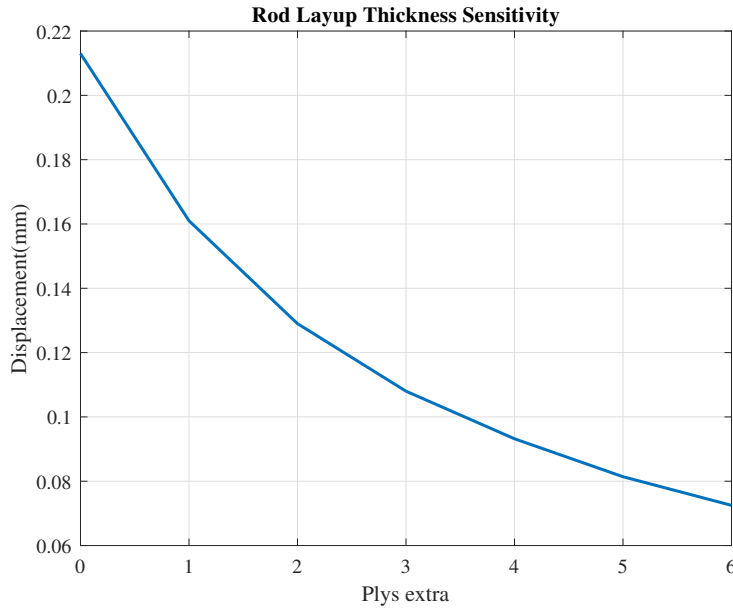


Figure 6.2: Displacement vs. adding one ply at the time extra to the layup

6.2.2 Spherical Bearing modelling

The spherical bearings are modeled as a solid rings with isotropic material behaviour. This is a gross simplification to the actual spherical bearing. This approach was chosen as the material characteristics of the bearings were unobtainable, especially with regards to the liner. It is very clear that this will not be an accurate representation of the bearing. In the paper by Zipfel et. al [28], they tested several *spherical rod ends*. These components have a similar construction as a spherical bearing. Their behaviour can therefore be regarded as similar in terms of compliance. In their experiment, they tested ten different spherical bearings. Their results show close to linear behaviour. Based on their findings, a sensitivity study has been done on the bearing. This has been done by simulating a smaller assembly, see figure. 6.3. The load is set to 7 kN and the young's modulus of the bearing material is changed incrementally. Although this is a crude estimate it shows that the deformation changes very little. It proves that very little change would be expected even tough material characteristics would have been modeled more accurately.

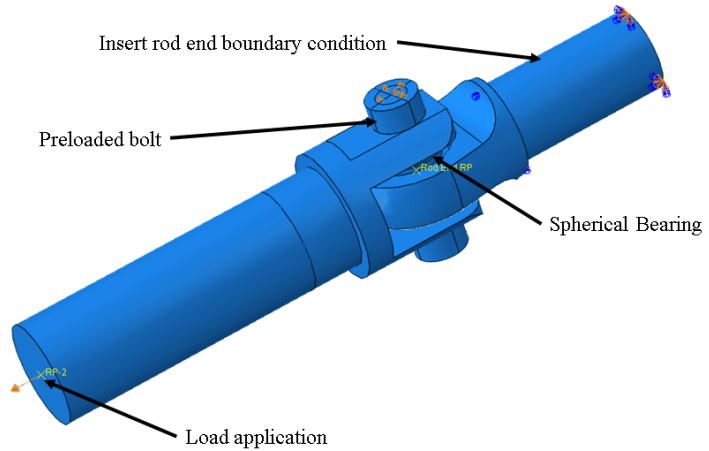
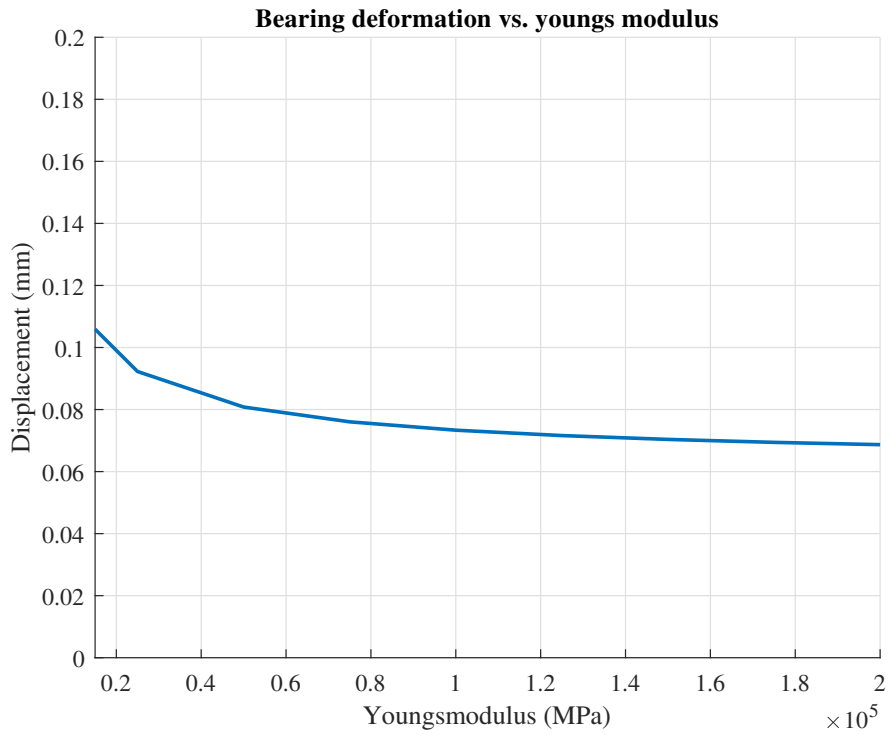


Figure 6.3: Only clevis and insert rod end was assembled. 6,8 kN of preload was applied. load was set to 7 kN



6.2.3 Adhesive joint modelling

Because of the thickness of the adhesive interface (0.1mm), it is not thought that it is a great impact on the overall compliance. Since accurate material data for the correct modelling approach was not available, it was decided to simulate the adhesive joint as a tied interface. This will be somewhat stiffer than the actual joint,

6.3 Experiment

Both load-displacement data and strain gauge data is linear (as expected), and did not exhibit any anomalies, except for some drift in the zero point of the displacement (figure. 5.1) . Adjusting the zero point for all the data shows that the data is still linear and can be used. See figure. 6.4.

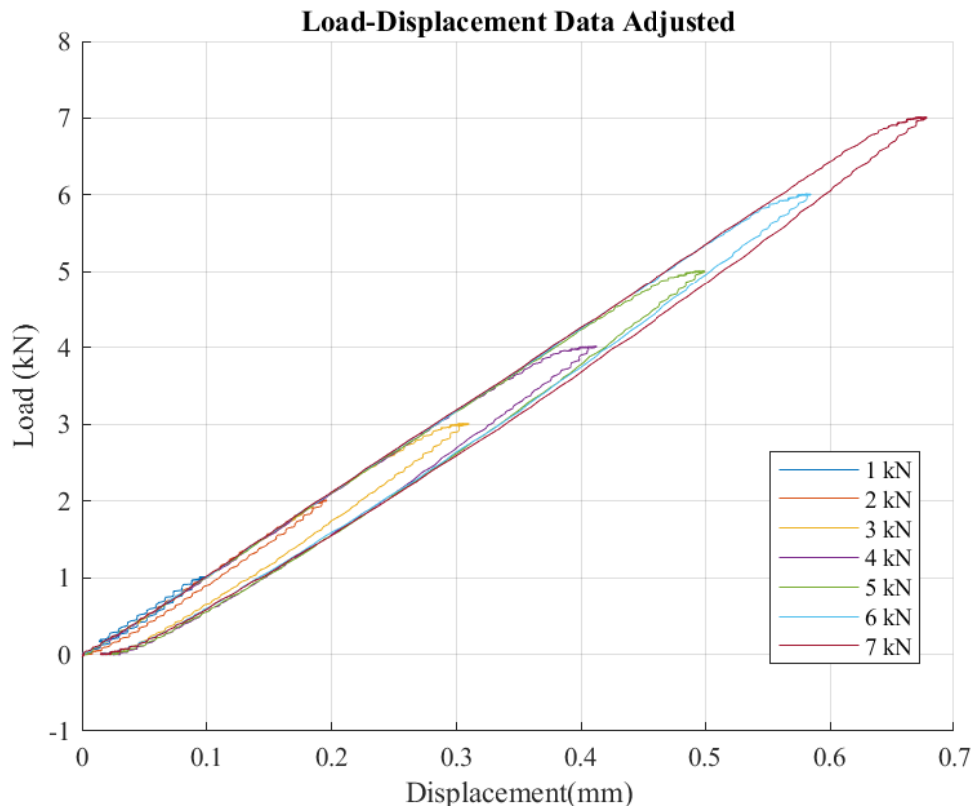


Figure 6.4: The zero point for the load-displacements have been adjusted

6. DISCUSSION

What causes this drift is uncertain, but it does question if the tensile test machine needs to be considered in further detail. It is thought that the compliance in the tensile test machine is of insignificant value.

The results found by Autio et. al [29] show that strain gauge results on a composite can vary to a great extent. This was also seen in the project thesis [1]. On the outside of the rod there is a layer of adhesive tape protecting the main fibre/epoxy matrix. To mount the strain gauge this layer has to be removed. When applying the strain gauge to the rod an uncertainty rises. This is related to how the strain gauge places across the fibre, or of how one bonds it to a part of the rod where the epoxy matrix is more prevalent.

The angle lock SG shows results with low error. The rod end on the other hand, shows deviations comparable to the rod. As it is an isotropic material with well documented characteristics, this result was unexpected. When modelling the suspension member, a guiding boundary condition was made as the simulation would not converge properly. This can explain why the SG in the FE model sees a lower strain value than in the experiment. Unfortunately, the model was never solvable without this BC.

7 Conclusion and Future Work

7.1 Conclusion

Comparing experimental results to a FE-model of one A-arm suspension member has been done. A framework for finding toe and camber compliance has been made. This framework has not yielded any usable results as the FE-model of the suspension member needs further attention. From the test data it can be seen that the angle lock strain gauge is within an acceptable deviation, while the rod end and rod strain gauges are outside of what is acceptable. The load-displacement data seems to be within acceptable deviation to be usable for further modelling. The deviation of the CFRP rod SG-data, and the overall trend that the assembly is more compliant than the experiment, counters this conclusion. Further testing on the rod is advised as it is clearly the part with the most uncertainties, and has the greatest impact on the results. For future work, an acceptable error range would be from 0% to 15% for the isotropic components (insert rod end and angle lock), and some what higher for the composite. This is based on results obtained by Monaheng et. al [30], and their validation of a Ti6Al4V mandibular implant. It is also stated in the article by Barret [31], that simple assemblies can be within 1 % deviation.

Studies done show that the orientation/thickness of the rod is not very sensitive, thus eliminating the manufacturing technique to some extent. The most likely error seems to be the strain gauge mounting.

The spherical bearing contributes to the compliance chain, but modelling it correctly for practical applications is difficult. It is not beneficial for Revolve to simulate the bearings as done by Li et. al [20] and Yang et. al [21], as part of an assembly. Finding the stiffness of the spherical bearings can be done in a likewise manner as Zipfel et. al [28] did in their work. This will yield a stiffness coefficient. This can then be modelled as a regular spring in the FE-model of the suspension member.

The results show that by simplifying the experiment the different deviations and impacts are easier to identify. This makes it easier do identify the next step for getting accurate results between a FE-model and experimental values.

7.1.1 Compliance FEA

To use the compliance model and acquire usable results relating to camber and toe variations, the input parameters need to be trusted. Trustable results were not obtained and the compliance model was not utilized. To use the compliance model, there needs to exist an agreement between the global data (load-displacement) and local data (SG-data) from A-arm testing and simulation. If this is not obtained one cannot have enough confidence in the models ability to accommodate change of geometry.

7.2 Future Work

Methods for future work are listed in the following section.

7.2.1 Testing of CFRP rod

A method for assessing the rods further is proposed, by making two expanding arbors. See. figure 7.1a. When tightening the screws in each arbor, it will expand and hold the rod internally, making it possible to clamp the rod in the tensile test machine without damaging it. A test must be done to see what tightening torque can be applied. This torque will determine the load which can be applied during tensile testing.

7.2.2 Testing of spherical bearing

To find the compliance in one spherical bearing a design has been made. See. figure. 7.2. The design uses one clevis used in the tensile testing of the A-arm, and a separate housing for the spherical bearing. See figure. 7.2b. The housing is welded into a plate which can be secured in the tensile test machines clamp.

7.2.3 Strain Gauge Use

In the experiments advised in the sections above, use multiple strain gauges. This will make it easier to see if one strain gauge does not produce accurate results. Place an unstrained gauge at a reference point to account for changes that might occur during testing. Avoid using linted cloth, or other fabrics that might contaminate the application area, when cleaning.

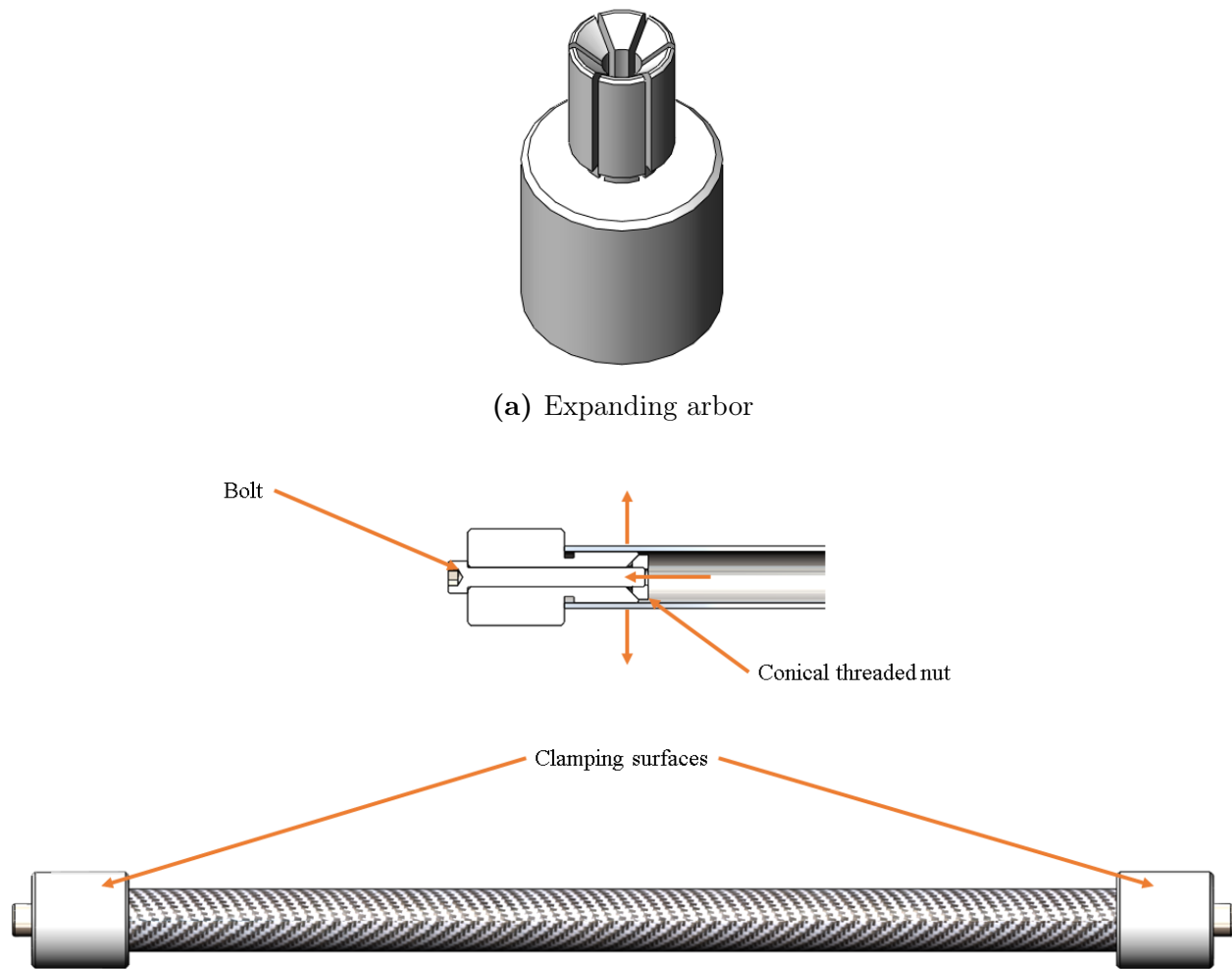


Figure 7.1: Expanding Arbor assembly

7. CONCLUSION AND FUTURE WORK

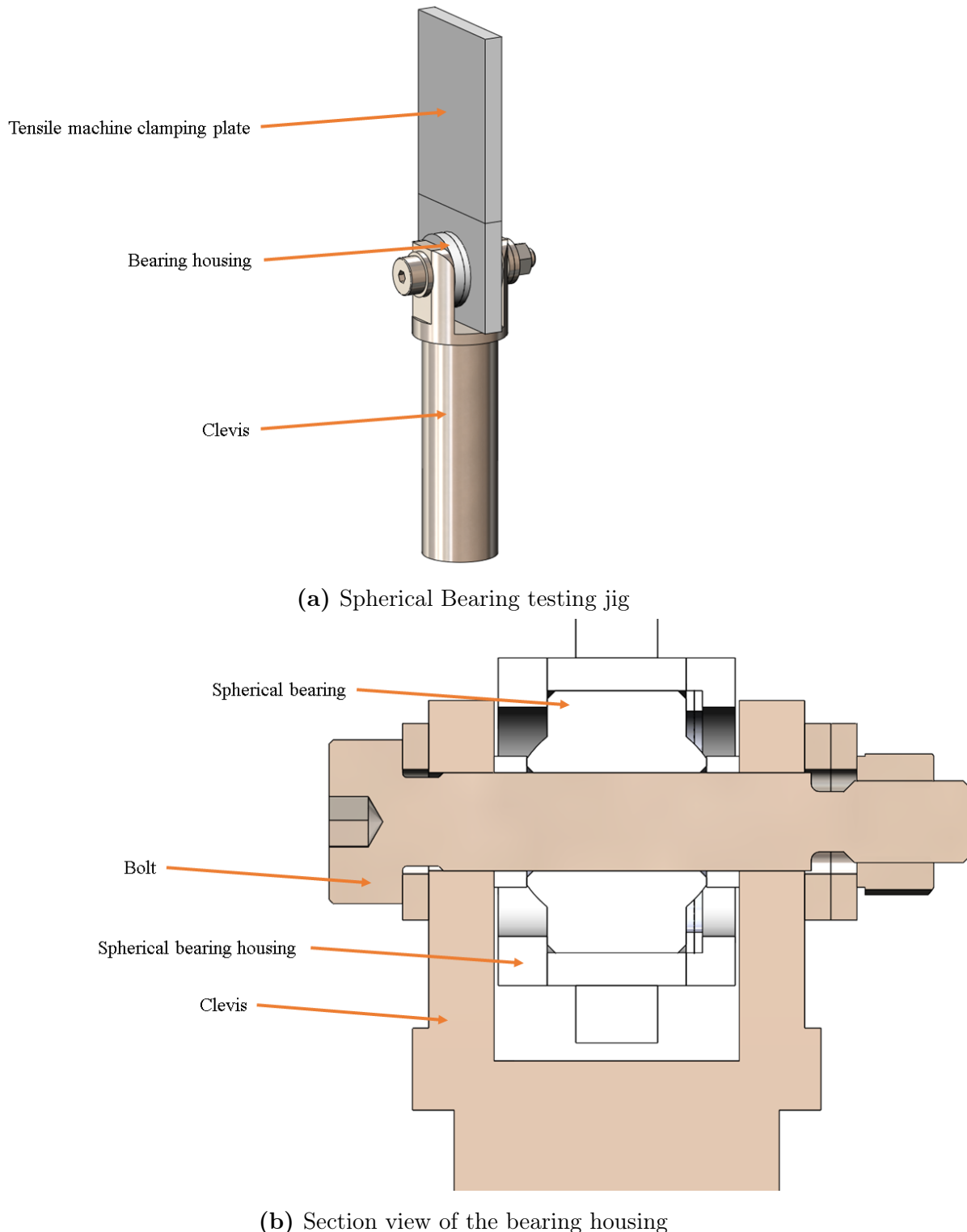


Figure 7.2: Advised test method to determine compliance in spherical bearing

References

- [1] Kristoffer Haugland. “Validation of Finite Element Analysis using strain gauges, of the suspension system of a Formula student car”. Trondheim, 2018.
- [2] SKF Group. “SKF Spherical Plain Bearings and Rod Ends”. In: (2004), p. 136.
- [3] Nils Petter Vedvik. *TMM4175 Polymer Composites*. URL: <http://folk.ntnu.no/nilspv/TMM4175/index.html> (visited on 05/20/2019).
- [4] *Learning Center - What are Unidirectional Carbon Fiber Fabrics?* URL: https://www.fibreglast.com/product/What-are-Unidirectional-Carbon-Fiber-Fabrics/Learning%7B%5C_%7DCenter (visited on 05/20/2019).
- [5] *What is Carbon Fiber? - Element6 Composites*. URL: <https://element6composites.com/what-is-carbon-fiber/> (visited on 05/20/2019).
- [6] *Unidirectional VS Woven Carbon Fiber — Appleman Bicycles*. URL: <https://www.applemanbicycles.com/unidirectional-versus-woven-carbon-fiber/> (visited on 05/21/2019).
- [7] Anonymous. “ME bookshelf – Fundamentals of Modern Manufacturing–Materials, Processes, and Systems by Mikell P. Groover”. In: *Mechanical Engineering* 118.1 (1996). ISSN: 00256501. URL: <http://search.proquest.com/docview/230170268/>.
- [8] Tasdeeq Sofi, Stefan Neunkirchen, and Ralf Schledjewski. “Path calculation, technology and opportunities in dry fiber winding: a review”. In: (2018). ISSN: 2055-0359. DOI: 10.1080/20550340.2018.1500099. URL: <https://www.tandfonline.com/action/journalInformation?journalCode=yadm20>.
- [9] A. Pramanik et al. “Joining of carbon fibre reinforced polymer (CFRP) composites and aluminium alloys – A review”. In: *Composites Part A: Applied Science and Manufacturing* 101 (Oct. 2017), pp. 1–29. ISSN: 1359-835X. DOI: 10.1016/J.COMPOSITESA.2017.06.007. URL: <https://www.sciencedirect.com/science/article/pii/S1359835X1730235X%7B%5C%7Db0090>.
- [10] Gary Savage. “Practical Aspects of Failure Prevention in Bonded Joints on Primary Load Bearing Structures”. In: *Materials and Structures* 1.2 (1994), pp. 67–53. DOI: 10.1007/BF02472819.
- [11] L Chouvet. “Creating the strongest bond on Composites”. In: February (2019).
- [12] “Stiffness — an unknown world of mechanical science?” In: *Injury* 31 (May 2000), pp. 14–84. ISSN: 0020-1383. DOI: 10.1016/S0020-1383(00)80040-6. URL: <https://www.sciencedirect.com/science/article/pii/S0020138300800406>.

REFERENCES

- [13] W F Milliken, D L Milliken, and Society of Automotive Engineers. *Race Car Vehicle Dynamics*. Premiere Series. SAE International, 1995. ISBN: 9781560915263. URL: <https://books.google.no/books?id=opgHfQzlnLEC>.
- [14] FSG: Pat's Seven Deadly Sins of FS Design. URL: <https://www.formulastudent.de/pr/news/details/article/pats-seven-deadly-sins-of-fs-design/> (visited on 11/21/2018).
- [15] Why is compliance so important? - F1technical.net. URL: <https://www.f1technical.net/forum/viewtopic.php?t=8947> (visited on 11/21/2018).
- [16] MARTIN KRÖNKE. 5.6: Camber & Toe - Virtual Racing School (VRS). 2017. URL: <https://virtualracingschool.com/academy/iracing-career-guide/setups/camber-toe/> (visited on 11/17/2018).
- [17] Book : The Contact Patch. URL: <http://the-contact-patch.com/book/road/c1405-front-wheel-set-up> (visited on 06/08/2019).
- [18] Continental. “Continental Formula Student Tire Competition Tire 2016 (C16)”. In: 2019 (2015).
- [19] SAE. *SAE J670 - Vehicle Dynamics Terminology*. Jan. 2008. DOI: https://doi.org/10.4271/J670_200801. URL: https://doi.org/10.4271/J670%7B%5C_%7D200801.
- [20] Kewei Li et al. *Numerical Analysis of Woven Fabric Composites Lubricated Spherical Plain Bearings*. Tech. rep. URL: <http://semimac.org/wp-content/uploads/2015/11/sem.org-SEM-XI-Int-Cong-s076p04-Numerical-Analysis-Woven-Fabric-Composites-Lubricated-Spherical.pdf>.
- [21] Yulin Yang et al. “Effects of Mechanical Properties of Kevlar/PTFE Fabric-Reinforced Self-lubricating Liners on Performance of Self-lubricating Spherical Plain Bearings”. In: (). DOI: 10.4028/www.scientific.net/AMM.29-32.197. URL: www.scientific.net.
- [22] Ever J Barbero. *Finite element analysis of composite materials using Abaqus*. Boca Raton, Fla, 2013.
- [23] F. Mustapha, N.W. Sim, and A. Shahrjerdi. “Finite element analysis (FEA) modeling on adhesive joint for composite fuselage model”. In: *International Journal of Physical Sciences* 6.22 (2011), pp. 5153–5165. ISSN: 19921950.
- [24] H. Khoramishad et al. “A generalised damage model for constant amplitude fatigue loading of adhesively bonded joints”. eng. In: *International Journal of Adhesion and Adhesives* 30.6 (2010), pp. 513–521. ISSN: 0143-7496.
- [25] R. Haghani. “Finite element modelling of adhesive bonds joining fibre-reinforced polymer (FRP) composites to steel”. In: *Rehabilitation of Metallic Civil Infrastructure Using*

- Fiber Reinforced Polymer (FRP) Composites* (Jan. 2014), pp. 60–95. DOI: 10.1533/9780857096654.1.60. URL: <https://www.sciencedirect.com/science/article/pii/B9780857096531500032?via%7B%5C%7D3Dihub>.
- [26] José Humberto S. Almeida et al. “Damage modeling for carbon fiber/epoxy filament wound composite tubes under radial compression”. In: *Composite Structures* 160 (Jan. 2017), pp. 204–210. ISSN: 02638223. DOI: 10.1016/j.compstruct.2016.10.036. URL: <https://linkinghub.elsevier.com/retrieve/pii/S0263822316313083>.
- [27] Dieter Jannasch & Joachim Voßiek Herbert Wittel Dieter Muhs. *Roloff/Matek Maschinenelemente Tabellenbuch*. [22nd ed.]. Springer Vieweg, 2015. ISBN: 9783658090814. URL: <https://link.springer.com/book/10.1007/978-3-658-09082-1>.
- [28] Matthew S. Zipfel and Albert R. George. “Compliance and Friction in Elastic and Mechanical Joints of Race Car Suspensions”. In: *SAE Technical Paper Series* 1.February (2010). DOI: 10.4271/2006-01-3650.
- [29] M. Autio, H. Parviainen, and A. Pramila. “Accuracy of the finite element method in analyzing laminated plate and pipe structures”. In: *Mechanics of Composite Materials* 28.3 (1992), pp. 236–245. ISSN: 0191-5665. DOI: 10.1007/BF00604915. URL: <http://link.springer.com/10.1007/BF00604915>.
- [30] LF Monaheng et al. “Strain gauge validation of finite element analysis of a Ti6Al4V (ELI) mandibular implant produced through additive manufacturing”. In: *Proceedings of the 17th Annual International Conference of the Rapid Product Development Association of South Africa* 978-0-620-72061-8 (2016).
- [31] *Tips and Tricks for Matching FEA Results to Physical Data / CAE Associates*. URL: <https://caeai.com/blog/tips-tricks-matchingfea-results-physical-data> (visited on 12/07/2018).

Appendix

A A-Arm Finite Element Model

A.1 Parts

A simplified assembly of the A-arm was created, and the whole assembly was imported into the Abaqus CAE environment as a .stp. Fillets, chamfers and other geometry deemed not important for the results were removed in Solidworks prior to Abaqus import. The assembly was imported in the coordinate system of the vehicle.

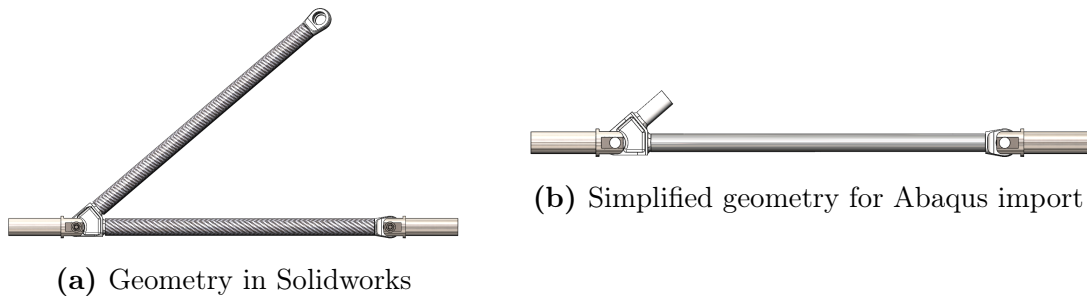


Figure A.1: Geometry simplification

The assembly consists of thirteen parts in total:

- 1 Angle lock
- 1 Rod End
- 1 CFRP Rod
- 2 Shoulder bolts
- 2 Rod end spacers
- 2 Angle lock spacers
- 1 GE8C Dummy bearing
- 1 XRL Dummy bearing
- 2 Clevises

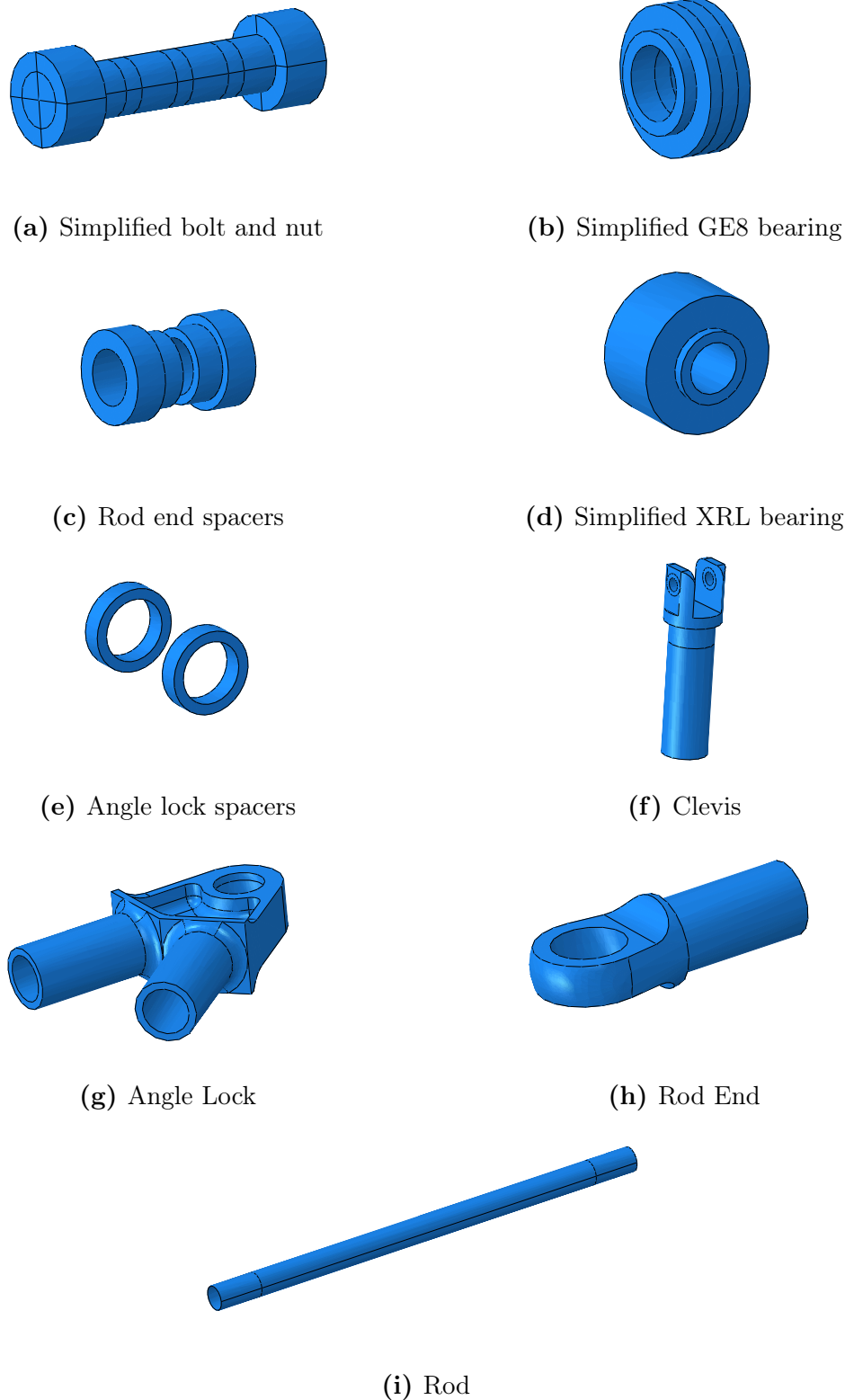


Figure A.2: Parts in simulation

A.2 Material Properties

Four different materials were defined. For angle locks, bolts and spherical bearings isotropic linear elastic material properties were used. In table A.1 the properties of the mentioned parts can be seen. The modelling and material properties of the composite can be seen in the next section.

Material Properties			
Parameters	Steel	Al7075-T6	Spherical Bearing
$E_1(MPa)$	210 000	70500	210 000
v_1	0.3	0.3	0.3

Table A.1: Material properties

A.3 CFRP material properties

The composite used, consists of Torayca T700S fibre and UF3369 TCR resin. To model the composite, elastic material behaviour with the lamina material type was chosen. This module requires longitudinal modulus E_1 , transverse E_2 modulus, poisson ratio for direction 12 (v_{12}) and shear modulus in direction 12, 13 and 23 ($G_{12/13/23}$). Values were at first calculated by using equations 1 to 9, but values were not consistent with what was found in literature. Values used have been obtained through the paper by Almeida et. al [26]. These can be seen in table A.2.

Material Properties Composite	
Parameters	Torayca T700S fibre w/ UFC3369 resin
$E_1(MPa)$	129300
$E_2(MPa)$	9110
v_{12}	0.32
$G_{12}(MPa)$	5440
$G_{13}(MPa)$	5440
$G_{23}(MPa)$	2100

Table A.2: Material properties CFRP rod

A.4 CFRP Layup

The rods were imported as surfaces and the layup was modelled using conventional shell elements. The layup orientation was defined using the discrete function. Selecting the surface for normal axis definition, and the circular edge at one side for the primary axis. This was done to get the correct layup for the rods according to table A.3.

Composite Layup A-Arms		
Layer	Degrees	Thickness
1	87	0.21
2	-6	0.42
3	-87	0.21
4	6	0.42
5	-6	0.42

Table A.3: Layup orientation for CFRP rod

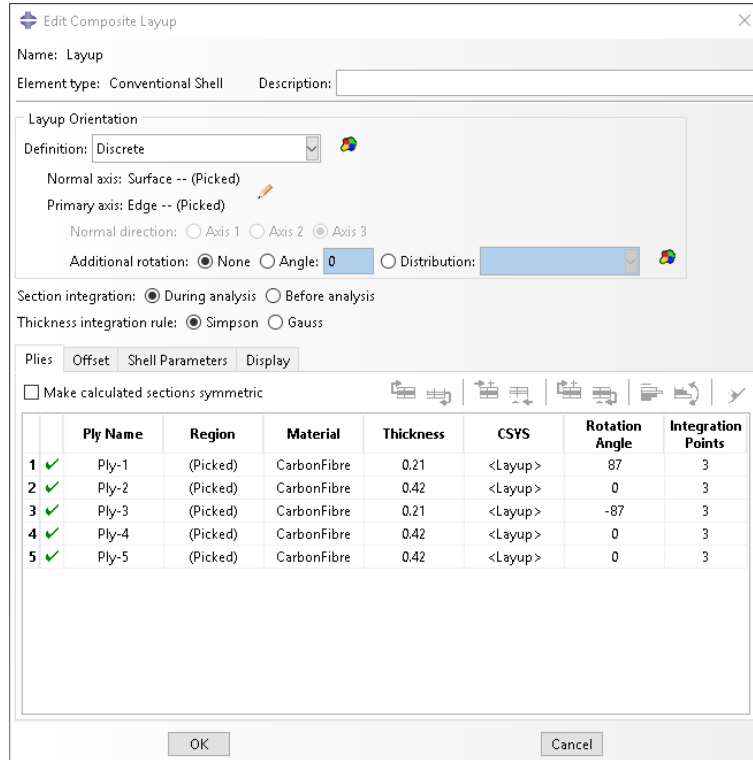
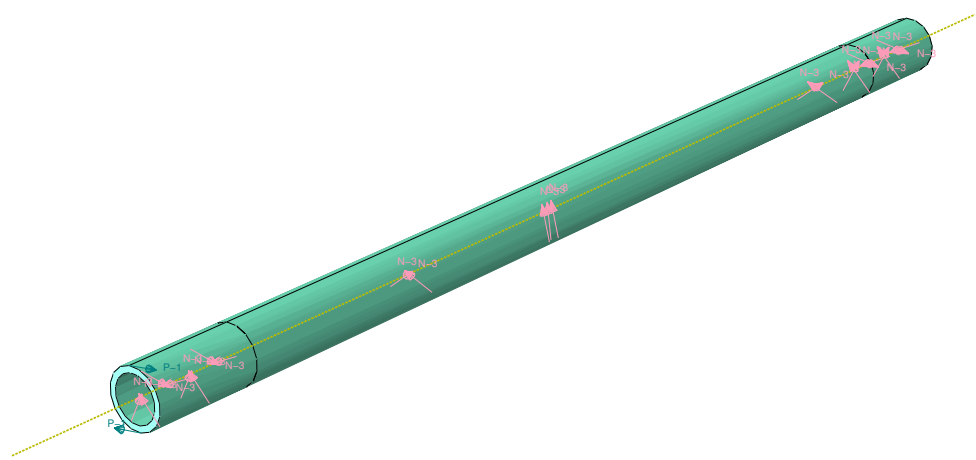
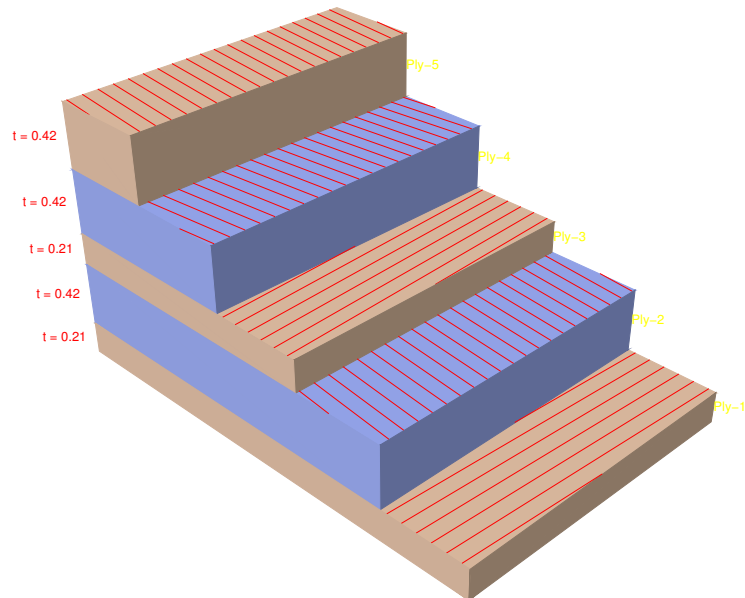


Figure A.3: Layup in Abaqus CAE



(a)



(b)

Figure A.4: Rod layup CSYS and ply stack plot

A.5 Assembly and steps

Two steps were made to accurately represent the loading procedure in the tensile test machine. A *preload step* was made where bolt preload is applied at angle lock bolt and rod end bolt. The next step is the *load step*, where the load is applied. Standard settings in each step was used, except for the initial step increment.

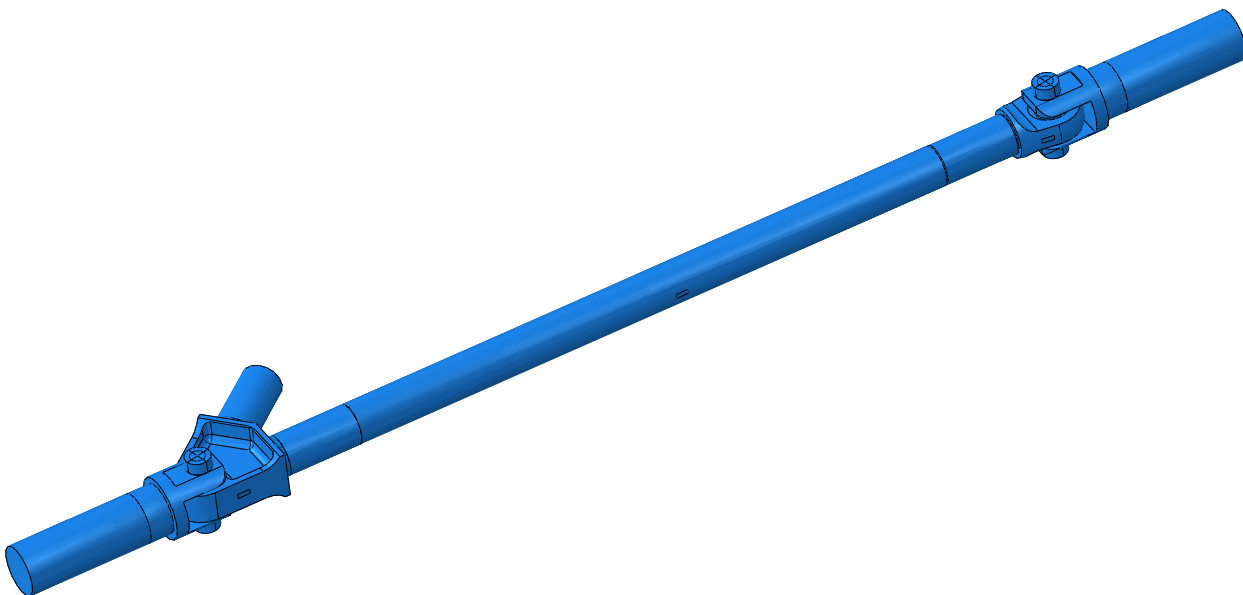


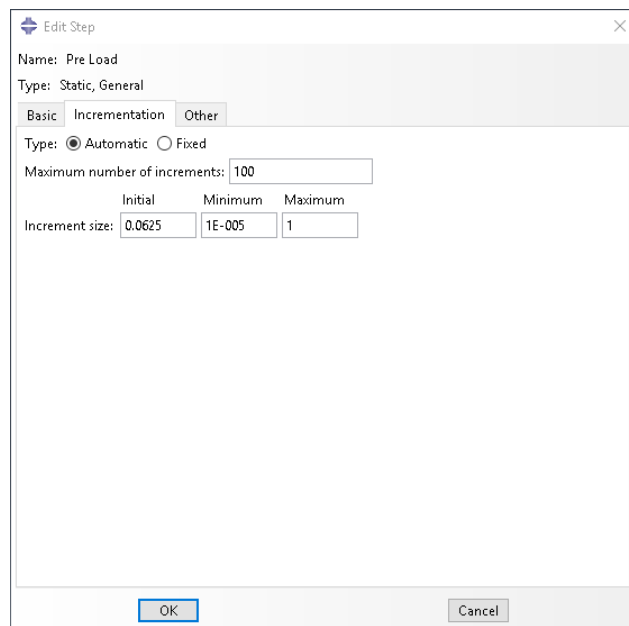
Figure A.5: Assembly of A-arm rod in Abaqus CAE

A screenshot of the 'Step Manager' dialog box from Abaqus CAE. The dialog shows a list of three steps: 'Initial', 'Pre Load', and 'Load'. The 'Initial' step is selected and highlighted in blue. The 'Procedure' column indicates the type of analysis for each step. The 'Nlgeom' and 'Time' columns show specific settings for each step.

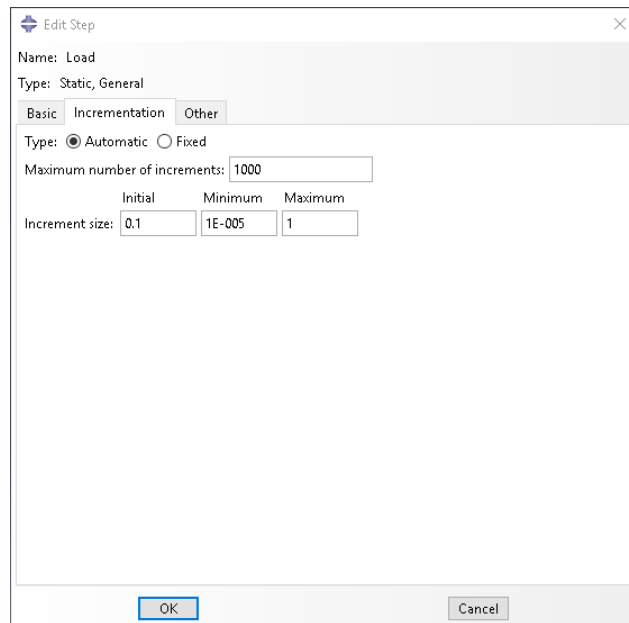
Name	Procedure	Nlgeom	Time
Initial	(Initial)	N/A	N/A
Pre Load	Static, General	OFF	1
Load	Static, General	OFF	1

Below the table are several buttons: 'Create...', 'Edit...', 'Replace...', 'Rename...', 'Delete...', 'Nlgeom...', and 'Dismiss'.

Figure A.6: Steps



(a) Preload settings



(b) Load settings

Figure A.7: Step settings

A.6 Interaction

To simulate the contact interactions between parts, the *general contact* method was used. Each surface pair was defined, this was done to reduce the run time. One interaction property was made (*Alu-Steel*) and used as the global proper assignment. For the contact properties, *hard* was chosen as *normal behavior* Penalty, with a friction coefficient of 0.5, was chosen for the *tangential behaviour*.

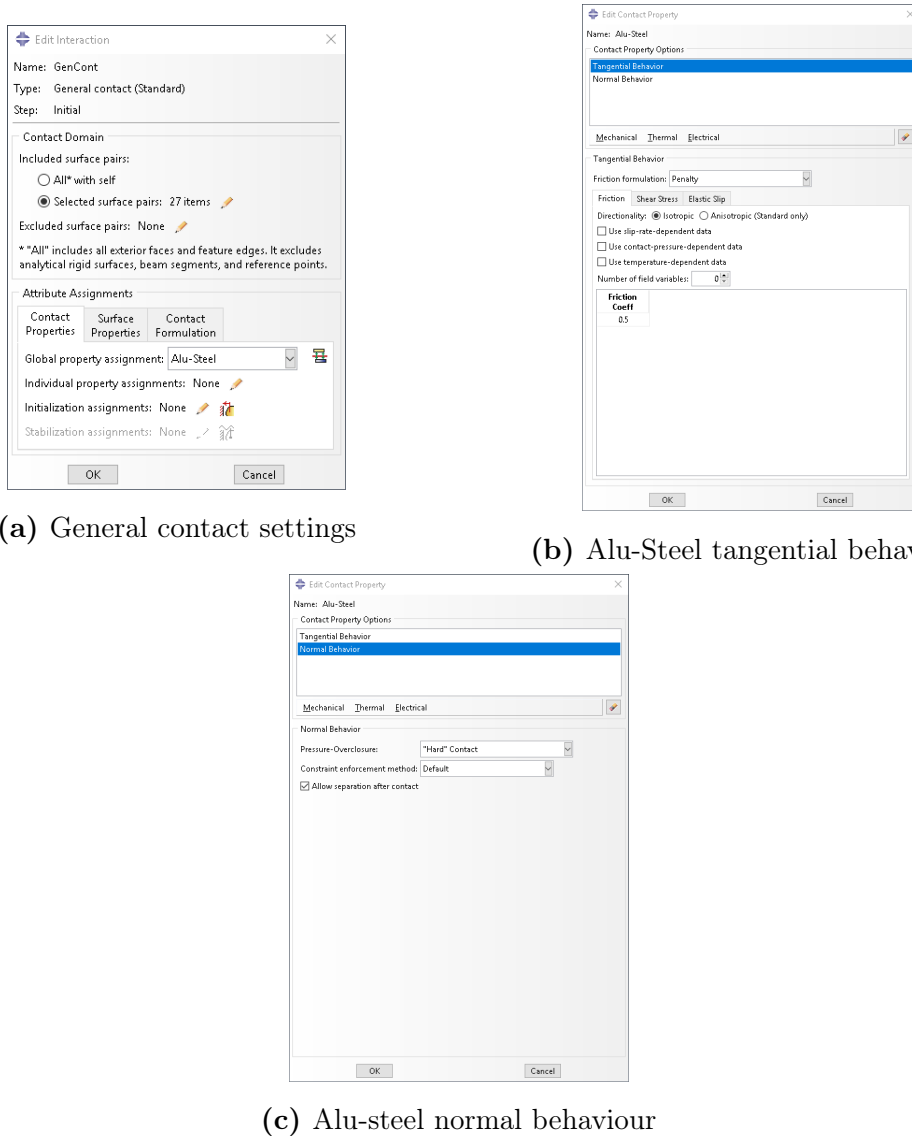


Figure A.8: Contact behaviour

As the interface thickness is thin (0.1mm), and the cohesive properties for a traction-separation law were not available, it was decided to use a tie constraint instead of a cohesive behaviour.

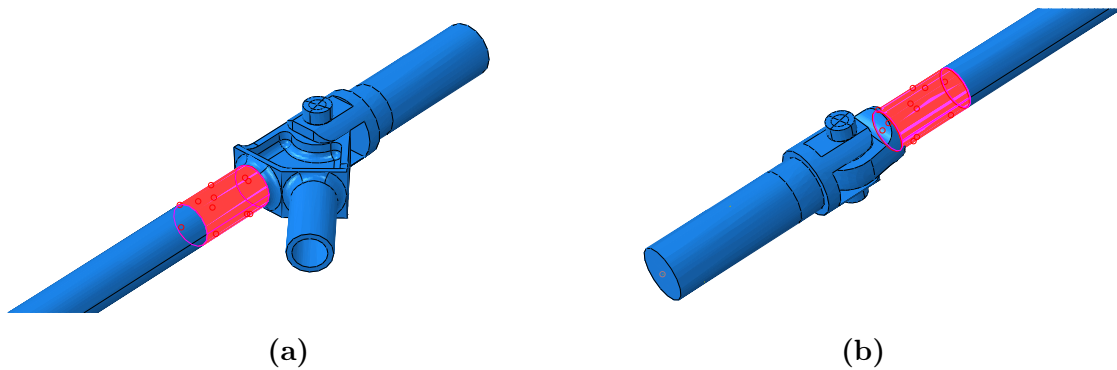
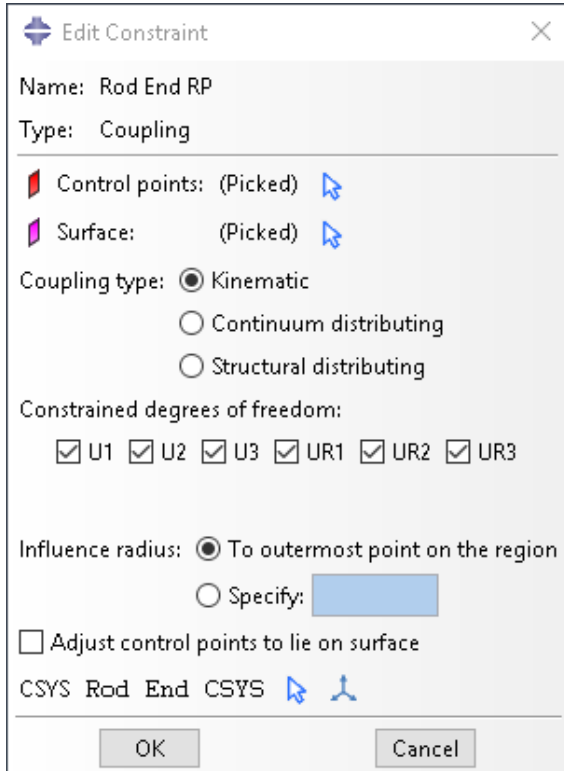
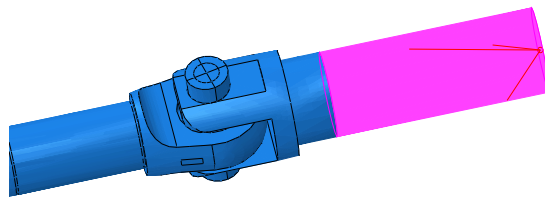


Figure A.9: Tie Constraints

To apply load at the correct location, a *kinematic coupling* has been used. The kinematic coupling is connected to a *reference point*, located at the center of the rod end clevis. It is then attached to the clevis surface as seen in figure. A.10.



(a) Kinematic coupling settings

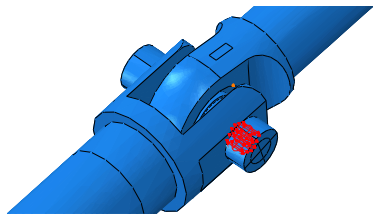


(b) Kinematic coupling assigned to clevis

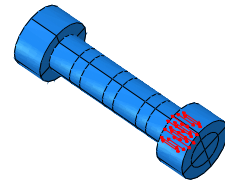
Figure A.10: Kinematic coupling

A.7 Loads and Boundary Conditions

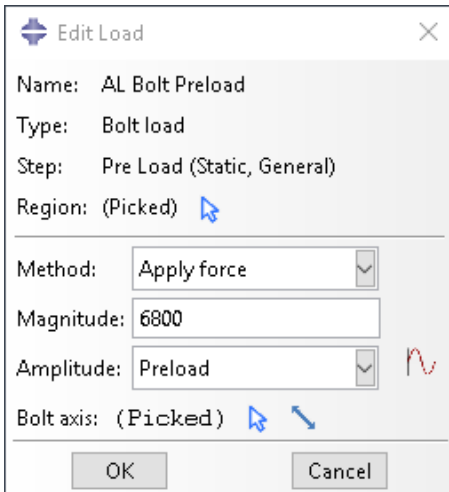
Three loads have been assigned to the model. Two *bolt loads* and one tensile *point load*. The bolt loads have been assigned in the preload step. A load of 6800 N is applied, corresponding to a tightening torque of 7.5 Nm. The preload is applied with an amplitude smooth step. This applies the load gradually.



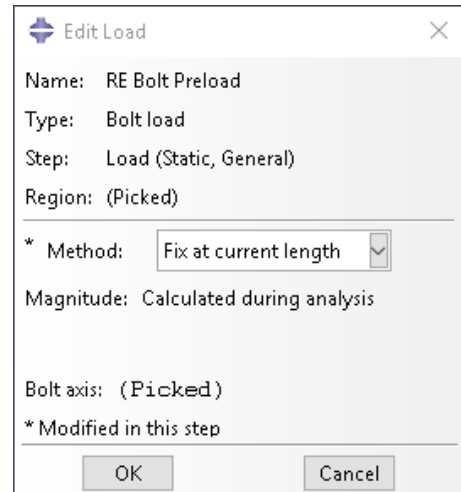
(a)



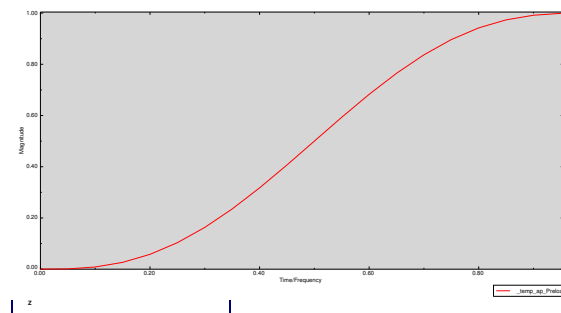
(b) Bolt load location



(c)



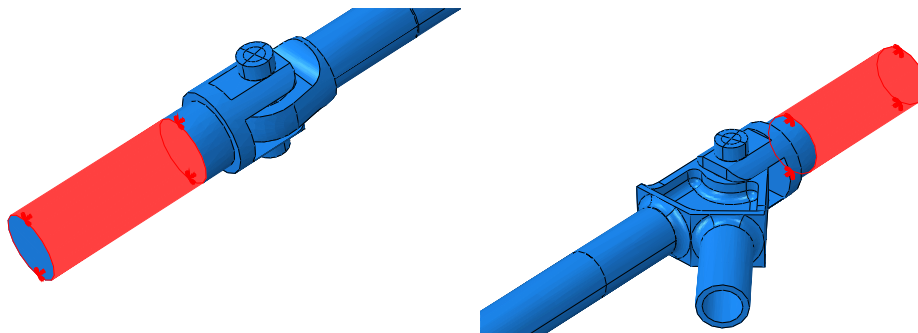
(d)



(e) smooth step amplitude

Figure A.11: Bolt Load

The tensile load has been applied at the rod end clevis through the reference point coupled to the rod end clevis surface, as mentioned. This surface also had a boundary condition only allowing displacement along the longitudinal axis of the assembly. The angle lock clevis has been held in place by a global encaster boundary condition. To achieve similar boundary conditions, each clevis has been partitioned so the boundary condition at each end can be applied according to the clamps in the Instron tensile machine. This can be seen in figure. A.12.



(a) Rod end clevis load and boundary condition
(b) Angle lock clevis boundary condition



(c) Clamping distance measure tensile machine marked

Figure A.12: Clevis BC

Each bearing has a retaining clip, holding the bearing in its place. This has been simulated by partitioning the bearing to the same overlap distance as the retaining ring.

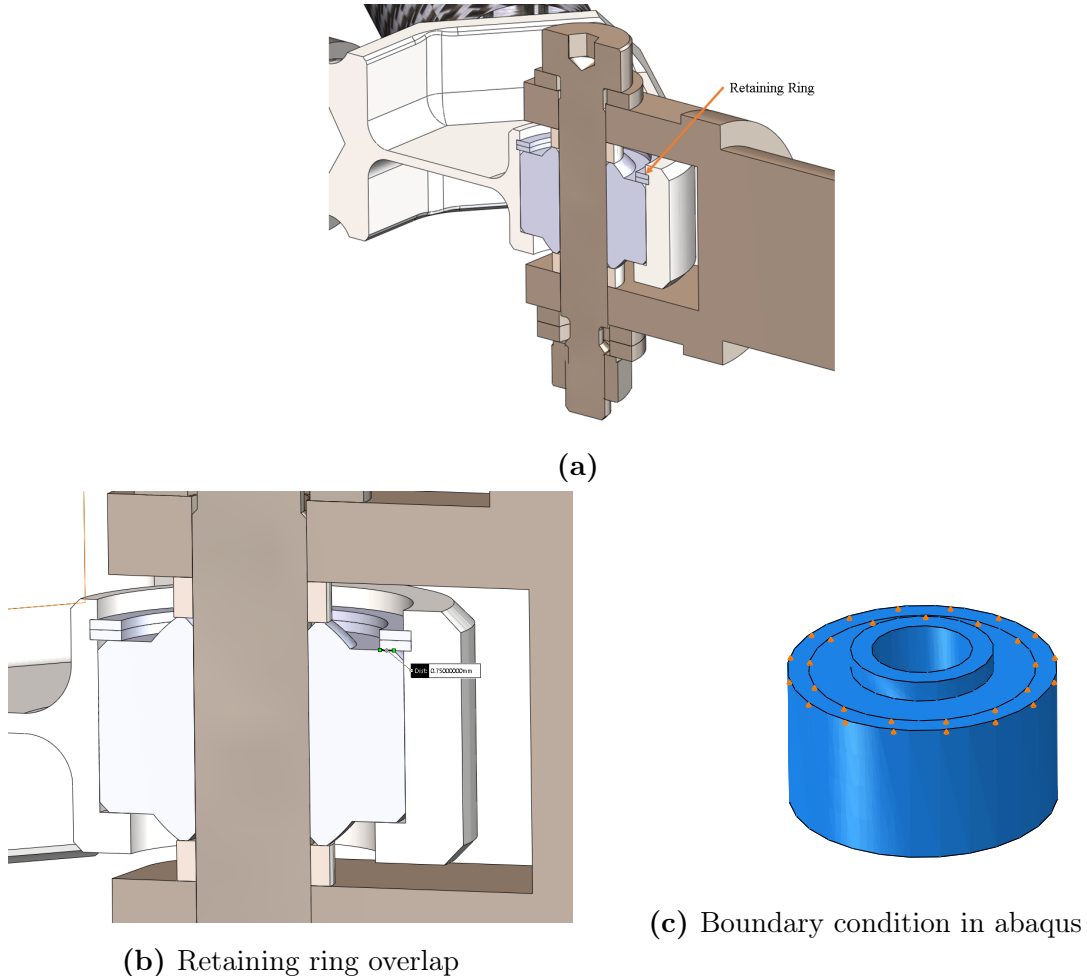


Figure A.13: Retaining ring BC

Boundary conditions were also applied to the rod end and angle lock during the preload step. These were removed in the load step. The model showed instabilities at the rod end clevis. This was countered by applying a boundary condition at the bearing as shown in figure

A.8 Mesh

The different parts have been meshed according to table A.4.

Mesh		
Parts	Element type	Number of Elements
Clevises	C3D10	27625
Angle lock	C3D10	17154
Rod End	C3D10	9110
CFRP Rod	S4	9110
Shoulder bolts	C3D8R	1344
Rod end spacers	C3D8R	416
Angle lock spacers	C3D10	1323
GE8C Dummy bearing	C3D10	2262
XRL Dummy bearing	C3D10	4034

Table A.4: Mesh characteristics of assembly

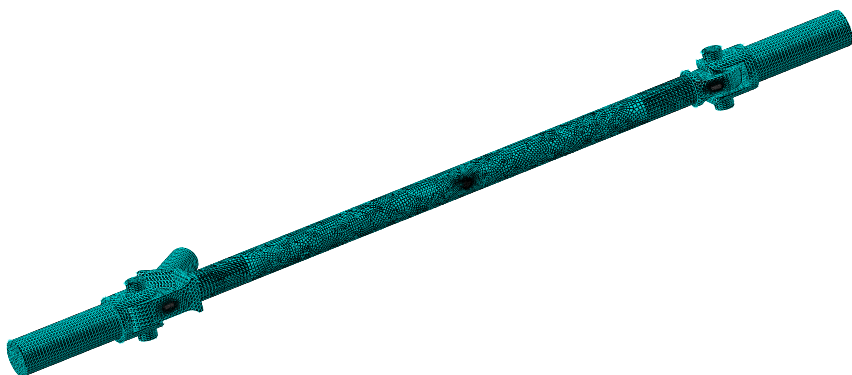


Figure A.14: Meshed assembly

Around the bolt holes of the clevis the mesh has been refined to 30 elements around the hole circumference.

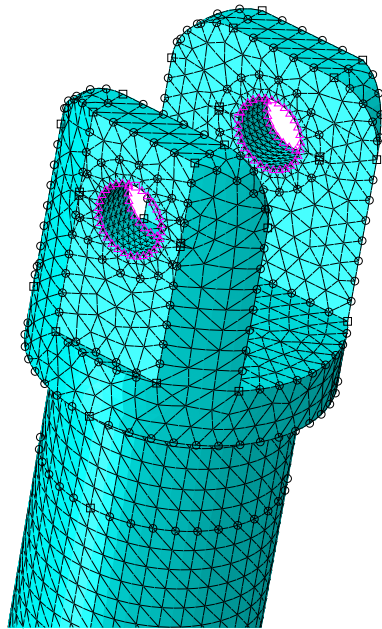


Figure A.15: Refinement around clevis hole

A.9 Results

The results presented with load of 7 kN. Since the model was imported in the coordinate system of the car, a transformation to the correct coordinate system has been made. See the legend in figure. A.16.

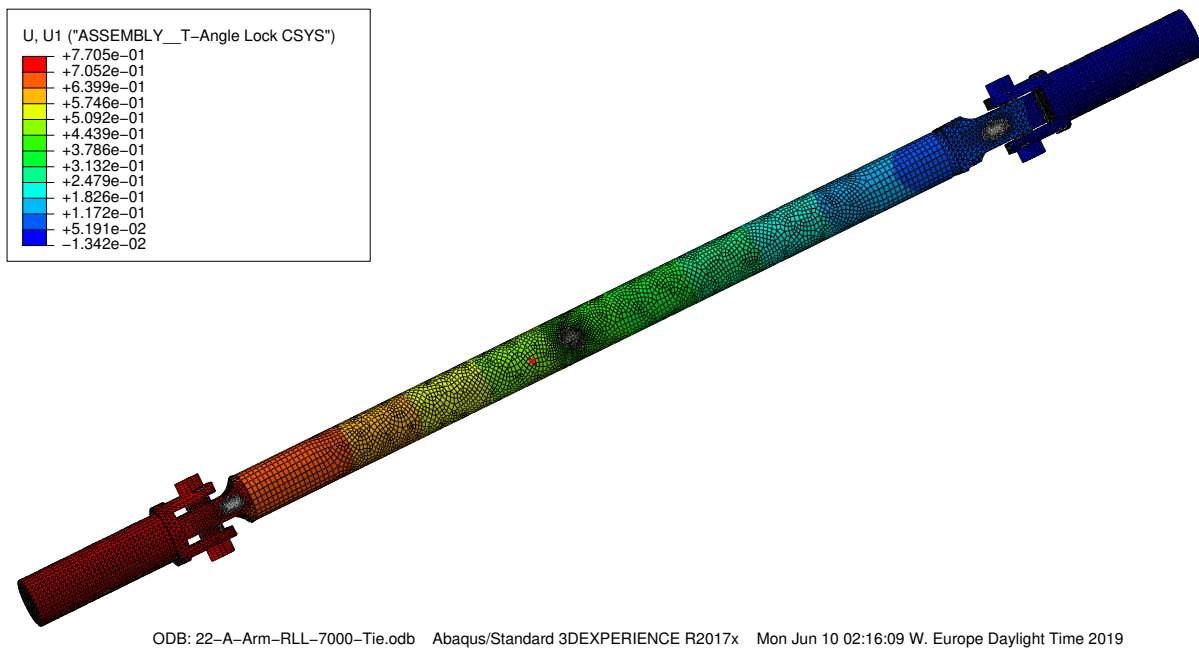
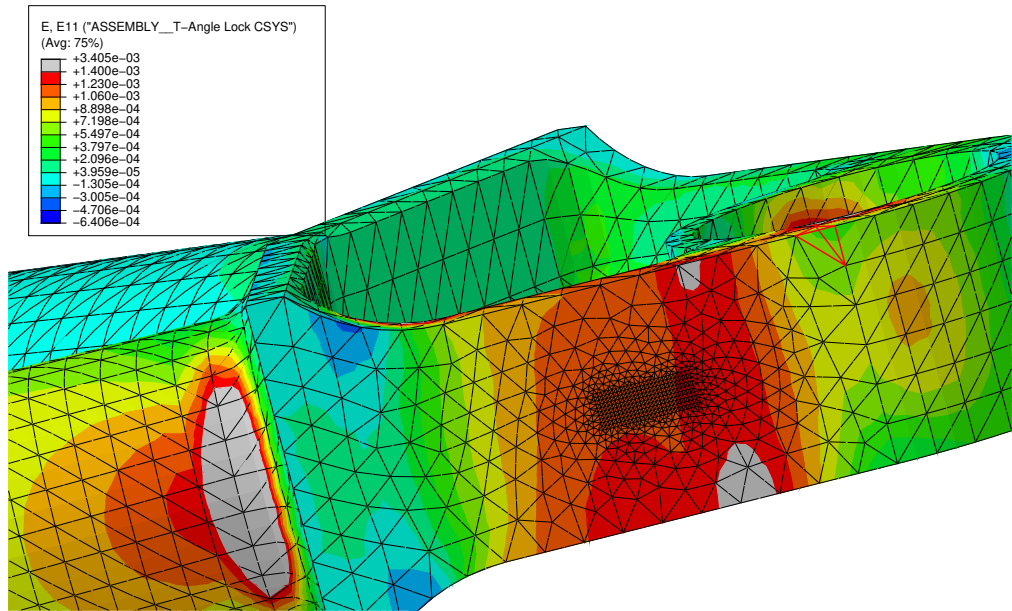
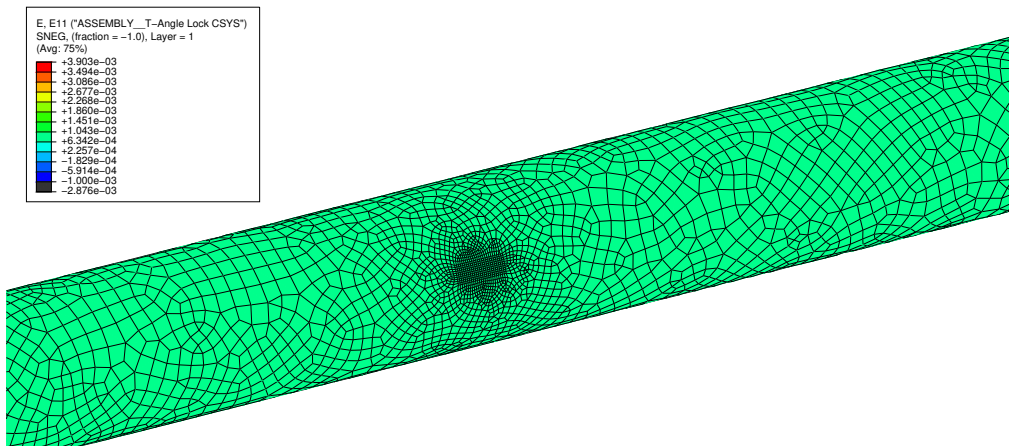


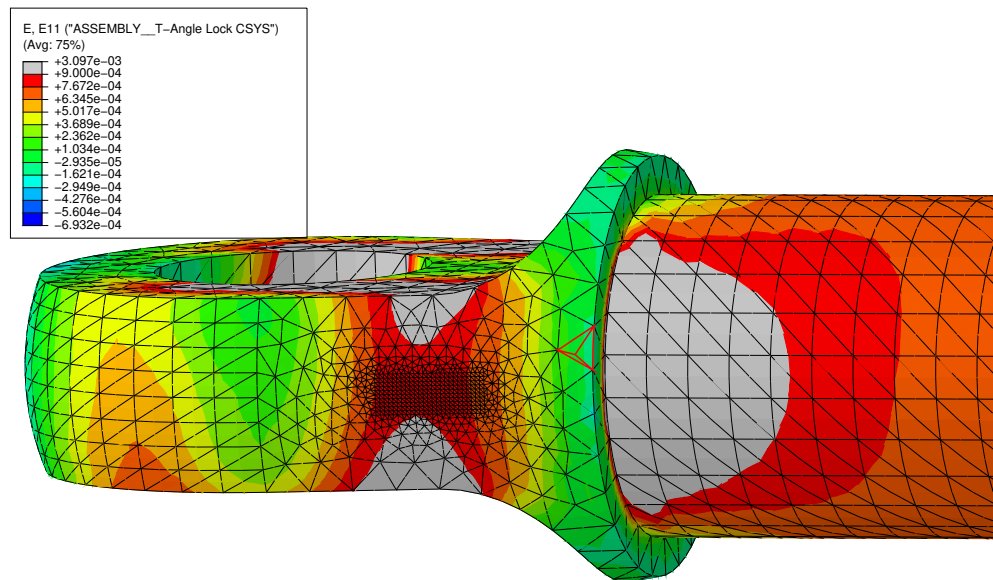
Figure A.16: Displacement along rod axis 7 kN load applied



(a) Angle lock strain gauge



(b) Rod strain gauge



(c) Rod end strain gauge

B The Compliance Model

Three scripts in total make the FE-spring model.

- mainRearLocal_Compliance.py
- functionsRearLocal_Compliance.py
- historyoutput.py

The input variables are set in the mainLocal_Compliance.py file. This then starts the model build up from the functionsRearLocal_Compliance.py file. The file builds the model and runs the coherent job in Abaqus CAE, before the displacement results from the analysis is printed to a .txt file. The history output file will not be documented as this is confidential.

B.1 Input Variables

The compliance model requires the suspension pickup points, contact patch, wheel center, loads and the stiffness of each suspension member.

```
#Spring Stiffness Upper A-arm
#Lateral Load: UpForeA = 15000
latload = [0, -2000, 0] UpAftA = 15000

#Spring Stiffness Lower A-arm
#Longitudinal Load LoForeA = 15000
longload = [2000, 0, 0] LoAftA = 15000

#Spring Stiffness Tie rod
#Vertical load Tie = 15000
vertload = [0, 0, 1000]
```

Table B.1: Loads at contact patch

Table B.2: Stiffness values for suspension members

```
# -*- coding: mbcs -*-

#Variables go here:

#RUF coordinates:
RUF = [-575, 268, 230.0754]

#RLA coordinates:
RLA = [-840, 223, 111.4586]

#RUA coordinates:
RUA = [-825, 242, 240.8754]

#RLF coordinates:
RLF = [-592, 251, 112.1346]

#Upright lower coordinates:
UpLo = [-764.4362, 571.3167, 139.5]

#Upright upper coordinates:
UpUp = [-764.7405, 535.894, 335.3958]

#Tierod mono coordinates:
TiMo = [-816, 233.9804, 156.8708]

#Upright tierod coordinates:
UpTi = [-858.1801, 554.0372, 213.0309]

#Contact point coordinates:
cp = [-765, 600, 10]

#Wheel Center
WC = [-765, 600, 238]
```

Figure B.1: Suspension pickup points

B.2 mainRearLocal_Compliance.py

```
# -*- coding: mbcs -*-

#Variables go here:

#RUF coordinates:
RUF = [-575, 268, 230.0754]

#RLA coordinates:
RLA = [-840, 223, 111.4586]

#RUA coordinates:
RUA = [-825, 242, 240.8754]

#RLF coordinates:
RLF = [-592, 251, 112.1346]

#Upright lower coordinates:
UpLo = [-764.4362, 571.3167, 139.5]

#Upright upper coordinates:
UpUp = [-764.7405, 535.894, 335.3958]

#Tierod mono coordinates:
TiMo = [-816, 233.9804, 156.8708]

#Upright tierod coordinates:
UpTi = [-858.1801, 554.0372, 213.0309]

#Contact point coordinates:
cp = [-765, 600, 10]

#Wheel Center
WC = [-765, 600, 238]

#Lateral Load:
latload = [0, -2000, 0]

#Longitudinal Load
longload = [2000, 0, 0]

#Vertical load
vertload = [0, 0, 1000]

#Spring Stiffness Upper A-arm
UpForeA = 15000
UpAftA = 15000

#Spring Stiffness Lower A-arm
LoForeA = 15000
LoAftA = 15000

#Spring Stiffness Tie rod
Tie = 15000

from part import *
from material import *
from section import *
from assembly import *
from step import *
from interaction import *
from load import *
```

```

from mesh import *
from optimization import *
from job import *
from sketch import *
from visualization import *
from connectorBehavior import *
from abaqus import*
from abaqusConstants import*
import functionsRearLocal_Compliance
reload(functionsRearLocal_Compliance)
import historyOutput
reload(historyOutput)

#Open a new mdb and close all the open odbs:
Mdb()
for odb in session.odbs.values():
    odb.close()

#Close old file
open('Displacement.txt', 'w').close()

functionsRearLocal_Compliance.make_jobs(RLF, RLA, RUF, RUA, TiMo, UpUp,
    UpLo, UpTi, cp, WC, latload, longload, vertload, UpForeA, UpAftA,
    LoForeA, LoAftA, Tie)

```

B.3 functionsRearLocal_Compliance.py

```

from part import *
from material import *
from section import *
from assembly import *
from step import *
from interaction import *
from load import *
from mesh import *
from optimization import *
from job import *
from sketch import *
from visualization import *
from connectorBehavior import *
from abaqusConstants import*
import math
import historyOutput
reload(historyOutput)

#Function for setting up the model:
def make_front_model(RLF, RLA, RUF, RUA, TiMo, UpUp, UpLo, UpTi, cp, WC,
    UpForeA, UpAftA, LoForeA, LoAftA, Tie):

    model = mdb.models['Model-1']
    model.StaticStep(name='Step-1', previous='Initial')
    ra =model.rootAssembly

    #Make the Points:

    model.Part(dimensionality=THREE_D, name='Part-1', type=DEFORMABLE_BODY)
    model.parts['Part-1'].ReferencePoint(point=(0.0, 0.0, 0.0))
    ra.ReferencePoint(point=RUF)
    ra.features.changeKey(fromName='RP-1', toName= 'RUF')
    ra.ReferencePoint(point=RLF)
    ra.features.changeKey(fromName='RP-1', toName='RLF')

```

```

ra.ReferencePoint(point=RUA)
ra.features.changeKey(fromName='RP-1', toName='RUA')
ra.ReferencePoint(point=RLA)
ra.features.changeKey(fromName='RP-1', toName='RLA')
ra.ReferencePoint(point=UpLo)
ra.features.changeKey(fromName='RP-1', toName='Upright lower')
ra.ReferencePoint(point=UpUp)
ra.features.changeKey(fromName='RP-1', toName='Upright upper')
ra.ReferencePoint(point=TiMo)
ra.features.changeKey(fromName='RP-1', toName='Tierod mono')
ra.ReferencePoint(point=UpTi)
ra.features.changeKey(fromName='RP-1', toName='Upright tierod')
ra.ReferencePoint(point=cp)
ra.features.changeKey(fromName='RP-1', toName='Contact point')
ra.ReferencePoint(point=WC)
ra.features.changeKey(fromName='RP-1', toName='WC')

#Make wires:

# ra.WirePolyLine(mergeType=IMPRINT, meshable=OFF, points=((ra.
#     referencePoints[6], ra.referencePoints[1]), ))
# ra.Set(edges=ra.edges.getSequenceFromMask(([#3 ], ), ), name='Wire
# -1-Set-1')
# ra.features.changeKey(fromName='Wire-1', toName='Upper A-arm')
# ra.sets.changeKey(fromName='Wire-1-Set-1', toName='Upper A-arm')
# ra.WirePolyLine(mergeType=IMPRINT, meshable=OFF, points=((ra.
#     referencePoints[4], ra.referencePoints[5]),
#     (ra.referencePoints[5], ra.referencePoints[2])))
# ra.Set(edges=ra.edges.getSequenceFromMask(([#3 ], ), ), name='Wire
# -1-Set-1')
# ra.features.changeKey(fromName='Wire-1', toName='Lower A-arm')
# ra.sets.changeKey(fromName='Wire-1-Set-1', toName='Lower A-arm')
ra.WirePolyLine(mergeType=IMPRINT, meshable=OFF, points=((ra.
    referencePoints[5], ra.referencePoints[6]),
    (ra.referencePoints[6], ra.referencePoints[8]),(ra.referencePoints[5],
    ra.referencePoints[8]),(ra.referencePoints[8], ra.referencePoints
    [10]), ))
ra.Set(edges=ra.edges.getSequenceFromMask(([#1 ], ), ), name='Upright
')
ra.features.changeKey(fromName='Wire-1', toName='Upright')
ra.WirePolyLine(mergeType=IMPRINT, meshable=OFF, points=((ra.
    referencePoints[8], ra.referencePoints[10]), (
ra.referencePoints[5], ra.referencePoints[10]), (ra.referencePoints[6],
    ra.referencePoints[10])))
ra.Set(edges=ra.edges.getSequenceFromMask(([#7 ], ), ), name='Wire-1-
Set-1')
ra.features.changeKey(fromName='Wire-1', toName='Wheel')
ra.sets.changeKey(fromName='Wire-1-Set-1', toName='Wheel')

# Make Springs
#UpAftA
ra.engineeringFeatures.TwoPointSpringDashpot(axis=NODAL_LINE,
    dashpotBehavior=OFF, dashpotCoefficient=0.0, name='RUA Spring',
    regionPairs=((Region(referencePoints=(ra.referencePoints[3], )),
        Region(
    referencePoints=(ra.referencePoints[6], ))), ), springBehavior=ON,
    springStiffness=UpAftA)

#UpForeA
ra.engineeringFeatures.TwoPointSpringDashpot(axis=NODAL_LINE,
    dashpotBehavior=OFF, dashpotCoefficient=0.0, name='RUF Spring',
    regionPairs=((Region(referencePoints=(ra.referencePoints[1], )),

```

```

    Region(
        referencePoints=(ra.referencePoints[6], )), ), springBehavior=ON,
        springStiffness=UpForeA)

#LoAftA
ra.engineeringFeatures.TwoPointSpringDashpot(axis=NODAL_LINE,
    dashpotBehavior=OFF, dashpotCoefficient=0.0, name='RLA Spring',
    regionPairs=((Region(referencePoints=(ra.referencePoints[4], )),
        Region(
            referencePoints=(ra.referencePoints[5], )), ), springBehavior=ON,
        springStiffness=LoAftA)

#LoForeA
ra.engineeringFeatures.TwoPointSpringDashpot(axis=NODAL_LINE,
    dashpotBehavior=OFF, dashpotCoefficient=0.0, name='RLF Spring',
    regionPairs=((Region(referencePoints=(ra.referencePoints[2], )),
        Region(
            referencePoints=(ra.referencePoints[5], )), ), springBehavior=ON,
        springStiffness=LoForeA)

# Tierod
ra.engineeringFeatures.TwoPointSpringDashpot(axis=NODAL_LINE,
    dashpotBehavior=OFF, dashpotCoefficient=0.0, name='Tierod Spring',
    regionPairs=((Region(referencePoints=(ra.referencePoints[8], )),
        Region(
            referencePoints=(ra.referencePoints[7], )), ), springBehavior=ON,
        springStiffness=Tie)

#Make the coupling for the contact patch of the force:
# ra.referencePoints[5], ra.referencePoints[8],
# ra.referencePoints[10], ra.referencePoints[9],
model.Coupling(controlPoint=ra.sets['AtPoint'], couplingType=KINEMATIC,
    influenceRadius=WHOLE_SURFACE, localCsys=None, name='Wheel',
    surface=ra.sets['UprightNodes'],
    u1=ON, u2=ON, u3=ON, ur1=ON, ur2=ON, ur3=ON)

#Make links and beams for whole model:
ra.Set(edges=ra.edges.getSequenceFromMask(['[#83e1003 #1f '], ), ),
    name='Beams')
ra.Set(edges=ra.edges.getSequenceFromMask(['[#f7c1effc '], ), ), name='Links')
model.ConnectorSection(name='Link', translationalType=LINK)
model.ConnectorSection(assembledType=BEAM, name='Beam')
ra.SectionAssignment(region=ra.sets['Beams'], sectionName='Link')
ra.SectionAssignment(region=ra.sets['Links'], sectionName='Link')

# Make localCsys for forces:
# ra.DatumCsysByThreePoints(coordSysType=CARTESIAN, name='RUFCSYS',
#     origin= RUF, point1= RUF_x, point2=RUF_y)
# ra.DatumCsysByThreePoints(coordSysType=CARTESIAN, name='RUACSYS',
#     origin= RUA, point1= RUA_x, point2=RUA_y)
# ra.DatumCsysByThreePoints(coordSysType=CARTESIAN, name='TieCSYS',
#     origin= TiMo, point1= TiMo_x, point2=TiMo_y)

#Make sets for historyOutputRequests:
ra.Set(name='RUALEFT', referencePoints=(ra.referencePoints[3], ))
ra.Set(name='RUFLEFT', referencePoints=(ra.referencePoints[1], ))
ra.Set(name='RLALEFT', referencePoints=(ra.referencePoints[4], ))
ra.Set(name='RLFLEFT', referencePoints=(ra.referencePoints[2], ))
ra.Set(name='TierodMonoLEFT', referencePoints=(ra.referencePoints[7], ))

```

```

        ra.Set(name='UPLO', referencePoints=(ra.referencePoints[5], ))
        ra.Set(name='UPTI', referencePoints=(ra.referencePoints[8], ))
        ra.Set(name='UPUP', referencePoints=(ra.referencePoints[6], ))
        ra.Set(name='CP', referencePoints=(ra.referencePoints[9], ))

#Make monocoque BC:
        ra.Set(name='Monopoints', referencePoints=(ra.referencePoints[1], ra.
            referencePoints[2], ra.referencePoints[3],
            ra.referencePoints[4], ra.referencePoints[7]))
        model.DisplacementBC(amplitude=UNSET, createStepName='Initial',
            distributionType=UNIFORM, fieldName='',
            fixed=OFF, localCsys=None, name='Mono', region=ra.sets['Monopoints'],
            u1=0.0, u2=0.0, u3=0.0, ur1=UNSET, ur2=UNSET, ur3=UNSET)
        model.DisplacementBC(amplitude=UNSET, createStepName='Initial',
            distributionType=UNIFORM, fieldName='',
            fixed=OFF, localCsys=None, name='CP', region=ra.sets['CP'], u1=0.0,
            u2=UNSET, u3=0.0, ur1=0.0, ur2=0.0, ur3=0.0)

#History output requests:

        model.FieldOutputRequest(createStepName='Step-1', name='Displacement in
            Upright', variables=('U',))

    del model.historyOutputRequests['H-Output-1']

#Upright Lower Point
    model.HistoryOutputRequest(createStepName='Step-1', frequency=
        LAST_INCREMENT, name='UPLO', rebar=EXCLUDE, region=
        ra.sets['UPLO'], sectionPoints=DEFAULT, variables=('U1', 'U2', 'U3'
        ))

#Upright Lower Point
    model.HistoryOutputRequest(createStepName='Step-1', frequency=
        LAST_INCREMENT, name='UPUP', rebar=EXCLUDE, region=
        ra.sets['UPUP'], sectionPoints=DEFAULT, variables=('U1', 'U2', 'U3'
        ))

#Tie Rod Point
    model.HistoryOutputRequest(createStepName='Step-1', frequency=
        LAST_INCREMENT, name='UPTI', rebar=EXCLUDE, region=
        ra.sets['UPTI'], sectionPoints=DEFAULT, variables=('U1', 'U2', 'U3'
        ))

    return model

#Copyinng of model and dataextraction
def make_jobs(RLF, RLA, RUF, RUA, TiMo, UpUp, UpLo, UpTi, cp, WC, latload,
    longload, vertload, UpForeA, UpAftA, LoForeA, LoAftA, Tie):

    model = make_front_model(RLF, RLA, RUF, RUA, TiMo, UpUp, UpLo, UpTi, cp
        , WC, UpForeA, UpAftA, LoForeA, LoAftA, Tie)

    # Copy model and apply loads:
    LatLoad = mdb.Model(name='Lateral Load', objectToCopy=model)
    LatLoad.ConcentratedForce(cf1=latload[0], cf2=latload[1], cf3=latload
        [2], createStepName='Step-1', distributionType=UNIFORM, field='',
        localCsys=None, name='Lateral Load', region=model.rootAssembly.sets
        ['AtPoint'])

    LongLoad = mdb.Model(name='Longitudinal Load', objectToCopy=model)
    LongLoad.ConcentratedForce(cf1=longload[0], cf2=longload[1], cf3=
        longload[2], createStepName='Step-1', distributionType=UNIFORM,
        field='')

```

```

        localCsys=None, name='Longitudinal Load', region=model.rootAssembly
        .sets['AtPoint'])
VertLoad = mdb.Model(name='Vertical Load', objectToCopy=model)
VertLoad.ConcentratedForce(cf1=vertload[0], cf2=vertload[1], cf3=
    vertload[2], createStepName='Step-1', distributionType=UNIFORM,
    field='',
    localCsys=None, name='Vertical Load', region=model.rootAssembly.
    sets['AtPoint'])

# Make jobs for the analysis:
mdb.Job(model='Lateral Load', name='Lateral-Load')
mdb.Job(model='Longitudinal Load', name='Longitudinal-Load')
mdb.Job(model='Vertical Load', name='Vertical-Load')

# Submit all the jobs, wait for them to complete, then open the
corresponding odb:

# mdb.jobs['Acceleration'].submit(consistencyChecking=OFF)
# mdb.jobs['Acceleration'].waitForCompletion()
# openOdb('Acceleration.odb')

# mdb.jobs['Brake110kph'].submit(consistencyChecking=OFF)
# mdb.jobs['Brake110kph'].waitForCompletion()
# openOdb('Brake110kph.odb')

# mdb.jobs['Bump2g+brake'].submit(consistencyChecking=OFF)
# mdb.jobs['Bump2g+brake'].waitForCompletion()
# openOdb('Bump2g+brake.odb')

# mdb.jobs['Bump2g+turn'].submit(consistencyChecking=OFF)
# mdb.jobs['Bump2g+turn'].waitForCompletion()
# openOdb('Bump2g+turn.odb')

# mdb.jobs['Bump3g'].submit(consistencyChecking=OFF)
# mdb.jobs['Bump3g'].waitForCompletion()
# openOdb('Bump3g.odb')

mdb.jobs['Lateral-Load'].submit(consistencyChecking=OFF)
mdb.jobs['Lateral-Load'].waitForCompletion()
openOdb('Lateral-Load.odb')

#Process all data:
RLALC =
UpLo_U = [0, 0, 0]
UpUp_U = [0, 0, 0]
UpTi_U = [0, 0, 0]

# loop over all open odbs
for odb in session.odbs.values():
    # set current ODB
    session.viewports['Viewport: 1'].setValues(displayedObject=odb)

    # Extract Curves from History Output for momentDisplacement and
    # momentStress
    xyData = historyOutput.HistoryOutput(maxPoints=None)

    # UpLo
    UpLo_U1 = xyData.getHistoryCurve(("UPL0", "U1"))
    UpLo_U2 = xyData.getHistoryCurve(("UPL0", "U2"))
    UpLo_U3 = xyData.getHistoryCurve(("UPL0", "U3"))
    UpLo_U = [UpLo_U1[-1][1], UpLo_U2[-1][1], UpLo_U3[-1][1]]

```

```

# UpUp
UpUp_U1 = xyData.getHistoryCurve(("UPUP", "U1"))
UpUp_U2 = xyData.getHistoryCurve(("UPUP", "U2"))
UpUp_U3 = xyData.getHistoryCurve(("UPUP", "U3"))
UpUp_U = [UpUp_U1[-1][1], UpUp_U2[-1][1], UpUp_U3[-1][1]]

# UpTi
UpTi_U1 = xyData.getHistoryCurve(("UPTI", "U1"))
UpTi_U2 = xyData.getHistoryCurve(("UPTI", "U2"))
UpTi_U3 = xyData.getHistoryCurve(("UPTI", "U3"))
UpTi_U = [UpTi_U1[-1][1], UpTi_U2[-1][1], UpTi_U3[-1][1]]

fout = open("Displacement.txt", "a")
fout.write("Displacement of Upright Points:\n")
fout.write("\t\tU1\t\tU2\t\tU3\t\tLoadcase:\n")
fout.write("%s\t\t%f\t\t%f\t\t%f\t\t%f\t\t%s\n" % (UpLo_U[0], UpLo_U[1],
                                                UpLo_U[2], odb.name))
fout.write("%s\t\t%f\t\t%f\t\t%f\t\t%f\t\t%f\t\t%s\n" % (UpUp_U[0], UpUp_U[1],
                                                       UpUp_U[2], RLALC))
fout.write("%s\t\t%f\t\t%f\t\t%f\t\t%f\t\t%f\t\t%s\n" % (UpTi_U[0], UpTi_U[1],
                                                       UpTi_U[2], RLALC))

fout.close()

```

C Data sheets

C.1 T700s Fiber

C.2 UF3369 Resin

C.3 Araldite 4859

C.4 HBM Quantum MX1615

C.5 TML FLAB-3-11-3LJCT-F

C.6 ASKF GE8C

C.7 Sarma XRL

TORAYCA® T700S DATA SHEET

Highest strength, standard modulus fiber available with excellent processing characteristics for filament winding and prepreg. This never twisted fiber is used in high tensile applications like pressure vessels, recreational, and industrial.

FIBER PROPERTIES

		English	Metric	Test Method
Tensile Strength		711 ksi	4,900 MPa	TY-030B-01
Tensile Modulus		33.4 Msi	230 GPa	TY-030B-01
Strain		2.1 %	2.1 %	TY-030B-01
Density		0.065 lbs/in ³	1.80 g/cm ³	TY-030B-02
Filament Diameter		2.8E-04 in.	7 µm	
Yield	6K	3,724 ft/lbs	400 g/1000m	TY-030B-03
	12K	1,862 ft/lbs	800 g/1000m	TY-030B-03
	24K	903 ft/lbs	1,650 g/1000m	TY-030B-03
Sizing Type	50C		1.0 %	TY-030B-05
& Amount	60E		0.3 %	TY-030B-05
	FOE		0.7 %	TY-030B-05
Twist		Never twisted		

FUNCTIONAL PROPERTIES

CTE	-0.38 α·10 ⁻⁶ /°C
Specific Heat	0.18 Cal/g·°C
Thermal Conductivity	0.0224 Cal/cm·s·°C
Electric Resistivity	1.6 x 10 ⁻³ Ω·cm
Chemical Composition: Carbon	93 %
Na + K	<50 ppm

COMPOSITE PROPERTIES *

Tensile Strength	370 ksi	2,550 MPa	ASTM D-3039
Tensile Modulus	20.0 Msi	135 GPa	ASTM D-3039
Tensile Strain	1.7 %	1.7 %	ASTM D-3039
Compressive Strength	215 ksi	1,470 MPa	ASTM D-695
Flexural Strength	245 ksi	1,670 MPa	ASTM D-790
Flexural Modulus	17.5 Msi	120 GPa	ASTM D-790
ILSS	13 ksi	9 kgf/mm ²	ASTM D-2344
90° Tensile Strength	10.0 ksi	69 MPa	ASTM D-3039

* Toray 250°F Epoxy Resin. Normalized to 60% fiber volume.

T700S

COMPOSITE PROPERTIES **

Tensile Strength	355 ksi	2,450 MPa	ASTM D-3039
Tensile Modulus	18.0 Msi	125 GPa	ASTM D-3039
Tensile Strain	1.7 %	1.7 %	ASTM D-3039
Compressive Strength	230 ksi	1,570 MPa	ASTM D-695
Compressive Modulus	--- Msi	--- GPa	ASTM D-695
In-Plane Shear Strength	14 ksi	98 MPa	ASTM D-3518
ILSS	15.5 ksi	11 kgf/mm ²	ASTM D-2344
90° Tensile Strength	10.0 ksi	70 MPa	ASTM D-3039

** Toray Semi-Toughened 350°F Epoxy Resin. Normalized to 60% fiber volume.

See Section 4 for Safety & Handling information. The above properties do not constitute any warranty or guarantee of values. These values are for material selection purposes only. For applications requiring guaranteed values, contact our sales and technical team to establish a material specification document.

PACKAGING

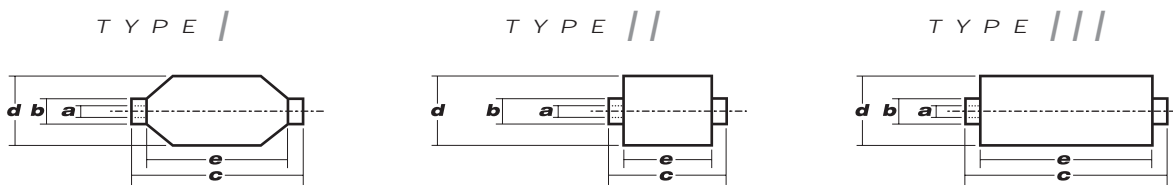
The table below summarizes the tow sizes, twists, sizing types, and packaging available for standard material. Other bobbin sizes may be available on a limited basis.

Tow Sizes	Twist ¹	Sizing	Bobbin Net Weight (kg)	Bobbin Type ²	a	b	c	d	e	Spools per Case	Case Net Weight (kg)
6K	C	50C	2.0	///	76.5	82.5	280	140	252	12	24
	C	50C	6.0	///	76.5	82.5	280	200	252	4	24
12K	C	60E	6.0	///	76.5	82.5	280	200	252	4	24
	C	FOE	6.0	///	76.5	82.5	280	200	252	4	24
24K	C	50C	6.0	///	76.5	82.5	280	200	252	4	24
	C	60E	6.0	///	76.5	82.5	280	200	252	4	24
	C	FOE	6.0	///	76.5	82.5	280	200	252	4	24

¹ Twist A: Twisted yarn B: Untwisted yarn made from a twisted yarn through an untwisting process

C: Never twisted yarn

² Bobbin Type See Diagram below



TORAY CARBON FIBERS AMERICA, INC.

6 Hutton Centre Drive, Suite #1270, Santa Ana, CA 92707 TEL: (714) 431-2320 FAX: (714) 424-0750
Sales@Toraycfa.com Technical@Toraycfa.com www.torayusa.com

UF3369 TCR™ Resin

June 2007, Revision 10

TCR Composites offers a unique thermosetting Bisphenol A epoxy matrix resin system featuring a **3-month shelf life without refrigeration**. This resin is currently used for tow/roving, unitape, and fabric, and is available for carbon, glass, aramid, and other fibers. Resin content, resin flow during cure, and tack levels can be tailored to suit your process requirements.

Neat Resin Properties and Applications

Density (g/cc)	Tg (°F/°C) (from G'' DMA curve)	Tensile Modulus (ksi/GPa)	Tensile Strength (ksi/MPa)	Elongation at Break (%)	Tg after 24-Hr Water-Boil (°F/°C)	Water Absorption (%)	Available Fiber Form
1.18	242 / 117	417 / 2.83	10.9 / 68.9	5.3	152 / 67	5.1	Tow/Roving, Unitape, Fabric

Typical Use

High pressure SCBA tanks, rocket motor cases, sporting goods, infrastructure repair, etc., where moderately low-temperature cure is required. High translation/performance in pressure vessels when used with Toray T700SC, Toho G30-700 and Mitsubishi TRH-50 and most other Carbon fibers.

Cure*

There are three recommended cure cycles for UF3369 resin. All three will produce similar properties.

1. $\leq 5^{\circ}\text{F}$ -per-minute ramp up to 250°F (121°C), hold for 1.5 hours, $< 5^{\circ}\text{F}$ -per-minute ramp down to at least 150°F (66°C) before removing from oven.
2. $\leq 5^{\circ}\text{F}$ -per-minute ramp up to 230°F (110°C), hold for 4 hours, $< 5^{\circ}\text{F}$ -per-minute ramp down to at least 150°F (66°C) before removing from oven.
3. $\leq 5^{\circ}\text{F}$ -per-minute ramp up to 210°F (99°C), hold for 24 hours, $< 5^{\circ}\text{F}$ -per-minute ramp down to at least 150°F (66°C) before removing from oven.

*Higher temperatures and shorter hold times should also work but have not yet been thoroughly tested.

Storage Requirements

The preimpregnated materials manufactured from this resin shall remain sealed and stored in the original package. The material is to be stored indoors, out of the weather.

The shelf life is 3 months from the date of manufacture when the maximum storage temperature shall not exceed 75°F (24°C).

The shelf life is 1.5 months from the date of manufacture when the maximum storage temperature shall not exceed 90°F (32°C).

The shelf life is 6 months from the date of manufacture when the maximum storage temperature shall not exceed 40°F (4°C), with an additional 2 months at $\leq 75^{\circ}\text{F}$ (24°C).

The shelf life is 18 months from the date of manufacture when the maximum storage temperature shall not exceed 0°F (-18°C), with an additional 2 months at $\leq 75^{\circ}\text{F}$ (24°C)

The values here represent expected ranges based on actual test data. Since the values are specimen-preparation- and test-method-dependent, TCR Composites cannot guarantee that these properties will be obtained in all cases. The data should be used as an indication only, since part or component properties are highly equipment- and process-dependent. It is recommended that end users determine the suitability of this material for each application through their own testing and evaluation. **TCR™** is a trademark of TCR Composites, Inc.

Advanced Materials

Araldite® AW4859/ Hardener HW4859

Structural Adhesives

ARALDITE® AW4859/ Hardener HW4859

Two component epoxy adhesive system

Key properties

- Very high lap shear
- Bonds a wide variety of materials (metal, composite and thermoplastics)
- Temperature resistant up to 140°C
- Extremly tough and resilient adhesive

Description

ARALDITE® AW4859/ Hardener HW4859 is a two-component, epoxy adhesive paste of high strength and toughness. Performances can be enhanced by post-curing at elevated temperature. It has been designed to perfectly bond onto composites , especially CFRP but it is suitable for bonding a wide variety of metals, ceramics and many other substrates in common use.

Product data

Property	Araldite® AW4859	Hardener HW4859	Mixed Adhesive
Colour (visual)	Black	Yellowish	Black
Specific gravity	1.2	1.0	approx. 1.1
Viscosity at 25 °C (Pa.s)	80 - 100	10 - 15	thixotropic
Pot Life (100 gm at 25°C)			100 -120 min

Processing

Pretreatment

The strength and durability of a bonded joint are dependent on proper treatment of the surfaces to be bonded.

At the very least, joint surfaces should be cleaned with a good degreasing agent such as acetone, iso-propanol (for plastics) or other proprietary degreasing agents in order to remove all traces of oil, grease and dirt.

Low grade alcohol, gasoline (petrol) or paint thinners should never be used.

The strongest and most durable joints are obtained by either mechanically abrading or chemically etching ("pickling") the degreased surfaces. Abrading should be followed by a second degreasing treatment

Mix ratio	Parts by weight	Parts by volume
Araldite® AW4859	100	100
Hardener HW4859	43	50

The resin and hardener should be blended until they form a homogeneous mix.

Araldite® AW4859/Hardener HW4859 is available in cartridges incorporating mixers and can be applied as ready to use adhesive with the aid of the tool recommended by Huntsman Advanced Materials

Application of adhesive

The resin/hardener mix is applied with a spatula, to the pretreated and dry joint surfaces.

A layer of adhesive 0.05 to 0.10 mm thick will normally impart the greatest lap shear strength to the joint.

The joint components should be assembled and clamped as soon as the adhesive has been applied. An even contact pressure throughout the joint area will ensure optimum cure.

Mechanical processing

Specialist firms have developed metering, mixing and spreading equipment that enables the bulk processing of adhesive.

We will be pleased to advise customers on the choice of equipment for their particular needs.

Equipment maintenance

All tools should be cleaned with hot water and soap before adhesives residues have had time to cure. The removal of cured residues is a difficult and time-consuming operation.

If solvents such as acetone are used for cleaning, operatives should take the appropriate precautions and, in addition, avoid skin and eye contact.

Times to minimum shear strength

Temperature	°C	23	40	60	100
Cure time to reach LSS > 1N/mm ²	hours	4.5			
	minutes		100	20	< 5
Cure time to reach LSS > 10N/mm ²	hours	6	2		
	minutes			30	10

LSS = Lap shear strength.

Curing requirements

To achieve optimum performance properties an elevated temperature cure or post cure is recommended. This adhesive will solidify to a handleable state but will not fully cure at temperatures below 60°C.

Suggested cure schedules are:

3 hrs at 80°C

1 hr at 130°C

30 mins at 150°C

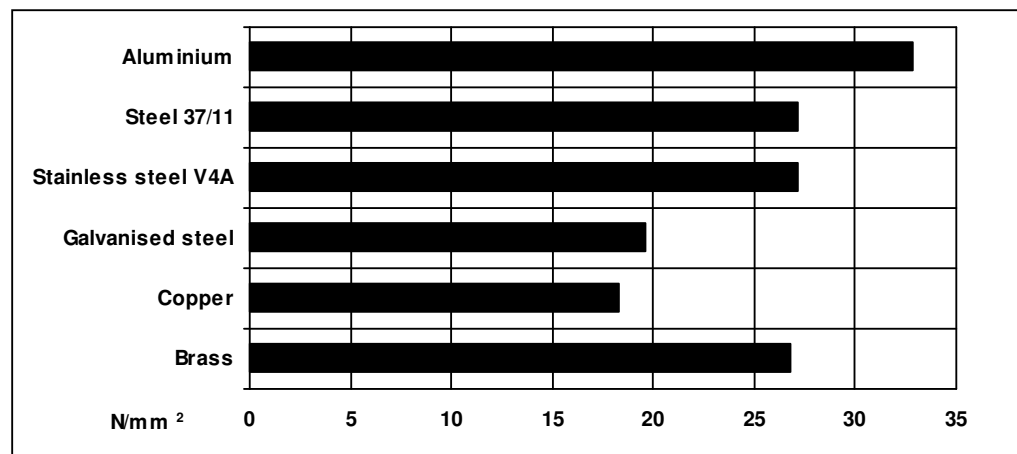
Typical cured properties

Unless otherwise stated, the figures given below were all determined by testing standard specimens made by lap-jointing 114 x 25 x 1.6 mm strips of aluminium alloy. The joint area was 12.5 x 25 mm in each case. The figures were determined with typical production batches using standard testing methods. They are provided solely as technical information and do not constitute a product specification.

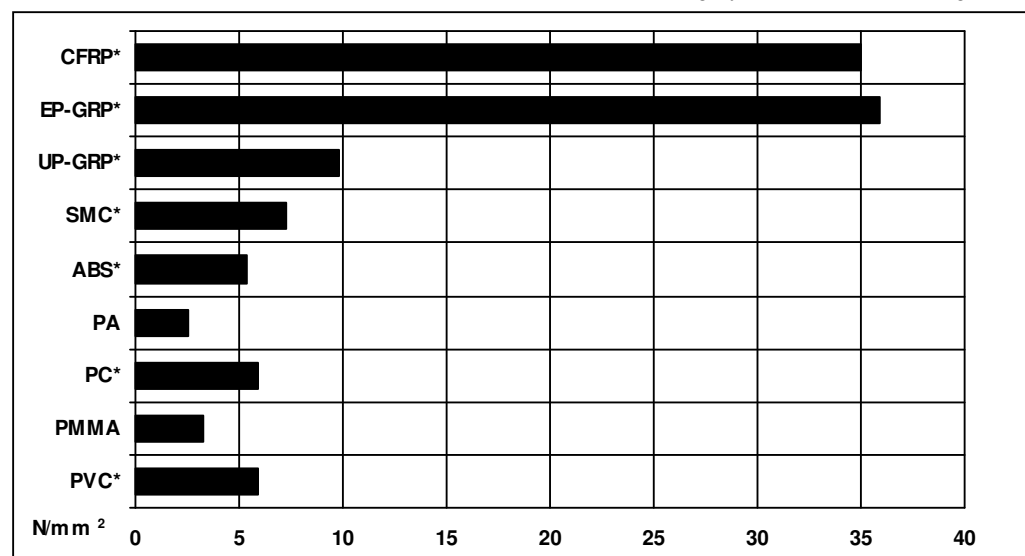
Note: The data in this edition is based on recent retesting of the product.

Average lap shear strengths of typical metal-to-metal joints (ISO 4587)

Cured for 16 hours at 40°C + 1h at 80°C and tested at 23°C Pretreatment - Sandblasting, degreasing

**Average lap shear strengths of typical plastic-to-plastic joints (ISO 4587)**

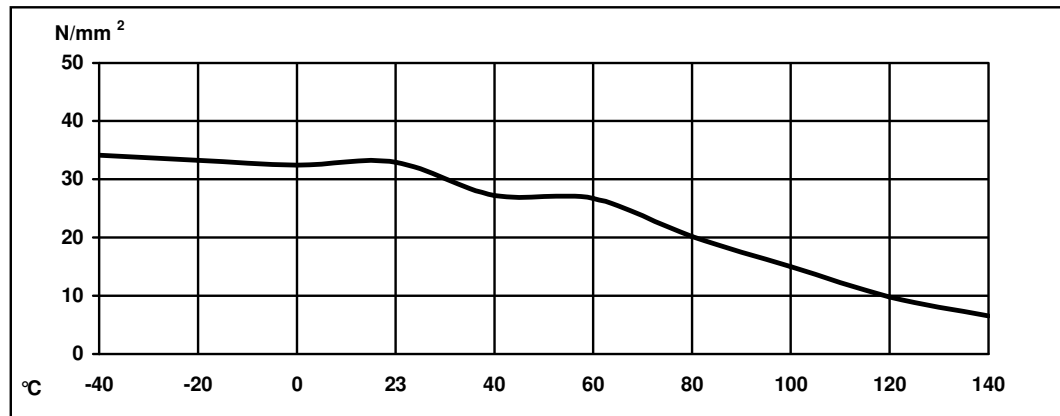
Cured for 16 hours at 40°C+ 1h at 80°C and tested at 23°C. Pretreatment - Lightly abraded and alcohol degreased.



* : substrate failure or substrate delamination

Lap shear strength versus temperature (ISO 4587) (typical average values)

Cure: 16 hours at 40°C +1 hr at 80°C, aluminium, sandblasted and degreased

**Glass transition temperature (ISO 6721 DMA measurement)**

Cure: 16 hours at 40°C +1 h at 80°C

95°C

Glass transition temperature (DSC measurement)

2 hours at 70°C	86°C
1 hour at 80°C	91°C
24 hours at RT + 2 hours at 150°C	122°C

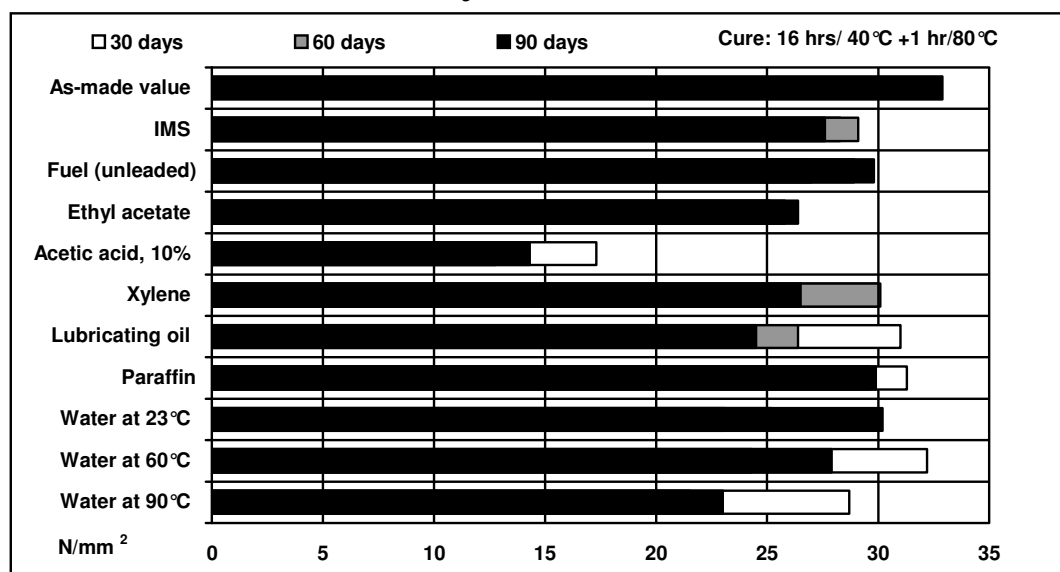
Roller peel test (ISO 4578)

Cured: 16 hours at 40°C

6 - 8 N/mm

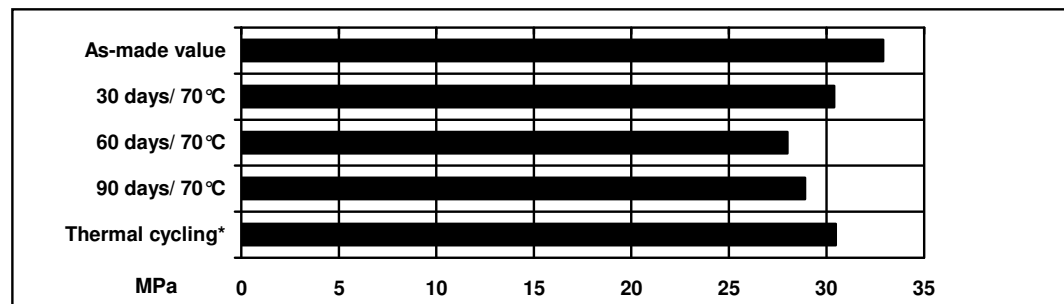
Lap shear strength versus immersion in various media (typical average values) (ISO 4587)

Unless otherwise stated, L.S.S. was determined after immersion for 30,60 and 90 days at 23°C. Cure: 16 hours at 40°C +1 h at 80°C, aluminium, sandblasted and degreased



Lap shear strength versus heat ageing (ISO 4587)

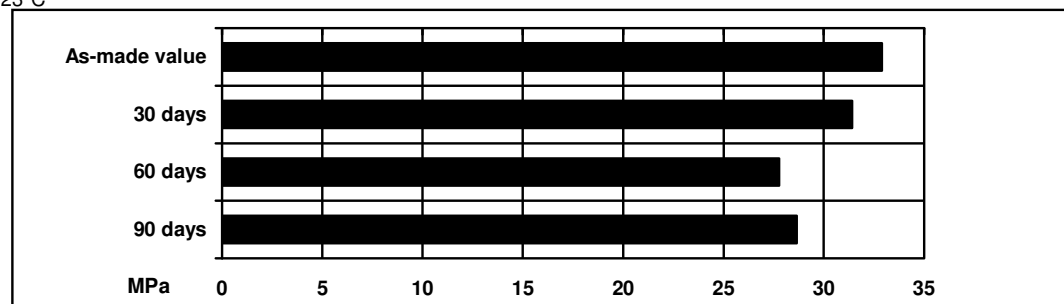
Cure: 16 hrs/ 40°C + 1hr/ 80°C, on aluminium sandblasted and degreased, tested at 23°C



*25 cycles -30°C to + 70°C

Lap shear strength versus tropical weathering (ISO 4587)

(40/92, DIN 50015; typical average values) Cure: 16 hours at 40°C, on aluminium sandblasted and degreased, tested at 23°C

**Tensile strength at 23°C (ISO 527)**

40 MPa

E-modulus

1600 MPa

Elongation at break

4.3 %

Flexural strength at 23°C (ISO178)

65 MPa

Flexural modulus

1500 MPa

Shore Hardness (D scale) (ISO 868/03)

Cure 16 hours/ 40°C + 1hr at 80°C , tested at 23°C, 50%RH

75 D

Bend notch test (ISO 13586) at 23 °C

Cure 16 hours/ 40°C + 1hr at 80°C

 $K_{1c} = 1.7 \text{ MPa.m}^{1/2}$ $G_{1c} = 1.9 \text{ kJ.m}^{-2}$ **Shear modulus G'(ISO 6721)**

Cure: 16 hours/ 40° + 1hr at 80°C

-40°C - 1.3 GPa

0°C - 920 MPa

23°C - 800 MPa

60°C - 490 MPa

90°C - 60 MPa

140°C - 1.2 MPa

Storage	ARALDITE® AW4859 and Hardener HW4859 may be stored for up to 3 years at room temperature provided the components are stored in sealed containers. The expiry date is indicated on the label.
----------------	--

Handling precautions	Caution Our products are generally quite harmless to handle provided that certain precautions normally taken when handling chemicals are observed. The uncured materials must not, for instance, be allowed to come into contact with foodstuffs or food utensils, and measures should be taken to prevent the uncured materials from coming in contact with the skin, since people with particularly sensitive skin may be affected. The wearing of impervious rubber or plastic gloves will normally be necessary; likewise the use of eye protection. The skin should be thoroughly cleansed at the end of each working period by washing with soap and warm water. The use of solvents is to be avoided. Disposable paper - not cloth towels - should be used to dry the skin. Adequate ventilation of the working area is recommended. These precautions are described in greater detail in the Material Safety Data sheets for the individual products and should be referred to for fuller information.
-----------------------------	--

Huntsman Advanced Materials	All recommendations for the use of our products, whether given by us in writing, verbally, or to be implied from the results of tests carried out by us, are based on the current state of our knowledge. Notwithstanding any such recommendations the Buyer shall remain responsible for satisfying himself that the products as supplied by us are suitable for his intended process or purpose. Since we cannot control the application, use or processing of the products, we cannot accept responsibility therefor. The Buyer shall ensure that the intended use of the products will not infringe any third party's intellectual property rights. We warrant that our products are free from defects in accordance with and subject to our general conditions of supply.
------------------------------------	--

Huntsman Advanced Materials warrants only that its products meet the specifications agreed with the buyer. Typical properties, where stated, are to be considered as representative of current production and should not be treated as specifications.

The manufacture of materials is the subject of granted patents and patent applications; freedom to operate patented processes is not implied by this publication.

While all the information and recommendations in this publication are, to the best of our knowledge, information and belief, accurate at the date of publication, NOTHING HEREIN IS TO BE CONSTRUED AS A WARRANTY, EXPRESS OR OTHERWISE.

IN ALL CASES, IT IS THE RESPONSIBILITY OF THE USER TO DETERMINE THE APPLICABILITY OF SUCH INFORMATION AND RECOMMENDATIONS AND THE SUITABILITY OF ANY PRODUCT FOR ITS OWN PARTICULAR PURPOSE.

The behaviour of the products referred to in this publication in manufacturing processes and their suitability in any given end-use environment are dependent upon various conditions such as chemical compatibility, temperature, and other variables, which are not known to Huntsman Advanced Materials. It is the responsibility of the user to evaluate the manufacturing circumstances and the final product under actual end-use requirements and to adequately advise and warn purchasers and users thereof.

Products may be toxic and require special precautions in handling. The user should obtain Safety Data Sheets from Huntsman Advanced Materials containing detailed information on toxicity, together with proper shipping, handling and storage procedures, and should comply with all applicable safety and environmental standards.

Hazards, toxicity and behaviour of the products may differ when used with other materials and are dependent on manufacturing circumstances or other processes. Such hazards, toxicity and behaviour should be determined by the user and made known to handlers, processors and end users.

Except where explicitly agreed otherwise, the sale of products referred to in this publication is subject to the general terms and conditions of sale of Huntsman Advanced Materials LLC or of its affiliated companies including without limitation, Huntsman Advanced Materials (Europe) BVBA, Huntsman Advanced Materials Americas Inc., and Huntsman Advanced Materials (Hong Kong) Ltd.

Huntsman Advanced Materials is an international business unit of Huntsman Corporation. Huntsman Advanced Materials trades through Huntsman affiliated companies in different countries including but not limited to Huntsman Advanced Materials LLC in the USA and Huntsman Advanced Materials (Europe) BVBA in Europe.

Araldite is a registered trademark of Huntsman Corporation or an affiliate thereof.

Copyright © 2008 Huntsman Corporation or an affiliate thereof. All rights reserved.



QUANTUM^X

MX1615B

Strain gauge bridge amplifier

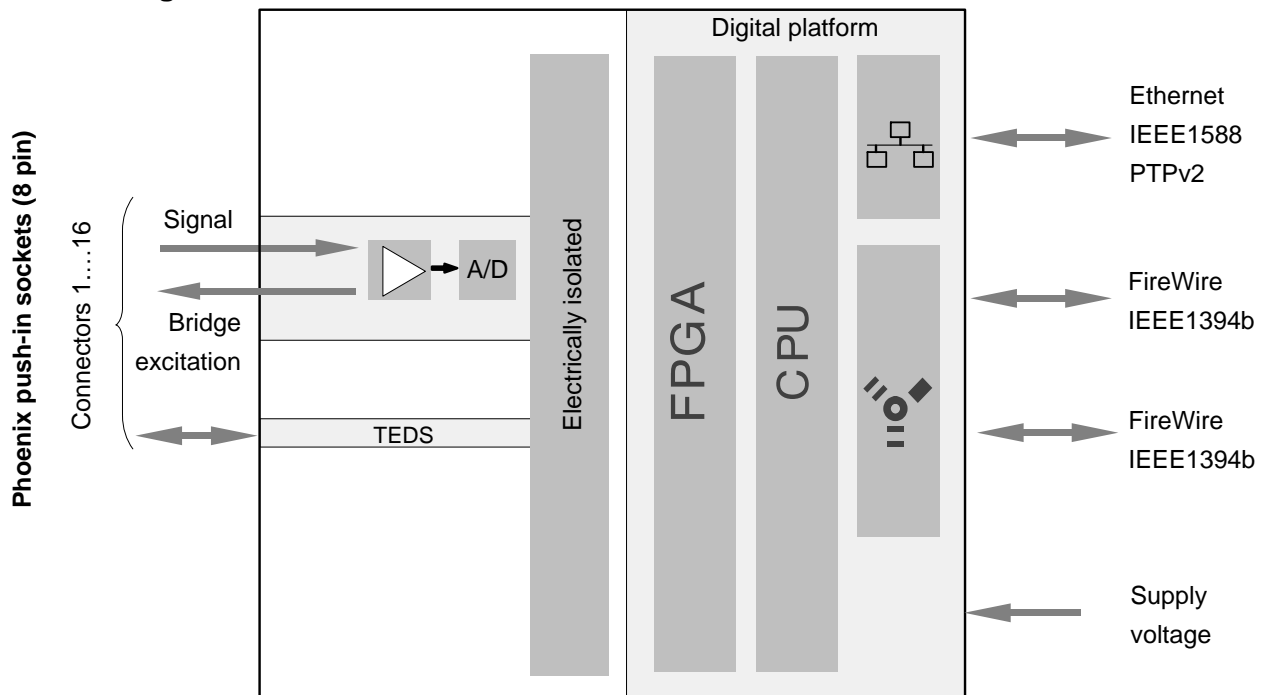
Data sheet



Special features

- 16 individually configurable inputs
- Connection of strain gauges in full-, half-, or quarter-bridge (120 or 350 Ohm)
- Bridge excitation : DC or carrier frequency
- Internal shunt resistor
- Connection of standard voltage, PT100, resistor, Potentiometer
- Individual data rates up to 20 kS/s per channel, active low pass filter
- 24-bit A/D converter per channel for synchronous, parallel measurements

Block diagram



FOIL series F STRAIN GAUGES



Suffix code for temperature compensation materials

-11: Mild steel -17: Stainless steel -23: Aluminium

For ordering, the above suffix code should be added to the basic gauge type.

-196°C Operating temperature range +150°C

Temperature compensation range

+10°C +100°C

Applicable adhesives

CN	-196 ~ +120°C
P-2	-30 ~ +150°C
EB-2	-60 ~ +150°C

GENERAL USE

Gauge pattern	Basic type	Gauge size L W	Backing L W	Resistance Ω
Strain gauges compliant to RoHS2 Directive 2011/65/EU are added to the lineup in F series. They are supplied with CE marking as standard specification. Our logo GOBLET, which is an abbreviation of "Gauges Of Brilliant Lifespan and Environmental Thoughtful", is marked on the package of these gauges.				
Single element				
	FLAB-02	0.2 1.4	3.5 2.5	120
	FLAB-1	1 1.1	6 2.5	120
	FLAB-03	0.3 1.4	3 2	120
	FLAB-05	0.5 1.2	4.3 2.2	120
	FLAB-1	1 1.3	5 2.5	120
	FLAB-2	2 1.5	6.5 3	120
	FLAB-3	3 1.7	7.7 3.5	120
	FLAB-3-60	3 1.2	7.7 3	60
	FLAB-5	5 1.5	10 3	120
	FLAB-6	6 2.2	11 4.3	120
	FLAB-10	10 2.5	15.4 5	120
	FLAB-30	30 2	35 5	120
FLK pattern with narrow gauge width	FLKB-1	1 0.7	4.5 1.4	120
	FLKB-2	2 0.9	5.5 1.5	120
	FLKB-6	6 1	11 2.2	120
	FLKB-10	10 1.6	15 3.8	120
350Ω Single element				
Gauge resistance 350Ω	FLAB-1-350	1 1.6	4.5 3	350
	FLAB-2-350	2 1.9	6 3.5	350
	FLAB-3-350	3 1.6	7.2 3	350
	FLAB-5-350	5 1.8	9.4 3.8	350
	FLAB-6-350	6 2.6	10.8 4.5	350
	FLAB-10-350	10 3	16 5	350
	FLAB-6-1000	6 4.6	11 7	1000
Each package contains 10 gauges.				

GE 8 C

Lubricant

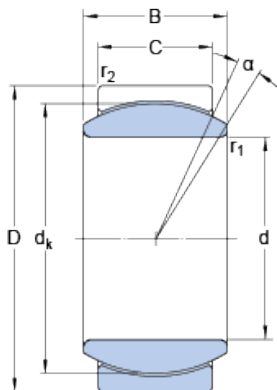
Maintenance free – dry
lubrication

Design (sliding contact surface combination)

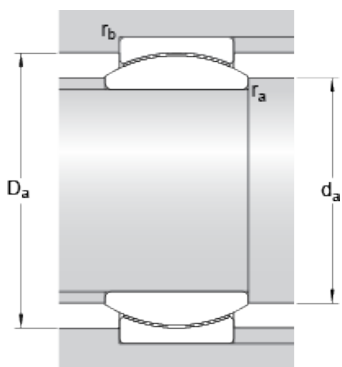
Steel/PTFE sintered
bronze

Sealing solution

-

Dimensions

d	8	mm
D	16	mm
B	8	mm
C	5	mm
α	15	°
d _k	13	mm
r ₁	min. 0.3	mm
r ₂	min. 0.3	mm

Abutment dimensions

d _a	min.	9.4	mm
d _a	max.	10.2	mm
D _a	min.	12.3	mm
D _a	max.	14.6	mm
r _a	max.	0.3	mm
r _b	max.	0.3	mm

Calculation data

Basic dynamic load rating	C	5.85	kN
Basic static load rating	C ₀	14.6	kN
Specific dynamic load factor	K	100	N/mm ²
Specific static load factor	K ₀	250	N/mm ²
Material constant	K _M	1400	

Mass

Mass plain bearing	0.008	kg
--------------------	-------	----

CHARGES - COUPLES

LOADS - TORQUES

Références de base Basic Part number		Charges statiques limites Limit static loads		Charges dynamiques radiales Radial dynamic loads C25	Couples de rotation Rotational torques	
		Radiales Radial Cs	Axiales Axial Ca**		standard normal EN2584	réduits reduced EN4038
Sans gorge without groove	Avec gorges with grooves	kN		N.m		
XRE 5	XRE 5 R	20,5	1,9	12,3	0,08 à 0,5	0,005 à 0,06
XRE 6	XRE 6 R	29,2	3,5	17,5	0,08 à 0,5	0,005 à 0,06
XRE 8	XRE 8 R	37	3,9	22,2	0,08 à 0,5	0,005 à 0,06
XRE 10	XRE 10 R	47,2	6,5	28,3	0,12 à 0,8	0,008 à 0,1
XRE 12	XRE 12 R	78,1	11,7	43	0,12 à 0,8	0,008 à 0,1
XRE 15	XRE 15 R	121,9	18	67	0,12 à 0,8	0,008 à 0,1
XRE 17	XRE 17 R	148,3	24,3	81	0,12 à 0,8	0,008 à 0,1
XRE 22	XRE 22 R	268,6	45,5	147,7	0,25 à 1	0,015 à 0,25
XRE 25	XRE 25 R	324,7	55,9	162,4	0,25 à 1	0,015 à 0,25
XRE 30	XRE 30 R	433,4	77,8	216,7	0,4 à 2	0,02 à 0,4
XRE 35	XRE 35 R	543,4	92,2	271,7	0,4 à 2	0,02 à 0,4
XRE 40	XRE 40 R	680,9	113,4	340,3	0,6 à 2,7	0,03 à 0,6
XRE 45	XRE 45 R	833,9	135,9	416,9	0,6 à 2,7	0,03 à 0,6
XRE 50	XRE 50 R	981,4	154,2	490,7	0,6 à 2,7	0,03 à 0,6

** Ces valeurs peuvent être limitées par la charge de dessertissage (consulter notre service technique)
These values can be limited by the de-crimping load (please contact our technical department)

OPTIONS - DESIGNATIONS

ZXRE 17ARXTTCP6

Sans code : version standard non chromée, CP6 : sphère bague intérieure chromée	No code : standard version non plated ball CP6 : chrome plated ball diameter
Sans code : version standard TT = version avec joints d'étanchéité PP = version avec flasques de protection } page a22	No code : standard version TT = sealed version PP = shielded version } page a22
Sans code : couple de rotation standard X = couple de rotation réduit	No code : standard rotational torque X = reduced rotational torque
Sans code : sans gorge de sertissage R = avec gorges de sertissage	No code : chamfered outer race R = grooved outer race
Sans code : sans SARFLON dans alésage A = SARFLON dans alésage - page a23	No code : bore without SARFLON A = SARFLON lined bore - page a23
Dimension de l'alésage en mm	Bore dimension in mm
Référence de base	Basic part number
Sans code : diamètre extérieur non cadmié Z = diamètre extérieur cadmié	No code : non plated external diameter Z = cadmium plated external diameter

*** INFORMATION AECMA**

Les normes AECMA EN2064 et EN2023 sont déclassées et remplacées respectivement par EN2755 et EN2584

*** AECMA INFORMATION**

AECMA standards EN2064 and EN2023 are inactive and respectively replaced by EN2755 and EN2584

SPECIFICATION TECHNIQUE

AECMA - EN2755 *

NORMES DE PRODUIT

AECMA EN2585 *

AECMA EN4039

MATIERES

- Autolubrifiant : SARFLON
- Bague intérieure : acier résistant à la corrosion 440 C
- Bague extérieure : acier résistant à la corrosion 17.4 PH



TECHNICAL SPECIFICATION

AECMA - EN2755 *

PRODUCT STANDARD

AECMA EN2585 *

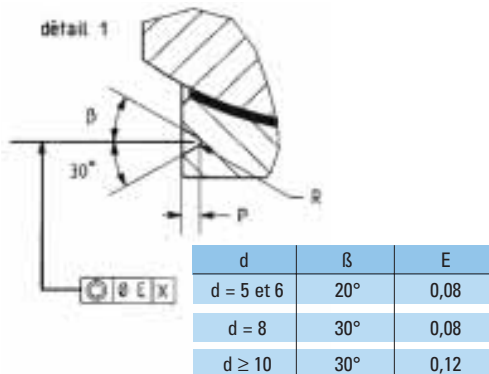
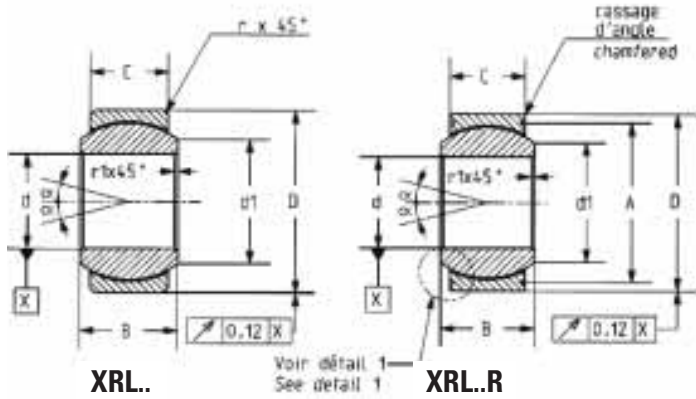
AECMA EN4039

MATERIALS

- Liner : SARFLON
- Inner ring : corrosion resistant steel 440 C
- Outer ring : corrosion resistant steel 17.4 PH

DIMENSIONS - TOLERANCES

Références de base Basic Part number	d	D	C ± 0,1	B 0 - 0,06	Tolérances Tolerances		d1 ≈	r	r1	A + 0,1 0	P 0 - 0,2	R + 0,1 0	α	Masse Weight	
					△ dmp	△ Dmp									
Sans gorge without groove	Avec gorges with grooves	mm				μm = 0,001 mm		mm							
														g	
XRL 5	XRL 5 R	5	16	8,5	11	0 - 8	0 - 8	7,7	0,5/0,8	0,1/0,4	14,2	0,7	0,2	15°	16
XRL 6	XRL 6 R	6	16	8,5	11	0 - 8	0 - 8	7,7	0,5/0,8	0,1/0,4	14,2	0,7	0,2	15°	16
XRL 8	XRL 8 R	8	18	8	11	0 - 8	0 - 8	10,3	0,5/0,8	0,1/0,4	16,2	0,7	0,2	14°	17
XRL 10	XRL 10 R	10	21	10	12,5	0 - 8	0 - 9	12,2	0,5/0,8	0,1/0,4	18,4	0,9	0,3	10°	27
XRL 12	XRL 12 R	12	26	13	16	0 - 8	0 - 9	15,5	0,5/0,8	0,1/0,4	23,4	0,9	0,3	10°	49
XRL 15	XRL 15 R	15	29	13,5	17	0 - 8	0 - 9	18,9	0,5/0,8	0,1/0,4	26,4	0,9	0,3	9°	62
XRL 17	XRL 17 R	17	30	14,5	18	0 - 8	0 - 9	20,1	0,5/0,8	0,1/0,4	27,4	0,9	0,3	9°	69
XRL 20	XRL 20 R	20	35	16	20	0 - 10	0 - 11	23,5	0,5/0,8	0,1/0,4	31,8	1,4	0,3	8°	104
XRL 25	XRL 25 R	25	54	26	32	0 - 10	0 - 13	35,3	0,6/1	0,1/0,4	50,8	1,4	0,3	9°	445
XRL 30	XRL 30 R	30	60	28	34	0 - 10	0 - 13	40,9	0,8/1,2	0,1/0,4	56,8	1,4	0,3	8°	480
XRL 35	XRL 35 R	35	65	29	36	0 - 12	0 - 13	45,5	0,8/1,2	0,1/0,4	61,8	1,4	0,3	8°	565
XRL 40	XRL 40 R	40	68	31	38	0 - 12	0 - 13	47	0,8/1,2	0,1/0,4	64,8	1,4	0,3	8°	600
XRL 45	XRL 45 R	45	76	33	41	0 - 12	0 - 13	54,1	0,8/1,2	0,1/0,4	72,8	1,4	0,3	8°	800
XRL 50	XRL 50 R	50	82	35	44	0 - 12	0 - 15	60,3	0,8/1,2	0,1/0,4	78,8	1,4	0,3	8°	970
XRL 55	XRL 55 R	55	96	40	52	0 - 12	0 - 15	63,4	0,8/1,2	0,1/0,4	92,8	1,5	0,3	10°	1580
XRL 60	XRL 60 R	60	105	48	60	0 - 12	0 - 15	69,7	0,8/1,2	0,1/0,4	101,8	1,5	0,3	9°	2250



D Project Thesis

Validation of Finite Element Analysis using strain gauges, of the suspension system of a Formula student car

PROJECT REPORT

NORWEGIAN UNIVERSITY OF SCIENCE AND TECHNOLOGY

June 12, 2019

Kristoffer Haugland

Supervisor: Jan Torgersen



**Department of Mechanical
and Industrial Engineering**

Project Description

The suspension system designs within Revolve NTNU have proven to be part of making Revolve NTNU achieve great merits in the renowned student engineering competition, Formula Student. Finite element analysis has been employed since the start of Revolve. The complexity and knowledge of these simulations have also increased a great deal within the organization. Through the 2018 season it became apparent that Revolve NTNU was at a stage where more knowledge is needed to make better decisions in terms of dimensioning of structural parts.

In this specialization project an experiment has been conducted and compared to FEA performed by the 2018 team. Results vary in correlation, and a conclusion is drawn that further work needs to be done in terms of correlating theoretical and experimental data.

Preface

I would like to give thanks to the Revolve NTNU team 2018 for letting me be a part of such a great project for two years. A special thanks goes to Hermann Sundklakk and Sindre Moklebost, for helping me with data aquisition during the testing phase in this project. Thanks to Fredrik Capellen for the good discussions on how to solve the task at hand.

Contents

List of Figures	vii
List of Tables	viii
Abbreviations	ix
1 Introduction	1
1.1 Formula Student	1
1.2 Revolve NTNU	1
1.3 Goals and Limitations	2
2 Theory and Background	3
2.1 Racing	3
2.2 Suspension system	4
2.2.1 Camber Angle	5
2.2.2 Toe Angle	5
2.3 Compliance and its effects	6
2.4 Load paths	8
2.5 Comparing Finite Element Analysis to Experimental Data	9
2.5.1 Strain Gauges	9
2.5.2 Strain Gauge Types	11
3 Approach	12
3.1 Quasi Static Test jig	12
3.1.1 Actuator	12
3.1.2 Test set up	14
3.2 Physical Testing and Data Acquisition	15
3.3 Statistics	16
3.4 Data Extraction	17
3.4.1 Strain Gauge Modelling and Data extraction	17
3.4.2 Strain Gauge Placement	19
4 Results	21
4.1 X-Direction - 1000 N	21
4.2 Y-Direction - 2000 N	22

4.3 Z-Direction - 2000 N	23
5 Discussion	24
5.1 Main Findings	24
5.2 FEA	24
5.2.1 Suspension rod model	24
5.3 Bellcrank model	25
5.4 Uncertainties in the experiment	25
6 Conclusion and Further Work	27
Appendix	30
A Finite Element Models	30
A.1 Strain Gauge Simplified Model	31
A.1.1 Parts	31
A.1.2 Part Properties	32
A.1.3 Assembly and Steps	33
A.1.4 Interactions and Contact	33
A.1.5 Loads and Boundary Conditions	34
A.1.6 Mesh	36
A.1.7 Results	37
A.2 Bellcrank Model	38
A.2.1 Parts	38
A.2.2 Part Properties	39
A.2.3 Assembly and Steps	40
A.2.4 Interactions and Contact	41
A.2.5 Connectors	41
A.2.6 Loads and Boundary Conditions	42
A.2.7 Mesh	42
A.3 Suspension Rod Model	43
A.3.1 Parts	43
A.3.2 Part Properties	44
A.3.3 Assembly and Steps	46
A.3.4 Interactions and Contact	47
A.3.5 Loads and Boundary Conditions	48

A.3.6	Mesh	48
B	Formula Student Events	49
C	Load Case 2018	50

List of Figures

1.1	The 2018 car, Atmos, during Formula student Germany	1
2.1	G-G Diagram, with lateral acceleration on the horizontal axis and longitudinal acceleration on the vertical axis	3
2.2	Tire Axis System	4
2.3	Suspension system front left	4
2.4	Suspension nomenclature and tire axis system	4
2.5	Camber and toe angle [4]	6
2.6	Rear toe compliance in FS-car [7]	7
2.7	Example of Z-direction force propagated through suspension system	8
2.8	Wheatstone bridge circuit [10]	10
2.9	Strain Gauge Rosette [11]	11
3.1	Actuator	12
3.2	Actuator assembled and mounted to car	13
3.3	Quasi Static Test Jig in bot x- and y-direction	14
3.4	HBM Quantum MX1615 data aquisition module	15
3.5	Raw Force data	16
3.6	Bellcrank strain data, Fz load	17
3.7	Bellcrank strain data, Fx load	17
3.8	Coordinate system x-axis aligned with strain direction	17
3.9	Location of each strain gauge	19
3.10	Strain Gauge placement on bellcrank and Angle lock	20
5.1	Left Mean strain: $693 \frac{\mu m}{m}$ Right Mean strain: $883 \frac{\mu m}{m}$	25
A.1	Strain gauge simplified model parts	31
A.2	Block Material	32
A.3	Strain gauge material properties	32
A.4	Strain gauges assembled to the block	33
A.5	Tie Constraint on surface	33
A.6	Kinematic coupling	34
A.7	Load application	35
A.8	Short side Boundary condition on Block	35
A.9	Mesh	36
A.10	Results from FEA showing $2.391e^{-05}$ to $2.392e^{-05}$	37
A.11	Bellcrank Parts	38

A.12 Materials Bellcrank Analysis	39
A.16 Mesh overview	42
A.20 Steps	46
A.22 Load application in Z-direction	48
A.23 Rod Model Mesh overview	48
C.1 Load cases 2018	50

List of Tables

4.1	Strain Data lower angle lock 1000 N X-direction	21
4.2	Strain data lower angle lock 2000 N Y-direction	22
4.3	Strain data lower angle lock 2000 N Z-direction	23

Abbreviations

CAD	Computer Aided Design
CG	Centre of gravity
DAQ	Data Acquisition
DOF	Degree of freedom
FE	Finite Element
FEA	Finite Element Analysis
FS	Formula Student
FSG	Formula Student Germany
FSS	Formula Student Spain
FSUK	Formula Student United Kingdom
FUA	Front Upper Aft
ODB	Output Data Base
QS	Quasi Static
QST	Quasi Static Testing
SAE	Soceiety Of Automotive Engineers
SG	Strain Gauge

1 Introduction

1.1 Formula Student

Formula student (FS) is the name of the worlds largest student engineering competition. The competition and its format was started in 1981 by the Society of Automotive Engineers (SAE), in the United States of America [1]. Students compete in teams representing their universities. Teams range in size, from twenty to 100+ members. During one season there are multiple FS-competitions, with the most predominant ones being Formula Student Germany (FSG) and Formula Student UK (FSUK). The competition awards the teams with best overall scores. Scores are gathered through dynamic and static events. Where the static events are least counting. There are in total four types of dynamic events, and three static events. For details see Appendix B. In the past five years, electrical cars have become more and more dominant. This is also the class of car Revolve NTNU designs. The competition is regarded as one of the biggest proving grounds for young engineers wanting to play a role in the automotive industry.

1.2 Revolve NTNU

Revolve NTNU was founded in 2010 by four students who wanted to apply their theoretical knowledge to something practical. The organization had their first car on the start grid at FSUK, in 2013. The organization has since then grown into something which is reminiscent to a medium sized business. With a member count of 70 in the 2018 season. The 2018 season was the most successful season in Revolve NTNUs history, with a second place at FSG and a fourth place at Formula Student Spain (FSS).



Figure 1.1: The 2018 car, Atmos, during Formula student Germany

1.3 Goals and Limitations

The suspension system used since the start of Revolve NTNU, has been a double A-arm suspension system. Since 2016, and continuing into the 2019 season a push rod actuated system has been employed. The structural design of the suspension system has been conducted through load case estimation by the vehicle dynamics engineer. The load cases have been made to accommodate different worst case situations the vehicle might experience. The load cases are passed on from the vehicle dynamics department, and given to the engineers responsible for their systems (rims, steering rack etc.). The loads are then used in finite element analysis (FEA) done by each person.

Since the start of the organization, a hard question to answer has been: "How stiff is stiff enough?". Stiffness is a sought after characteristic in motor sport, as lack thereof can be a major troublemaker when it comes to vehicle handling and control. An increase in stiffness is often closely related to an increase in weight. An increase in weight is a direct performance parameter. A higher weight will require an increase in force to accelerate the vehicle. To answer the question stated, a foundation must be laid. This thesis will act as a starting point for the work in answering this question.

An effort has been made into investigating how accurate FEA from the 2018 season was. This is done through an experiment of quasi static load application on the 2018 car, Atmos. The front left suspension of the car has been analyzed. Two finite element models were used when comparing simulation to testing. The thesis will also give an insight in what way the vehicle is affected by loading, and the implications this has for vehicle handling.

The main goal of this thesis is:

- Gain knowledge on correlating experimental data to finite element analysis.
- Compare finite element models made in 2018, to the suspension assembly of the 2018 car through quasi static testing.

2 Theory and Background

2.1 Racing

Driving a car as fast as possible around a given track has a history dating back to when the first automobile was created. Milliken et. al [2] summarizes the following: "*The overall technical objective in racing is the achievement of a vehicle configuration, acceptable within the practical interpretation of the rules, which can traverse a given course in a minimum time (or at the highest average speed) when operated manually by a driver utilizing techniques within his/her capabilities*"

A high average speed is obtained by high change in speed i. e. high acceleration. Into a corner the vehicle should be decelerated as fast as possible before the driver starts to accelerate the vehicle out of the corner and onto the straight, before arriving at the next corner. Straight line acceleration is known as longitudinal acceleration. In a corner, lateral acceleration occurs. The higher the lateral acceleration obtained, the quicker a car can handle through corners. From these two explanations, a race cars performance may be drawn as a the resultant vector represented by the two quantities of longitudinal and lateral acceleration. This leads to the creation of the G-G diagram. The G-G diagram is made up of logged data points of lateral and longitudinal acceleration. Spending time at the boundary of the G-G diagram will result in faster lap times. The race car designers job is to increase this boundary.

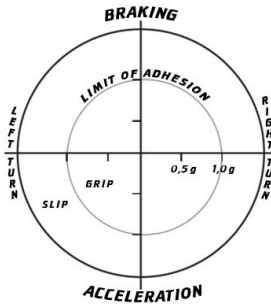


Figure 2.1: G-G Diagram, with lateral acceleration on the horizontal axis and longitudinal acceleration on the vertical axis

2.2 Suspension system

The suspension system is the first system to experience the external forces acting on the vehicle. The suspension constrains each wheel to movement in one direction (Z-direction). This is a simplification, the wheel will move laterally in addition to vertically. How much, is determined by the kinematics of the suspension. The velocity of the movement is controlled through a coilover (fig. 2.2). A damper and spring assembly, situated inboard the chassis. The front wheels are permitted to allow rotation about the steering axis of the wheel, enabling the driver to control the steering of the vehicle. Pure Z-directional forces are often referred to as bump loads. Longitudinal loading is in the X-direction and lateral loads are in the Y-direction. fig. 2.2

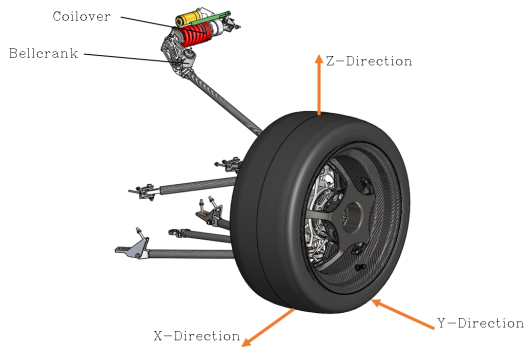


Figure 2.2: Tire Axis System

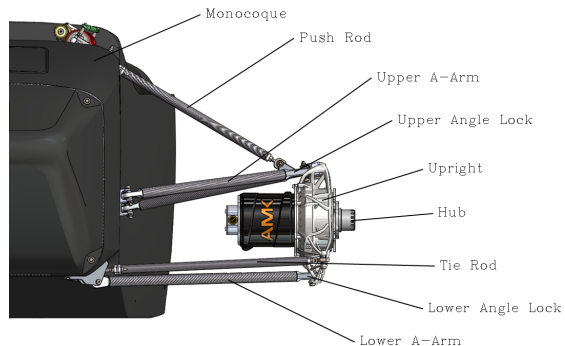


Figure 2.3: Suspension system front left

Figure 2.4: Suspension nomenclature and tire axis system

The main goal of the suspension is controlling movement and speed of the wheels. This is done in a way which will let the tire generate as much force as possible at their contact patch, interacting with the ground. This means controlling the angle the tires have in relation to the ground [3]. The most important in structural work being camber and toe angles.

2.2.1 Camber Angle

The camber angle is defined as the angle, ϕ , between a tilted wheel plane and the vertical. [2] A positive camber is described as the top of the wheel is tilting away from the vehicle, negative vice versa. Camber plays a role in force generation between the tire and the road as the tire will produce a force in the direction it is tilted. As the car goes through a turn the tire is subjected to a lateral force causing lateral tire wall deflection. As the side wall deflects in a negative cambered wheel, the deflection can zero out the negative camber and keep the wheel more perpendicular to the ground. Resulting in a maximization of lateral grip [4]. The opposite will result in a reduction in lateral grip.

2.2.2 Toe Angle

The toe angle is defined as the angle between the tires center plane as the tires are rotated around its center axis [4]. The toe angle is viewed from above, see fig. 2.5. A cambered tire will not follow a straight line as it is free rolled. Two tires angled with the same camber angle will create an equal force opposing each other. This will lead to a heat build up and excessive wear and tear of the tire [2]. An appropriate toe-out angle can negate these effects. Toeing of the rear wheels can be used to introduce under- or oversteer effects. Toe-out leads to oversteer and toe-in creates understeer [4].

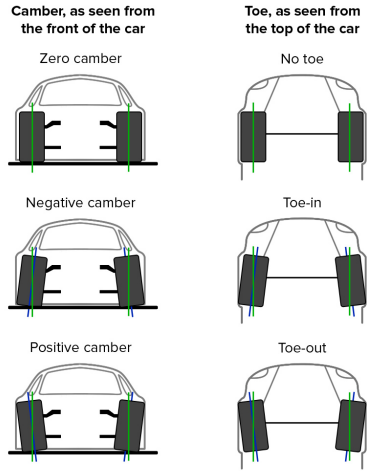


Figure 2.5: Camber and toe angle [4]

2.3 Compliance and its effects

Stiffness is defined as the ability of an elastic object to resist deformation under a given load. [5] Compliance is the inverse of stiffness [2]. As forces are reacted through the suspension, compliant effects occur. The different forces applied at the contact patch will result in deformation of various parts in the suspension system. This deformation accumulates and will alter the angle the tires have in relation to the ground. Different compliant effects are summarized below:

- Toe compliance (steer compliance) - Forces acting on the wheel affect the angle of the wheel relative to the direction of vehicle.
- Camber compliance - Change in camber angle of the wheel as forces act on it

The different compliant effects can lead to *understeer* or *oversteer* in a vehicle. An easy way to think of this effect, is to visualize a car in a turn with fixed velocity and a slightly increasing acceleration. The driver must control the steering angle to keep a constant radius. Compliant understeer will make the vehicle travel along a larger circle [2]. For a driver, compliance can be a major issue in terms of vehicle control, this with special regard to rear toe compliance. Rear toe compliance can not be controlled by the driver. It is hard to quantify how big an influence it will have, but it will lead to oversteer. Oversteer is a more unstable condition for the vehicle and driver control [6].



Figure 2.6: Rear toe compliance in FS-car [7]

2.4 Load paths

Visualizing load propagation through the suspension system helps understand how forces are reacted. As the vehicle is driven around a track, forces are generated at the four contact patches of the tire. The ability of the tires to generate force is an attribute not fully understood, and the theory is not within the scope of this thesis. The tires generate two type of forces, lateral and longitudinal forces[2].

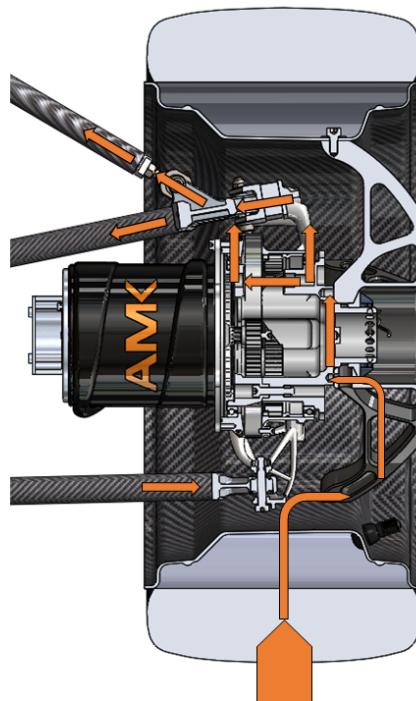


Figure 2.7: Example of Z-direction force propagated through suspension system

The forces from the tires enter the wheel assembly through the rim. First through the rim shell, and then through the rim center. The rim center is connected to the hub and carrier. These two parts not only make up the bearings seats for the wheel bearings, but also act as a frame holding the planetary gear box. Leaving the in-wheel bearings the force path continues through the upright, before entering the suspension rods. Depending on the type of loading, each rods experiences a different magnitude of compression/tensile load.

Lateral and longitudinal forces are reacted through the A-arms and tie rod. The lateral forces will also be reacted through the push rods. The bump forces (forces purely in the Z-direction) will make their way through the push rod and into the coil-over through the bell

crank. The simplification of having forces feed into the system one at a time is not accurate in terms of the actual scenario occurring during driving. All forces act simultaneous in different magnitudes. Lateral and longitudinal forces are also a catalyst for Z-direction forces as load transfer of the vehicle occurs. This happens due to the center of mass of the vehicle being above the wheels center plane, generating a moment as loads are applied at the wheels [3].

2.5 Comparing Finite Element Analysis to Experimental Data

The compliant effects mentioned in the section above can be quantified through FEA. The first step in quantifying these effects is to evaluate the displacement, of the part(s) being analyzed. To know if the displacement in the simulation is accurate, experiments need to be conducted to gain comparative data. This can be done by replicating the finite element model in an experimental setting. Monahang et. al [8] show good correlation when comparing the FEA of a 3D printed medical implant with experimental data.

2.5.1 Strain Gauges

In the paper by Monahang et. al [8] strain gauges are employed to accumulate the necessary data. Strain gauges are devices used to measure strain, by converting an analog signal to an electrical signal. The strain gauge referred to in this thesis is called: "*Bonded Metallic Foil Grid Resistance Strain Gauge*". The strain gauge consists of a metallic strips covered with thin plastic film. The strain gauge is secured to a mechanical part with glue. As the part is deformed (strained), the strain gauge is strained, and the resistance in the metallic foil changes. Measuring this resistance change yields the strain through eq. 1. GF is denoted as the Gauge Factor, ϵ is the strain and $\frac{\Delta R}{R}$ is the change in resistance. [9]

$$GF = \frac{\Delta R/R}{\Delta L/L} = \frac{\Delta R/R}{\epsilon} \quad (1)$$

As the changes in resistance are minuscule, a "Wheatstone Bridge" is employed (fig. 2.8). This is a two legged balancing circuit consisting of 4 resistors, where one resistor is the unknown (R_x). The unknown resistance is the strain gauge. The two legs are balanced with a variable resistance (R_2), and the other leg contains the unknown resistor. The balanced bridge will yield eq. 2.[10]

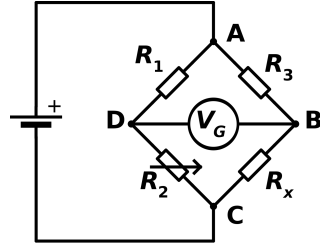


Figure 2.8: Wheatstone bridge circuit [10]

As R_x changes with straining of the component. The change is calculated by substituting eq. 2 into eq. 3, and yielding eq. 4.

$$\frac{V_{out}}{V_{In}} = \frac{R_3}{R_3 + R_x} - \frac{R_2}{R_1 + R_2} \quad (2)$$

$$V_r = \frac{V_{out}}{V_{IN\text{strained}}} - \frac{V_{out}}{V_{IN\text{unstrained}}} \quad (3)$$

$$\frac{\Delta R}{R} = \frac{-4V_r}{1 + 2V_r} \quad (4)$$

By now substituting eq. 4 into the gauge factor, eq. 1 we can obtain a solution for strain based on change in resistance:

$$\epsilon = \frac{-4V_r}{GF(1 + 2V_r)} \quad (5)$$

2.5.2 Strain Gauge Types

Two types of strain gauges have been used in the experiment conducted in this thesis, one axis strain gauge and strain gauge rosette. The one axis strain gauge consist of one single strain gauge, measuring strain in the longitudinal direction of its grid. The strain gauge rosette consists of three strain gauges in 0° , 45° and 90° . [11].

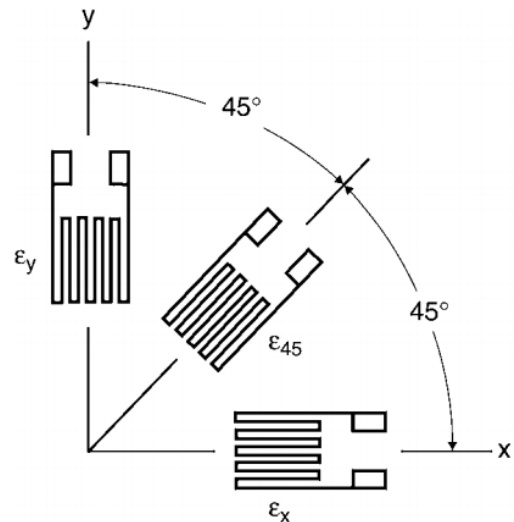


Figure 2.9: Strain Gauge Rosette [11]

3 Approach

3.1 Quasi Static Test jig

To apply loads to the suspension, a test jig was built. The jig applies a displacement load to the suspension, and measures the reaction forces i.e the forces acting on the suspension. The test jig consists of a front brace, a rear braces and an actuator. The front and rear brace are steel trusses. These were secured to the floor, and at each end of the vehicle. The rear brace was secured to the floor of the monocoque, and the front brace was secured to the front of the monocoque.

3.1.1 Actuator

The actuator was made to apply forces in two directions at a time. Depending on how the actuator is secured to the car, it can apply a x- or y-directional displacement. Z-direction can be applied either way. The actuator has two force transducers in the load path. Load application in the x/y - direction is done my turning the black handle seen in fig: 3.1. The actuator seen at the bottom of the figure, applies a displacement in the Z-direction. The distance from the hub center to the force application point is the same as the continental tires used by Revolve.

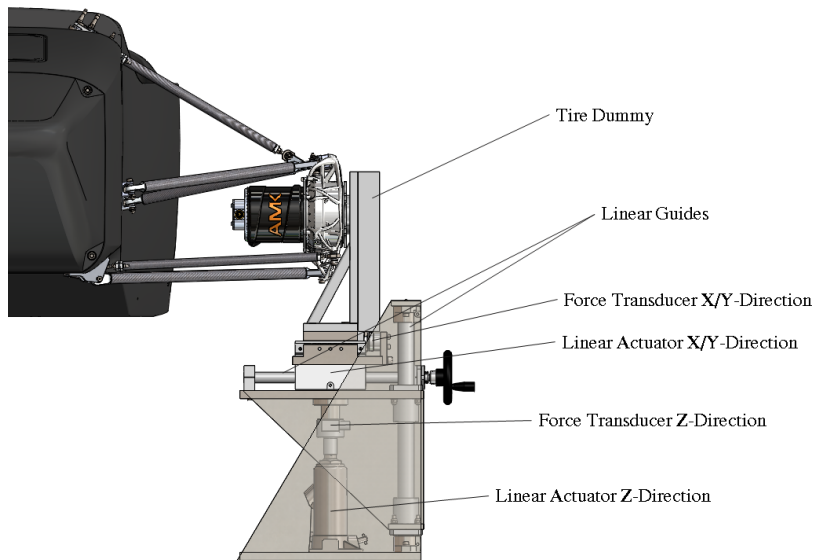


Figure 3.1: Actuator

The main frame of the actuator is made up of ten millimeter steel plates. Linear guides constrain motion in two directions. Motion is dependent on what linear actuator is operated. The actuator is made to operate at a load of 2000 N. This criterion was set based on the being close to the load cases from the 2018 season (Appendix C), but still making the jig as nimble as possible.

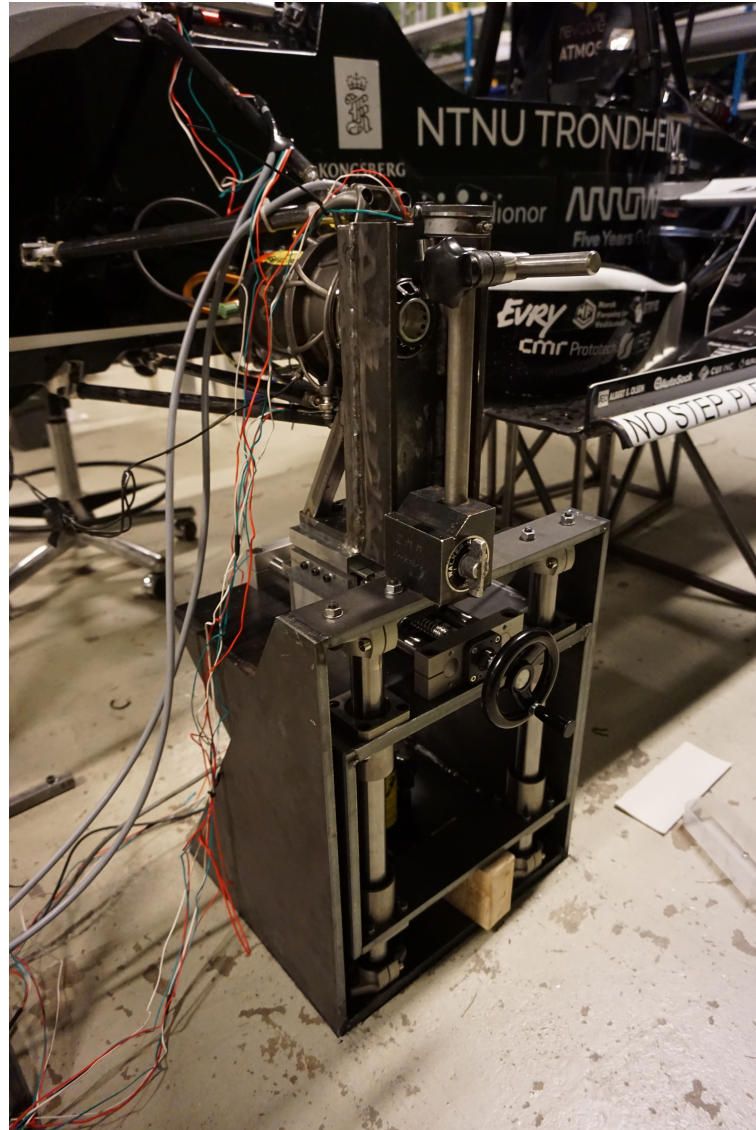


Figure 3.2: Actuator assembled and mounted to car

3. APPROACH

3.1.2 Test set up

The front and rear braces were welded together after being cut to the correct length. The car was then positioned onto the braces. When the assembly was in the correct position, all holes for securing the braces to the floor were marked and drilled. The actuator was also bolted to the floor. The position of the actuator was found by fastening the tire dummy plate onto the hub and ensuring a zero steering angle. The actuator was then moved into place so that the linear guides underneath the tire dummy aligned. It was ensured that the position was in the center of the Z-actuator, so forces applied had the correct line of action. The tire dummy was then secured to the linear guide. When the actuator was in the correct place all holes for bolting the actuator to the ground were marked and drilled. It must also be made notice of that a dummy coilover was used while testing.

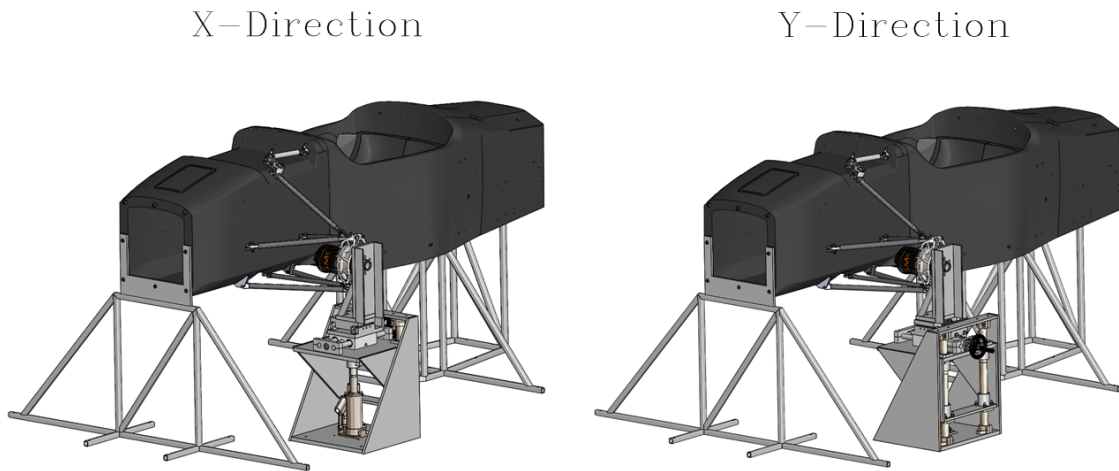


Figure 3.3: Quasi Static Test Jig in both x- and y-direction

3.2 Physical Testing and Data Acquisition

Testing was, as mentioned earlier, limited to the front left suspension of the car. Loads were applied in sets from 500 N up to 2000 N, with 500 N intervals. It was also chosen to apply load and release load application multiple times at each load level. This was done to ensure that the measurements were consistent within each load level. In the x-direction, the maximum load set applied was a 1000 N. Two persons preformed the testing. One person operated the data acquisition module, and one person applied the actuator. Loads were applied in one direction at a time. The person responsible for the data acquisition reported how long the load was being applied, and if the correct load was being reached. The data acquisition (DAQ) module used, was an HBM Quantum MX1615 (fig. 3.4) with 16 HBM phoenix connectors connected to TML FRAB 5-11 strain rosette strain gauges and HBM 1-LY11-6/120A one axis gauges. All gauges were set to operate in a full bridge configuration with a sampling frequency of 300Hz. No strain gauge was used for temperature compensation. This was a decision made based on the room temperature non fluctuating, and the short periods load application lasted. All gauges were also zeroed before each test set.

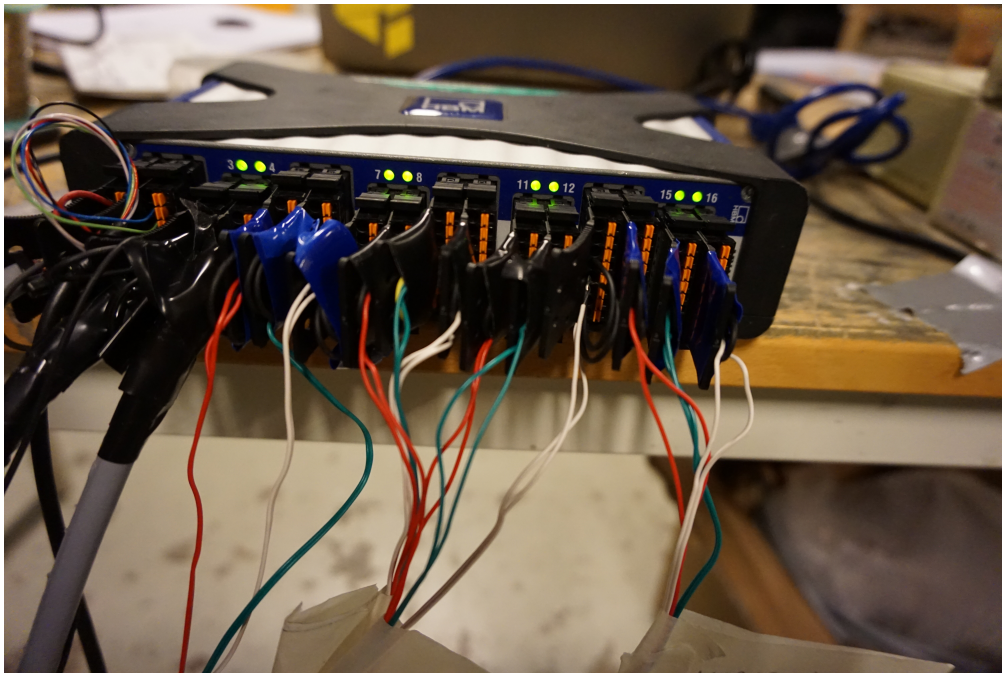


Figure 3.4: HBM Quantum MX1615 data aquisition module

3.3 Statistics

The data was recorded automatically in a Matlab friendly format (.TSX), through the "HBM Catman" software. A time vector was generated by extracting time stamps relating to the load level being applied. This was done from the raw force data (fig.3.5). The strain data point corresponding to the time stamp vector, generated from the correct force data points were obtained. The strain data mean, median and variance were obtained.

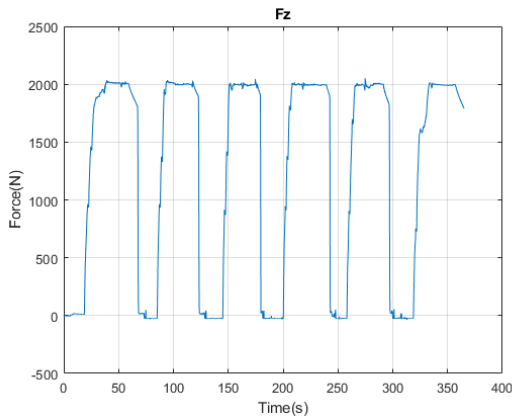


Figure 3.5: Raw Force data

Data sets from strain gauges with low strain were not compared with FEA. The lower strain values had a high amount of noise (fig. 3.7) and strain gauge tolerance issues came into play. Only the highest load levels were compared, as the largest strain levels were reached. An example of a data set from the bellcrank gauge can be seen in fig. 3.6 and fig. 3.7. Data sets from the push rod and A-arm were filtered with the a Matlab low pass filter function as these had more noise then the other gauges.

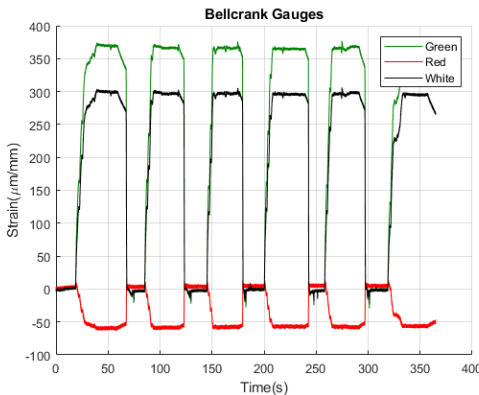


Figure 3.6: Bellcrank strain data, Fz load

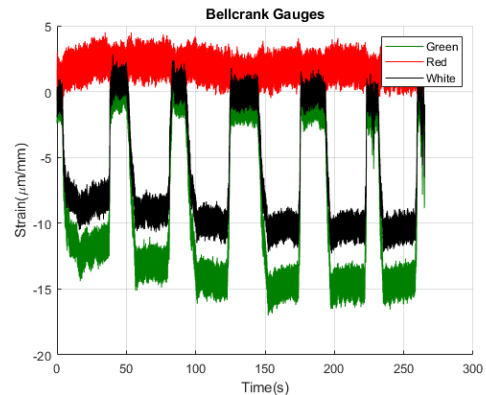


Figure 3.7: Bellcrank strain data, Fx load

3.4 Data Extraction

3.4.1 Strain Gauge Modelling and Data extraction

To extract strain results from the FEA, strain gauges were modeled in Abaqus CAE by Dassault Systemes. They were first drawn in Solidworks, in the correct coordinate system. This enabled the correct placement when imported into Abaqus. The gauges were modeled as surfaces with the corresponding sizes to the gauges used in the QST. Note: Only the grid size dimensions were included in the analysis. The gauges were assigned a membrane section. The gauges were modeled linear elastically with a Young's modulus of 0.1 MPa and a poisson's ratio of 0.1. A coordinate system was made inline with the strain direction, indicated by the white arrow in fig. 3.8. This allowed for transformation of strain to the correct direction, corresponding to the longitudinal direction of the strain gauge. The coordinate system was defined in the abaqus input file.

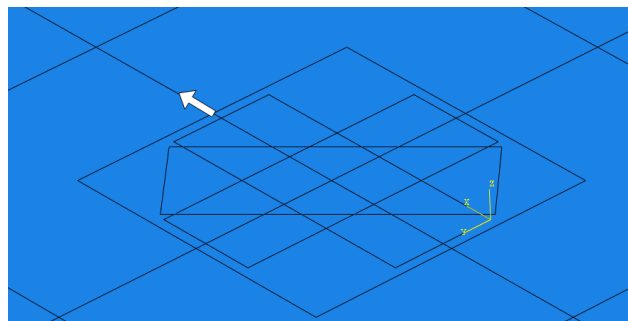


Figure 3.8: Coordinate system x-axis aligned with strain direction

3. APPROACH

Strain values in the appropriate direction were then averaged across all integration points in the strain gauge mesh. These values were then averaged to get a finite value for the gauge. The validity of this approach was verified through simple analytic calculations. See Appendix A.

3.4.2 Strain Gauge Placement

The following parts were equipped with strain gauges:

- Bellcrank (1 rosette)
- Lower Angle Lock (1 rosette)
- Push rod (1 single axis)
- Front upper Aft (FUA) A-arm Rod (1 single axis)

Strain gauges in the rosettes were given names based on the colour of their lead wire. The position of the gauges can be seen in the picture below (3.9).

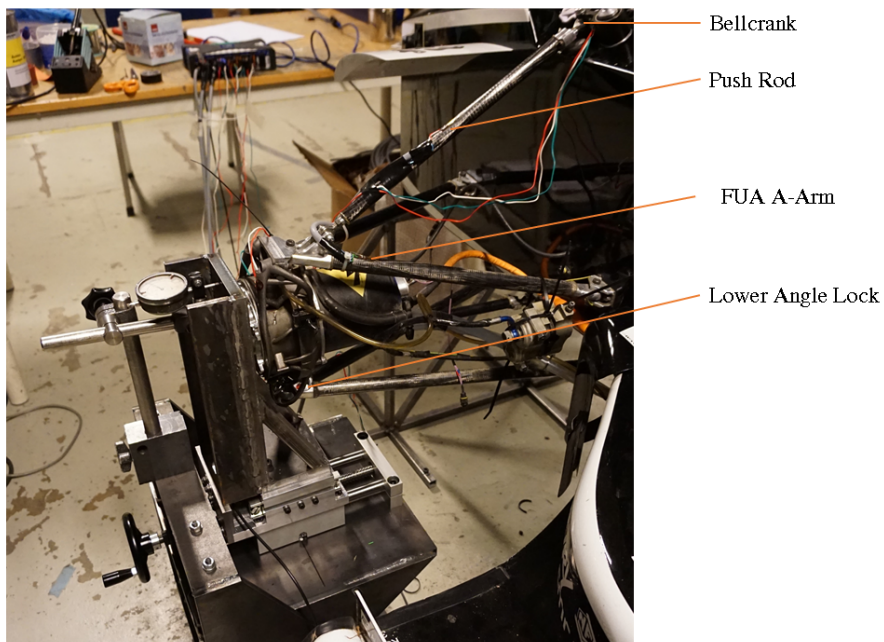
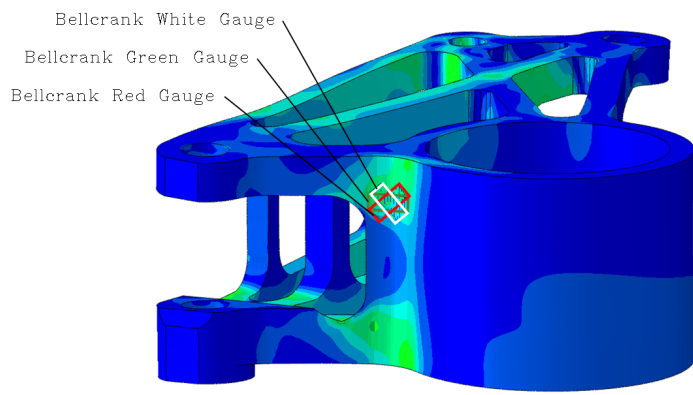


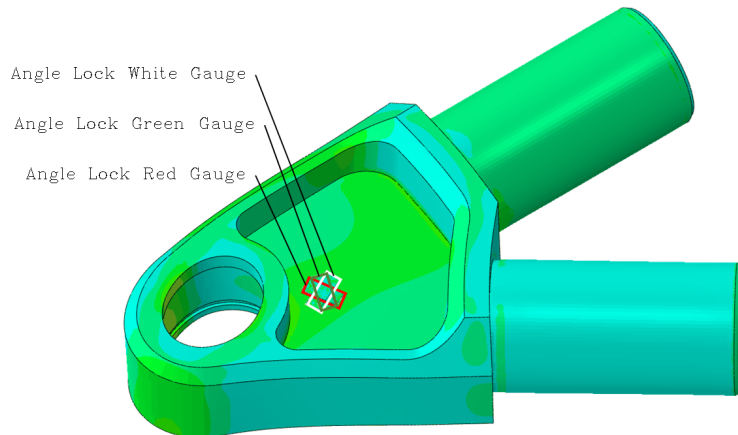
Figure 3.9: Location of each strain gauge

The locations were based on initial FEA of the suspension rods and bellcrank. Hot spots for strain were noted, and the strain gauges were placed accordingly. Information about the FEA models compared in this thesis are listed in Appendix A.

3. APPROACH



(a) Bellcrank



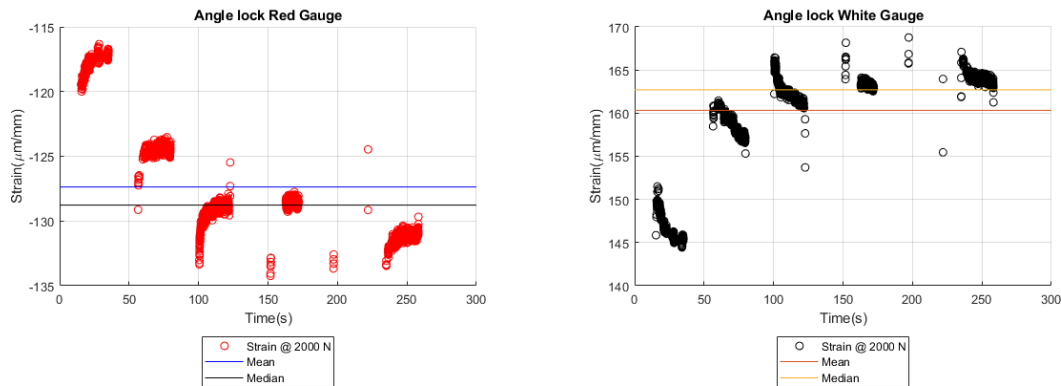
(b) Lower Angle Lock

Figure 3.10: Strain Gauge placement on bellcrank and Angle lock

4 Results

Results presented are from the quasi static testing and FEA. The data is presented for each load direction. The data used for comparison with FEA averages is shown, with the mean and median. The percentage deviation has been calculated for each strain gauge.

4.1 X-Direction - 1000 N

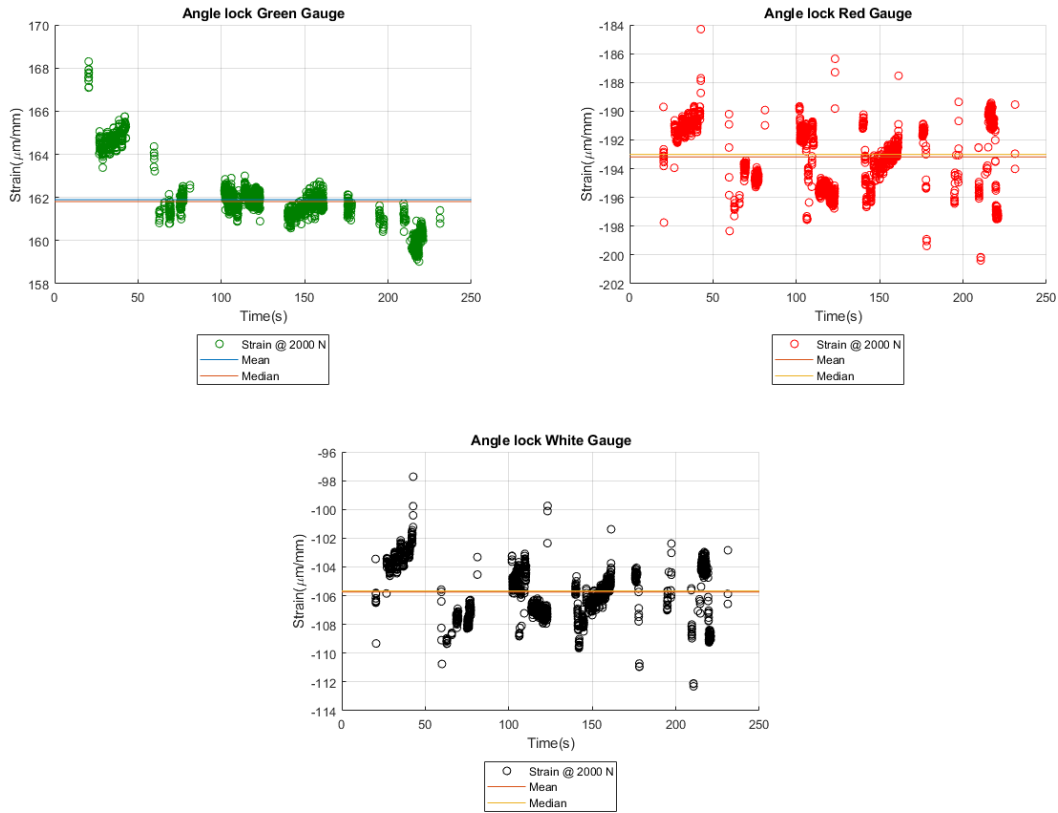


Strain Gauge Data					
Strain Gauge	Median Strain $\frac{\mu m}{mm}$	Variance $(\frac{\mu m}{mm})^2$	Mean Strain QST $\frac{\mu m}{mm}$	Mean Strain FEA $\frac{\mu m}{mm}$	Percentage Dev %
Angle Lock Red	-128,77	18,30	-127,37	-575,93	552,2
Angle Lock White	162,70	29,79	160,33	575,02	459,21

Table 4.1: Strain Data lower angle lock 1000 N X-direction

4. RESULTS

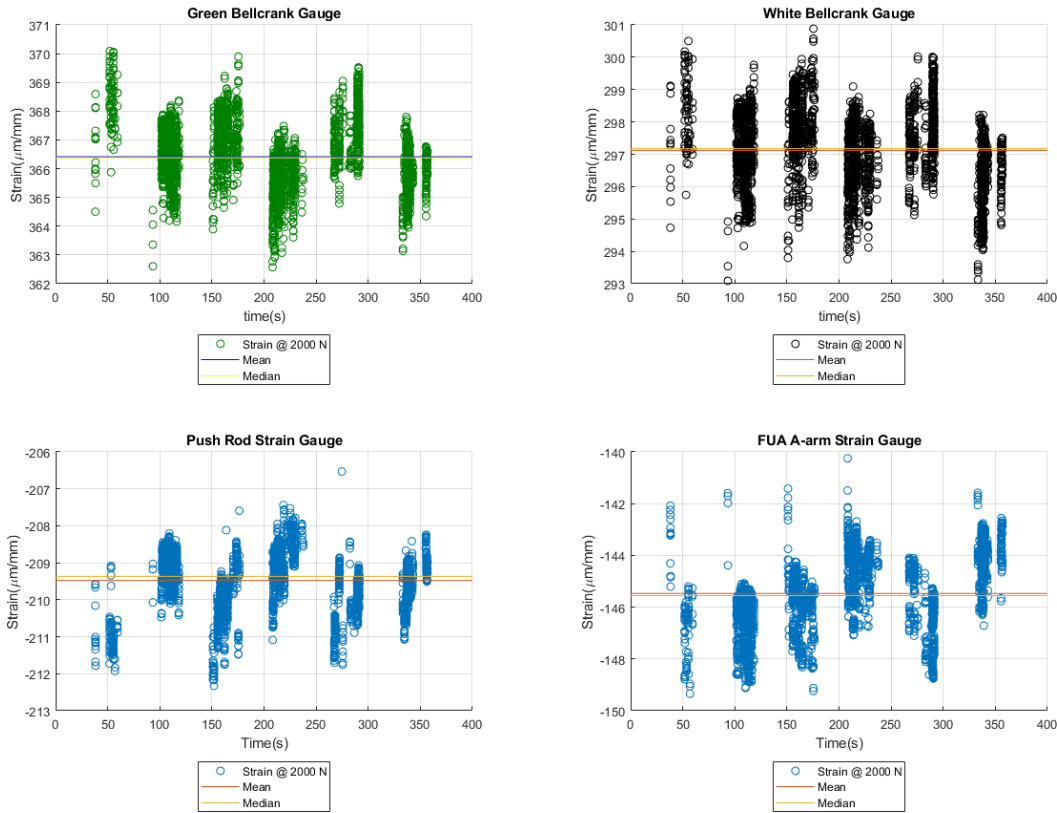
4.2 Y-Direction - 2000 N



Strain Gauge Data					
Strain Gauge	Median Strain $\frac{\mu\text{m}}{\text{mm}}$	Variance $(\frac{\mu\text{m}}{\text{mm}})^2$	Mean Strain QST $\frac{\mu\text{m}}{\text{mm}}$	Mean Strain FEA $\frac{\mu\text{m}}{\text{mm}}$	Percentage Dev %
Angle Lock Green	161,81	1,90	161,89	193,37	16.3
Angle Lock Red	-193,01	4,82	-193,18	-161,3	19,8
Angle Lock White	-105,67	3,12	-105,74	-116,94	9,01

Table 4.2: Strain data lower angle lock 2000 N Y-direction

4.3 Z-Direction - 2000 N



Strain Gauge Data					
Strain Gauge	Median Strain $\frac{\mu m}{mm}$	Variance $(\frac{\mu m}{mm})^2$	Mean Strain QST $\frac{\mu m}{mm}$	Mean Strain FEA $\frac{\mu m}{mm}$	Percentage Dev %
Bellcrank Green	366,38	1,26	366,41	887,89	58,7
Bellcrank White	297,17	1,34	297,12	821,04	63,8
FUA A-arm	-145,55	2,05	-141,46	-240,66	41,2
Push rod	-209,36	0,57	-208,67	-292,43	28,6

Table 4.3: Strain data lower angle lock 2000 N Z-direction

5 Discussion

5.1 Main Findings

Comparing the rod FEA and QST shows a correlation between FEA and QST which varies from 9.01 % to 552 %. The bellcrank model comparison shows a correlation ranging from 58.7 % to 63.8 %.

5.2 FEA

An unusual trend can be seen in all the results. The FEA shows more strain than QST results. A concrete reason for this has not been found in literature. In an article written by Peter Barrett the importance of the boundary conditions are stated when comparing FEA to experimental data [12]. The boundary conditions have not been adjusted in either model in this thesis. In the experiment conducted by Lisle et. al [13], it can also be seen how they simulate their part with the whole experimental set-up. A simulation with more accurate boundary conditions was planned, but this was not feasible within the time frame of this thesis.

5.2.1 Suspension rod model

The results compared in the suspension rod model showed the best and worst correlation of all the data sets extracted. It seems that the model is very sensitive to the loading direction as the X-directional load resulted in extreme deviation between FEA and QST. A concrete reason to why this occurs, has not been found.

5.3 Bellcrank model

The model has several simplifications done to keep run time of the simulation low. A more crucial simplification found in the model is that the dummy bearings have been simulated with having a friction coefficient of 0.3 to the axle. Changing this coefficient to a frictionless property, yields a different result, closer to the tested data. The figure below (5.1) shows the simulation result of the green bellcrank gauge. The left result is with the adjusted friction coefficient. The result on the right is the gauge used to calculate the mean presented in the thesis, i. e the model used by Revolve NTNU 2018 team.

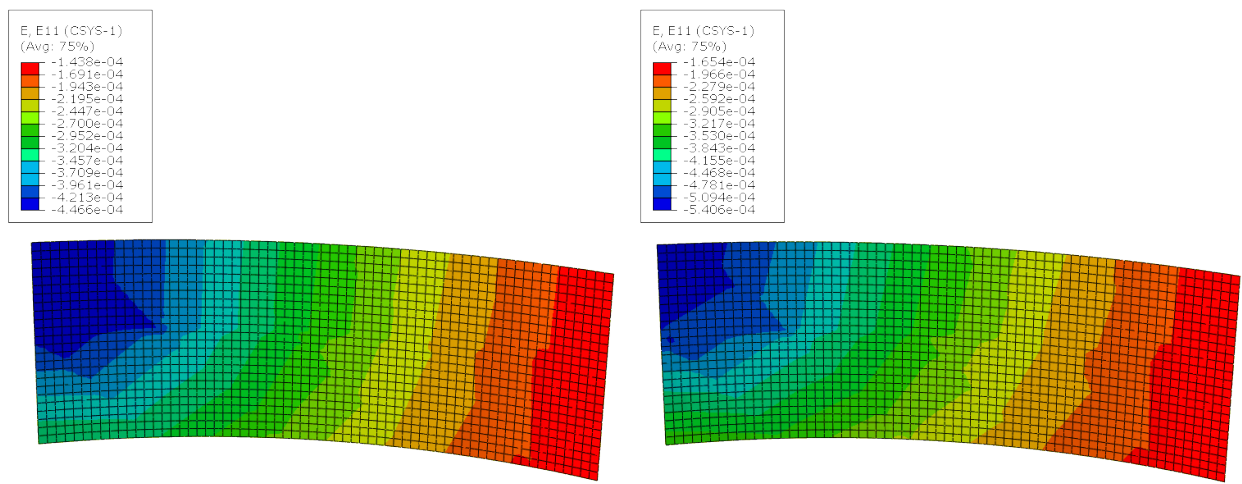


Figure 5.1: Left Mean strain: $693 \frac{\mu m}{m}$ Right Mean strain: $883 \frac{\mu m}{m}$

When extracting results from the bellcrank model, a cylindrical coordinate system was made. This was done since the gauge was glued to a curved face. This method was not verified in a more simple model. The direction of strain was checked, and noted to be along the gauge surface. This was also the case in the simplified strain gauge model.

5.4 Uncertainties in the experiment

A great part of the work done in this thesis was focused on the quasi static test jig. The jig was at first designed to have a single force transducer located directly under the tire dummy. This meaning, that only the tire dummy would be between the force reading and

5. DISCUSSION

the suspension of the vehicle. In the actuator used, the force transducers used needed to be placed where it was mechanically possible and where they fit. This placement introduced more parts in between the force reading and the suspension, and the force reading can have become inaccurate because of this.

When the actuator was placed and secured to the floor, it did not fit correctly. When the actuator was in the correct position the hub interface and the tire dummy did not align. An adjustment to the dummy damper had to be made. It was made shorter until the tire dummy fit correctly. This places the suspension in a slightly different position to what it has in the FEA. This will effect how forces propagate through the suspension, and will alter the strain readings.

Two of the strain gauges used in the experiment (FUA A-arm and push rod) needed to be soldered before mounting to the car. The soldering was hard to do correctly with the equipment at hand. This raises some doubt to the strain gauges and their results. The FUA A-Arm gauge and the push rod gauge are clearly more noisy than the other gauges, as mentioned a low pass filer was used. This raises questions towards their validity.

While mounting the strain gauges it was challenging to place the strain gauges correct according to the positions found in FEA. Both the bellcrank and angle lock are relatively small parts with awkward geometry. Both the hot spots targeted for strain gauge placement on the bellcrank and angle lock were placed at an awkward angle and curvature. An attempt was made to place the gauge as straight as possible along the curvature. The paper by Lisle et. al [13] assumes an accuracy of +/- 0.5 mm in placing of strain gauges manually. In their experiment, the strain gauge application area was larger application area. This shows that a concern towards the results achieved in this thesis, can be related to the placement of the gauges.

6 Conclusion and Further Work

The aim of this thesis was do gain knowledge in the comparison between FEA and testing. Testing has been performed on the front left suspension system. A simple method for extracting and comparing results from FEA has been verified, and used. The method has been used to compare test results to two independent FEA models, used by the 2018 Revolve NTNU team. The results show a non satisfactory correlation between the FEA and the QST.

In retrospect, looking at the results, the scope of this specialization project should have been narrowed down to a more simple approach. The results presented are largely affected by the fact that during the project more uncertainties came into play then what was first thought of.

For further work it is recommended to take a close look at the FE models. The boundary conditions need to be corrected to the experiment. In the FEA done in the paper by Monaheng et. al [8] surfaces for strain extraction were marked, instead of simulating actual gauges. This might be a more efficient way to get accurate results, as it does not introduce more parts. It also removes interactions needed between different parts in the FEA.

For further experimentation, more simple and less time consuming experiments should be conducted before doing a complete system experiment, like the one done in this thesis. This can most likely pave the way for obtaining better results and more use full answers in terms of usability in the vehicle design. Here again, a focus must be had on correct boundary conditions. It is also recommended to pay close attention and verify the testing jigs. This can eliminate a great deal of uncertainty.

Even though the results are not acceptable in terms of using them in the design of future vehicles, the knowledge benefit of the project is large. The project has succeeded in uncovering potential pitfalls and difficulties when it comes to executing proper testing and validation.

References

- [1] FSHist. *History of Formula Student*. URL: <https://www.imeche.org/events/formula-student/about-formula-student/history-of-formula-student>.
- [2] W F Milliken, D L Milliken, and Society of Automotive Engineers. *Race Car Vehicle Dynamics*. Premiere Series. SAE International, 1995. ISBN: 9781560915263. URL: <https://books.google.no/books?id=opgHfQzlnLEC>.
- [3] D Seward. *Race Car Design*. Macmillan Education UK, 2014. ISBN: 9781137030146. URL: <https://books.google.no/books?id=d7jloAEACAAJ>.
- [4] MARTIN KRÖNKE. *5.6: Camber & Toe - Virtual Racing School (VRS)*. 2017. URL: <https://virtualracingschool.com/academy/iracing-career-guide/setups/camber-toe/>.
- [5] “Stiffness — an unknown world of mechanical science?” In: *Injury* 31 (May 2000), pp. 14–84. ISSN: 0020-1383. DOI: 10.1016/S0020-1383(00)80040-6. URL: <https://www.sciencedirect.com/science/article/pii/S0020138300800406>.
- [6] *FSG: Pat's Seven Deadly Sins of FS Design*. URL: <https://www.formulastudent.de/pr/news/details/article/pats-seven-deadly-sins-of-fs-design/>.
- [7] *Why is compliance so important? - F1technical.net*. URL: <https://www.f1technical.net/forum/viewtopic.php?t=8947>.
- [8] LF Monaheng et al. “Strain gauge validation of finite element analysis of a Ti6Al4V (ELI) mandibular implant produced through additive manufacturing”. In: *Proceedings of the 17th Annual International Conference of the Rapid Product Development Association of South Africa* 978-0-620-72061-8 (2016).
- [9] *Practical Strain Gage Measurements Omega*. Tech. rep. URL: https://www.omega.com/techref/pdf/StrainGage_Measurement.pdf.
- [10] *Wheatstone bridge - Wikipedia*. URL: https://en.wikipedia.org/wiki/Wheatstone_bridge.
- [11] Norman E. Dowling, Katakam. Siva Prasad, and R. Narayanasamy. *Mechanical behavior of materials : engineering methods for deformation, fracture, and fatigue*. 4th ed., i. Boston, Mass: Pearson Education, 2013, p. 954. ISBN: 0273764551. DOI: 10.1017/CBO9781107415324.004. URL: <http://cds.cern.ch/record/2064030>.
- [12] *Tips & Tricks for Matching FEA Results to Physical Data / CAE Associates*. URL: <https://caeaxi.com/blog/tips-tricks-matchingfea-results-physical-data>.

- [13] Timothy J. Lisle, Brian A. Shaw, and Robert C. Frazer. "External spur gear root bending stress: A comparison of ISO 6336:2006, AGMA 2101-D04, ANSYS finite element analysis and strain gauge techniques". In: *Mechanism and Machine Theory* 111 (May 2017), pp. 1–9. ISSN: 0094-114X. DOI: 10.1016/J.MECHMACHTHEORY.2017.01.006. URL: <https://www.sciencedirect.com/science/article/pii/S0094114X16303159#bib0036>.
- [14] Dassault Systèmes SE. "Membrane elements". In: URL: <https://abaqus-docs.mit.edu/2017/English/SIMACAEELMRefMap/simaelm-c-membrane.htm>.

Appendix

1. Finite Element Analysis
2. Formula Student Competitions
3. Load Case 2018
4. HBM Quantum MX1615B
5. HBM 1-LY11-6/120A Data Sheet
6. TML FRAB-5-11-3LJB-F

A Finite Element Models

The following section will describe the finite element models used in this thesis. There are in total five models used. Three of the models are models from the 2018 season, which were modified to fit with the set-up of the QS test jig. A simple model was also made to access feasibility of result extraction through modeling strain gauges in Abaqus.

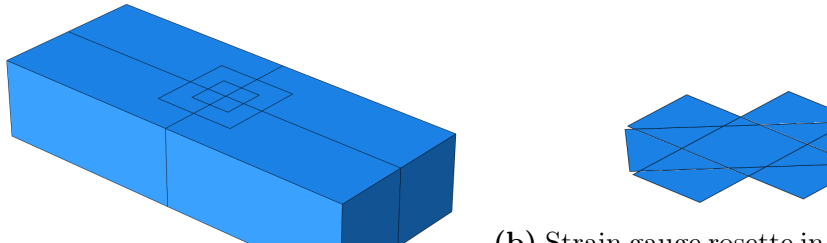
- Model Description
- Parts
- Part Properties
- Assembly and Steps
- Interactions
- Loads
- Mesh

A.1 Strain Gauge Simplified Model

The idea behind this model was to verify if the modelling of strain gauges through membrane section and tie constraint could work. The way this was done was through accessing mesh convergence and following the results are satisfactory and verified through simple analytical hand calculations.

A.1.1 Parts

The model consists of 4 parts. Block, and three strain gauges. The the gauges are placed like the strain gauge rosettes used in the physical testing. The block was given the dimension 20x10x50 mm.



(b) Strain gauge rosette in Abaqus CAE

(a) Block

Figure A.1: Strain gauge simplified model parts

A.1.2 Part Properties

The block is simulated as regular steel, with linear elastic and isotropic material behaviour. The strain gauges were given custom material properties. They have been given a low Young's modulus so that no contribution to the blocks stiffness would be added. They are also modeled linear elastically.

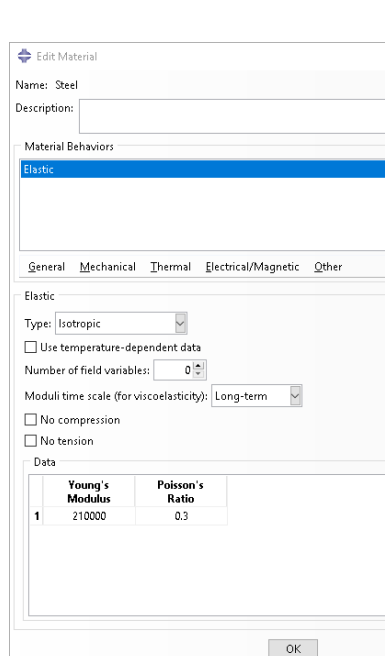


Figure A.2: Block Material

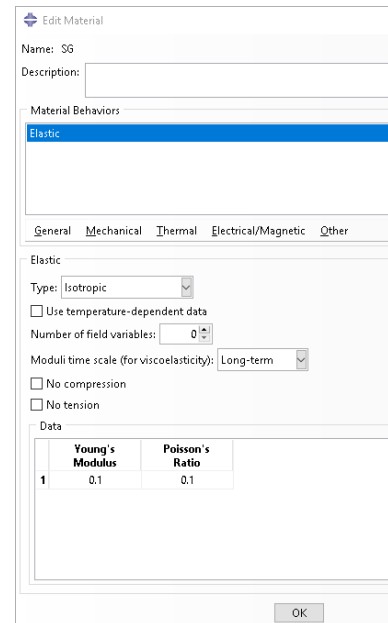


Figure A.3: Strain gauge material properties

A.1.3 Assembly and Steps

The simulation was run in one static, general step. Standard abaqus settings for incrementation and step time were kept.

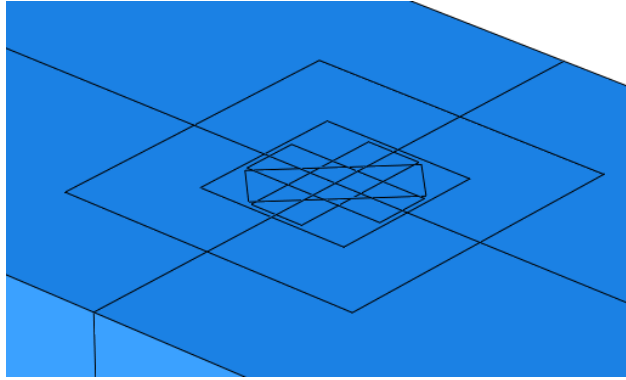


Figure A.4: Strain gauges assembled to the block

A.1.4 Interactions and Contact

To secure the strain gauges to the block a surface based tie constrain was employed. A surface-to-surface discretization method was chosen, opposed to a node-surface discretization. The tie constraint will transfers strain from a master surface to the slave surface, as the degrees of freedom of the slave surface follow that of the master. In this case the master is defined as the block and the strain gauges are defined as the slave surfaces [**DassaultSystemesSEMeshConstraint**].

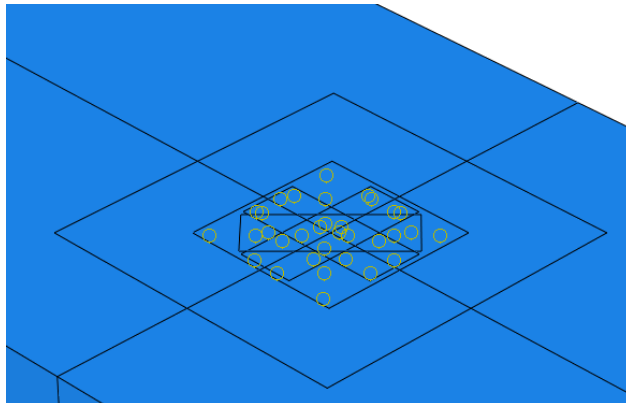


Figure A.5: Tie Constraint on surface

A Kinematic coupling was used to connect one side of the block to a reference point where the load was applied.

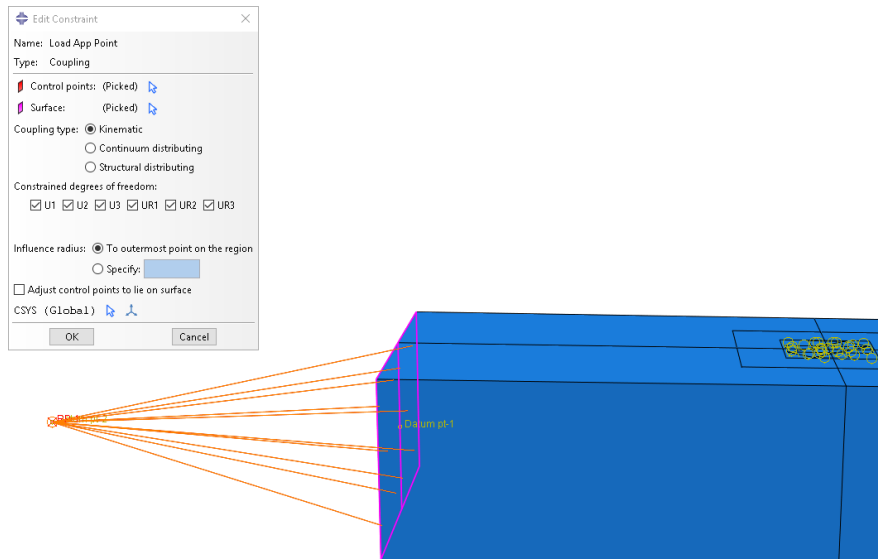


Figure A.6: Kinematic coupling

A.1.5 Loads and Boundary Conditions

An arbitrary load of 1000 N was applied. The load application was set at a geometric node, located a distance of 20 mm in the negative x-direction away from the center node of one side of the block. The other short side has an encaster BC applied securing the block in all DOFs.

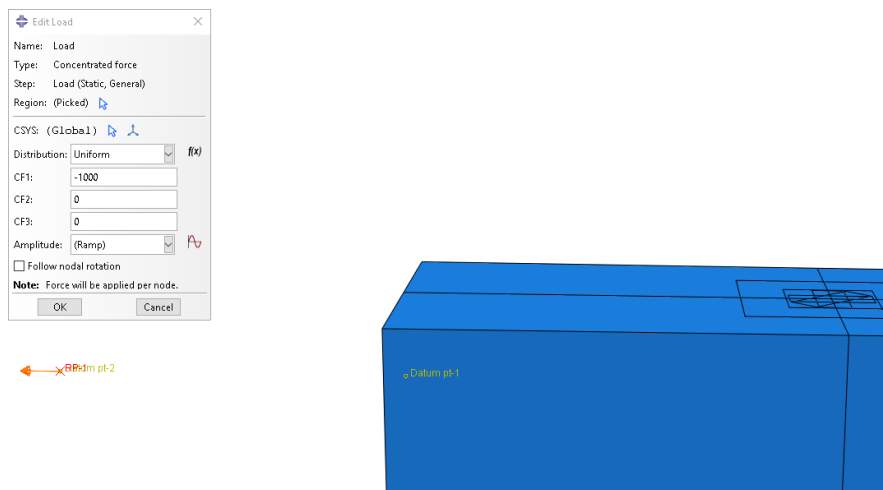


Figure A.7: Load application

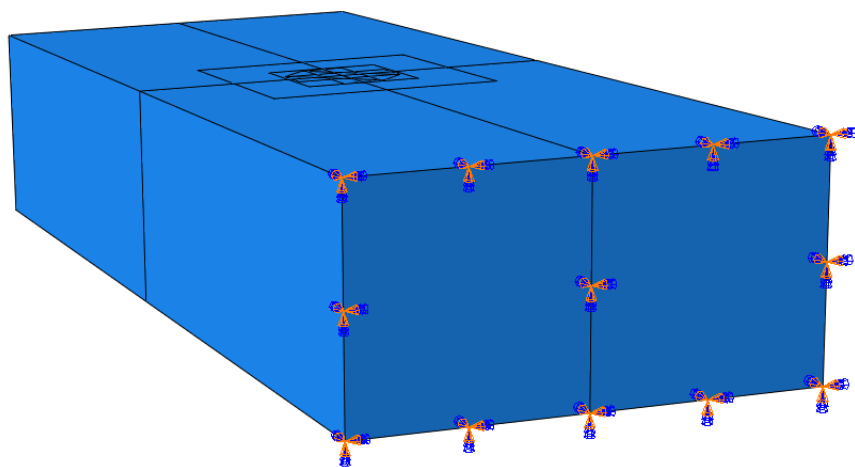


Figure A.8: Short side Boundary condition on Block

A.1.6 Mesh

The block was partitioned into three sections. From the outside and inn, the mesh was gradually refined towards the strain gauges. The block used C3D8R, an 8-Node brick element. The gauges were meshed with membrane elements. Membrane elements are made to only add strength in the direction of the element, with no bending stiffness [14]. The membrane elements used were M3D8R, An 8-node quadrilateral membrane with reduced integration.

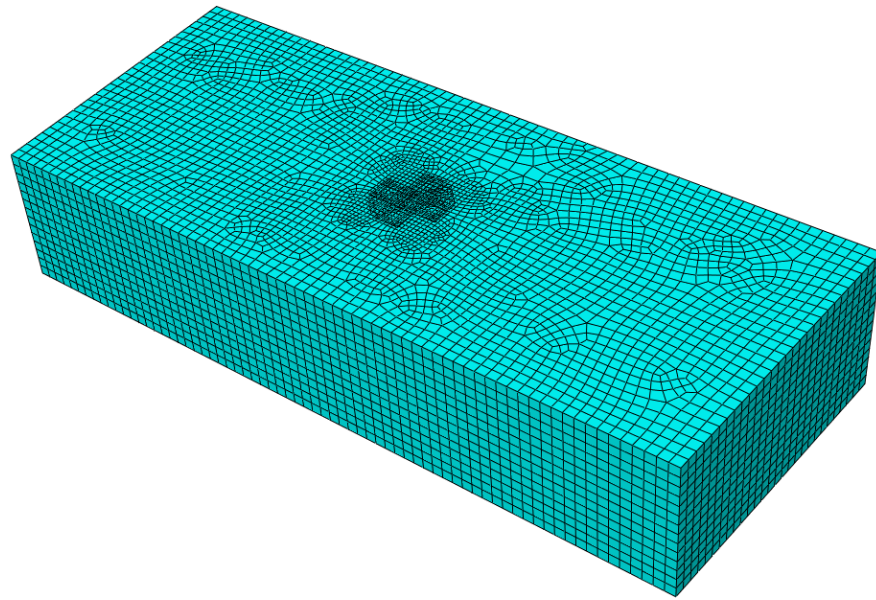


Figure A.9: Mesh

A.1.7 Results

Results from the strain gauge oriented in the direction of loading was extracted for comparison with simple analytically calculations.

Analytic calculations:

$$\begin{aligned}\sigma_{xx} &= \frac{F}{A} \\ \sigma_{xx} &= \frac{1000N}{20mm * 10mm} \\ \sigma_{xx} &= 5N/mm^2\end{aligned}\tag{6}$$

$$\begin{aligned}\sigma_{xx} &= E * \epsilon \\ \epsilon_{xx} &= \frac{\sigma_{xx}}{E} \\ \epsilon_{xx} &= \frac{5N/mm^2}{210000N/mm^2} \\ \epsilon_{xx} &= 2.38e^{-5}\end{aligned}\tag{7}$$

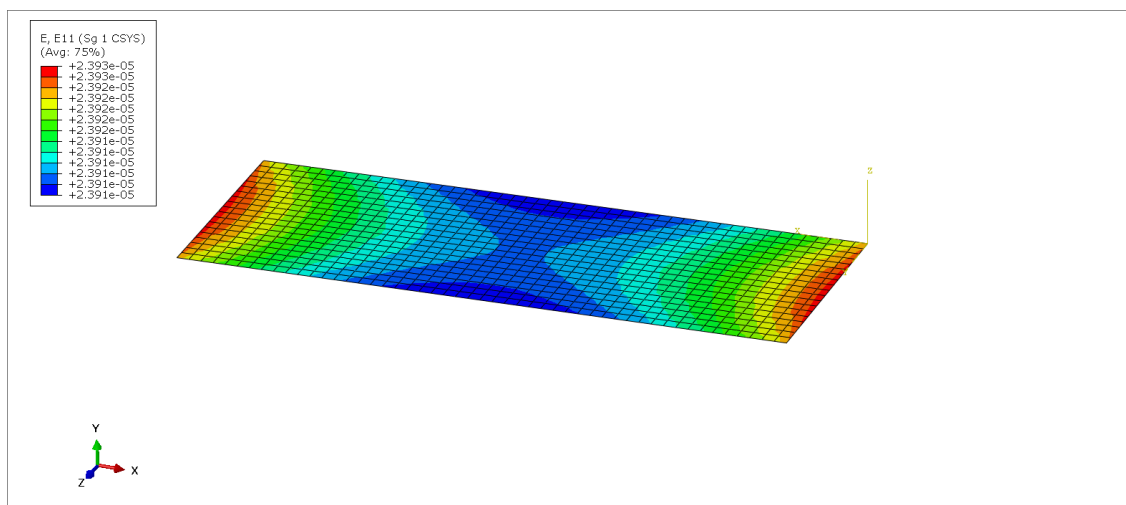


Figure A.10: Results from FEA showing $2.391e^{-05}$ to $2.392e^{-05}$

A.2 Bellcrank Model

A.2.1 Parts

The analysis consists of six parts in total.

- Bellcrank
- Bellcrank axle
- Two Dummy Bearings
- Two Dummy Bolts

Bellcrank, Bellcrank axle, two dummy bearings and two dummy bolts. All parts were modeled in solidworks and imported into Abaqus CAE.

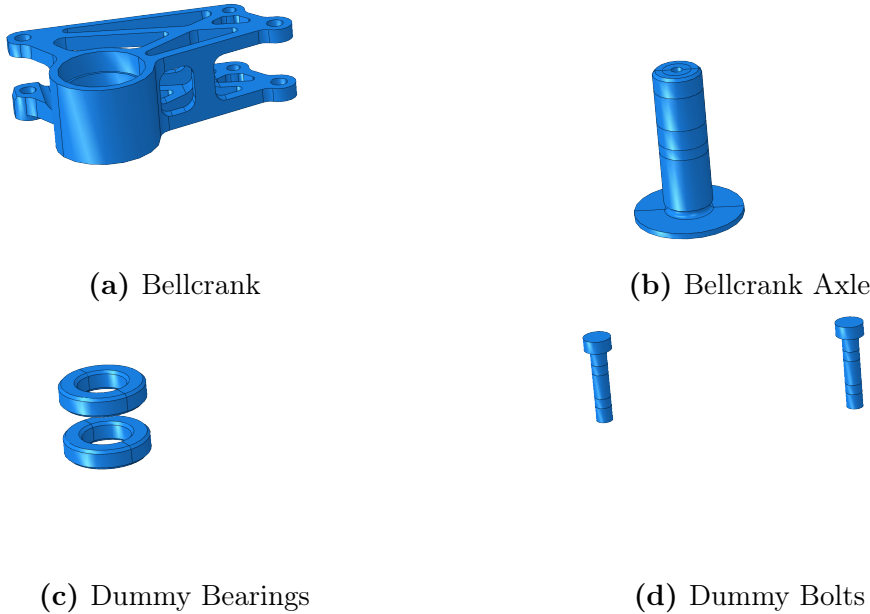
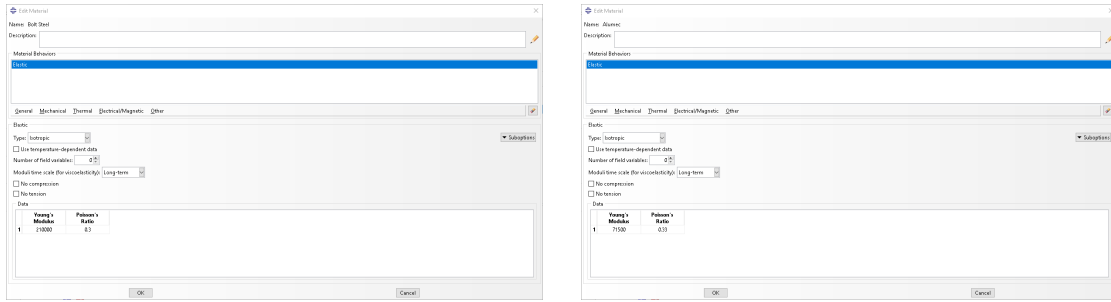


Figure A.11: Bellcrank Parts

A.2.2 Part Properties

The materials used in the simulation are Alumec-89 (Bellcrank and Axle) and Steel (Bearings and bolts). All materials were modeled as linear elastic and isotropic. All parts were modeled as solid homogeneous sections.



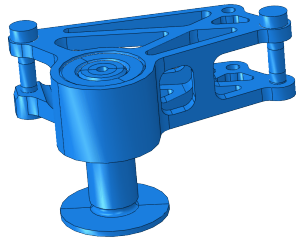
(a) Steel

(b) Alumec-89

Figure A.12: Materials Bellcrank Analysis

A.2.3 Assembly and Steps

The model was imported with the same coordinate system of the car in CAD. Before importing, the correct position of the assembly was set. All parts are meshed on part level. Two steps were made, contact and load. Basic settings were kept, except for changing initial step size to 0.25.



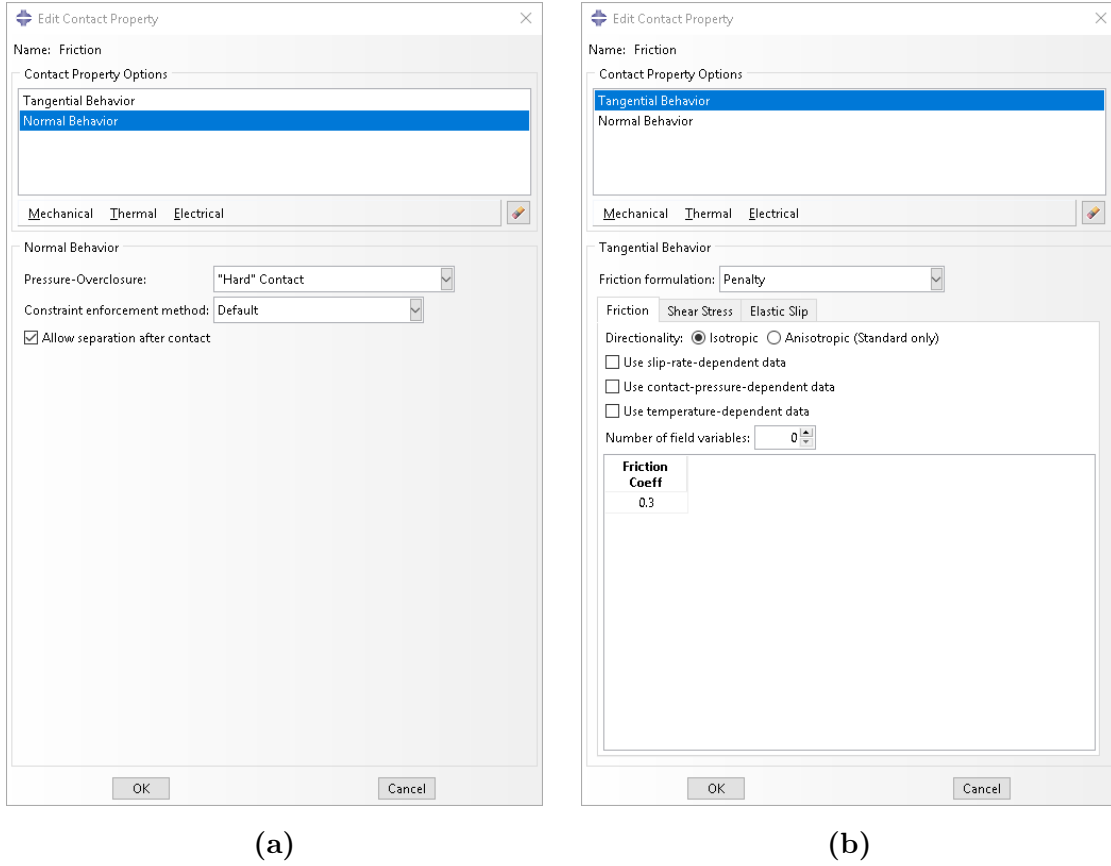
(a) Bellcrank Assembly in Abaqus CAE

Two overlapping dialog boxes from the Abaqus CAE software. The left dialog is the 'Step Manager' showing three defined steps: 'Initial', 'Contact', and 'Load'. The right dialog is the 'Edit Step' for the 'Load' step, which is a 'Static, General' type. It shows settings for 100 increments, an initial increment size of 0.25, and a minimum increment size of 1E-005. The 'OK' button is highlighted in blue.

(b) Steps

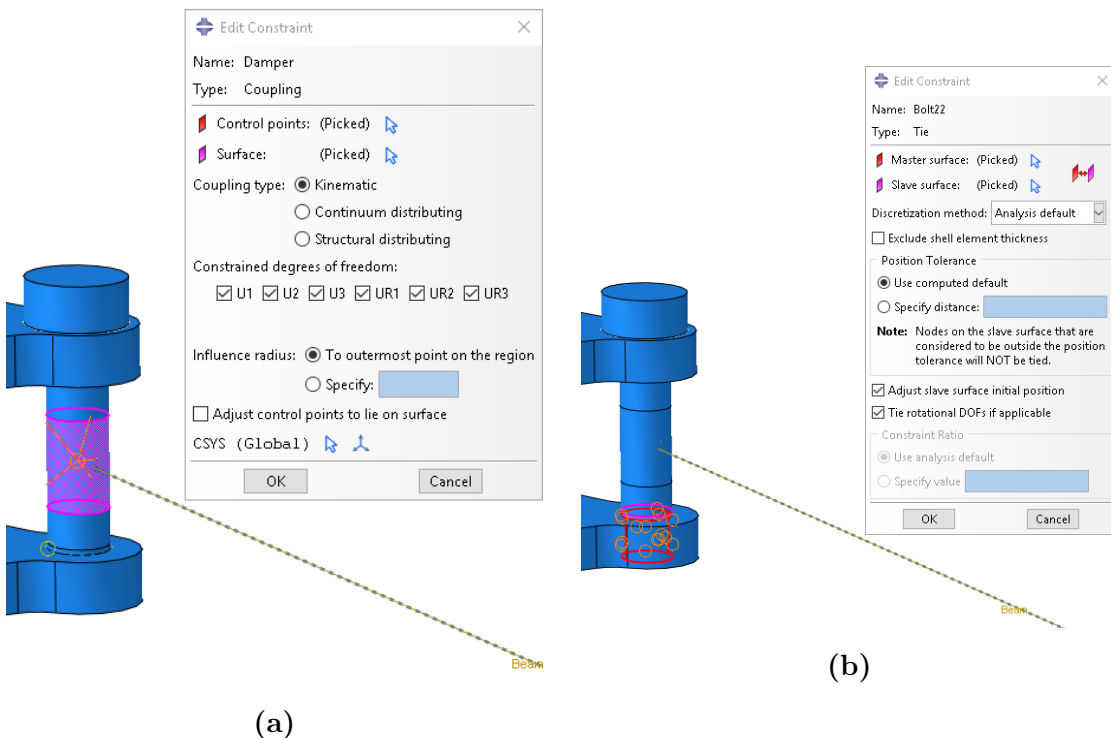
A.2.4 Interactions and Contact

Four contact interactions were created. These are between the bearings-axle and bearings-bellcrank. The bearing-axle contact was made in the initial step while the bearing-bellcrank contact is initiated in the contact step. All interactions are propagated to the load step.



A.2.5 Connectors

To simulate the correct load path through the assembly, beam connectors have been used. They are secured to the bolts at one end with a kinematic coupling, and assigned a boundary condition at the other end. All bolts are secured with tie constrains to simulate the threads.



A.2.6 Loads and Boundary Conditions

One load is applied at the push rod with a magnitude of 3310.66 N. A boundary condition is applied at the beam connector simulating the damper at its end stroke.

A.2.7 Mesh

The bellcrank is meshed using a C3D10 element. This is A 10-node quadratic tetrahedron. All other elements used are C3D20R, A 20-node quadratic brick with reduced integration.

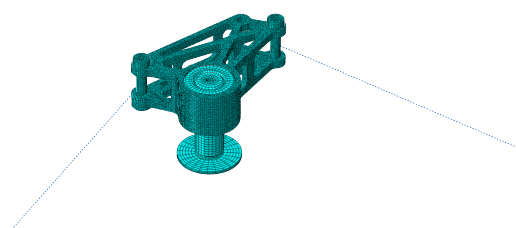


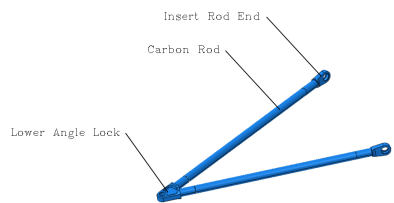
Figure A.16: Mesh overview

A.3 Suspension Rod Model

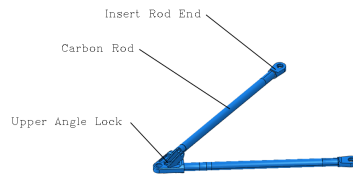
A.3.1 Parts

The model consists of multiple sub assemblies listed below.

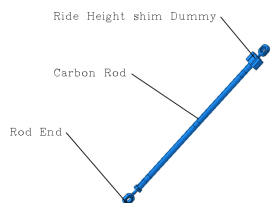
- Upper A-Arm
- Lower A-Arm
- Push rod
- Tie rod



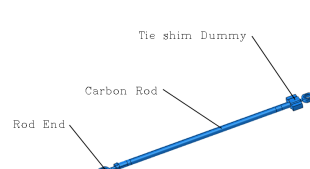
(a) Lower A-Arm



(b) Upper A-Arm



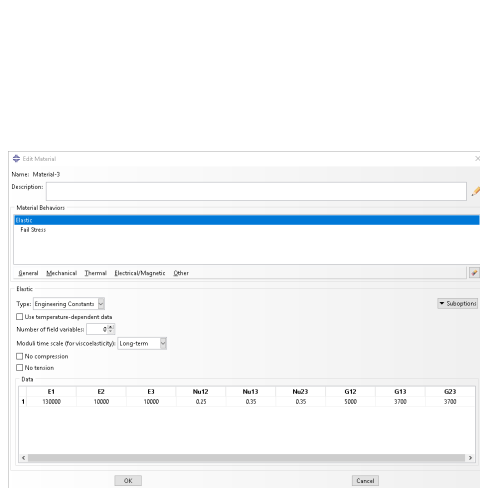
(c) Push Rod



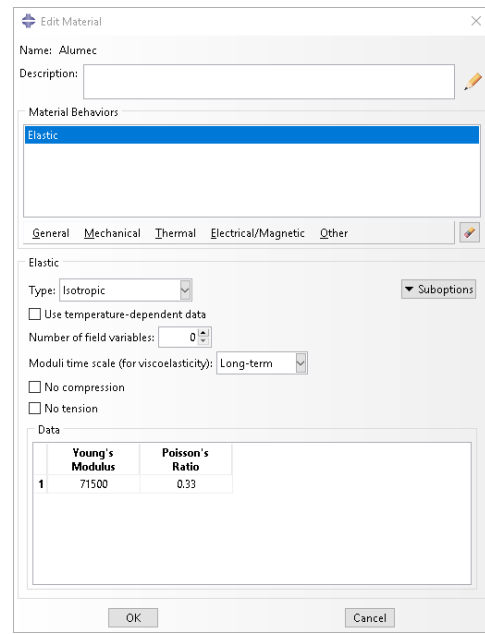
(d) Tie Rod

A.3.2 Part Properties

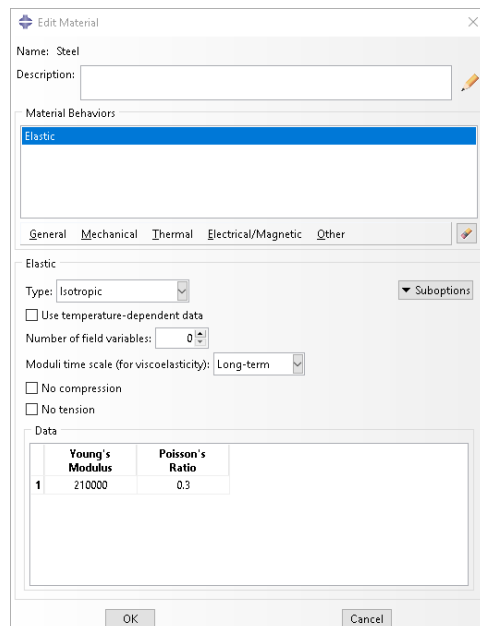
Insert Rod ends and angle locks are made of Alumec89. Rod ends are modeled as steel and the carbon rods are modeled with a specific lay-up, but same material properties.



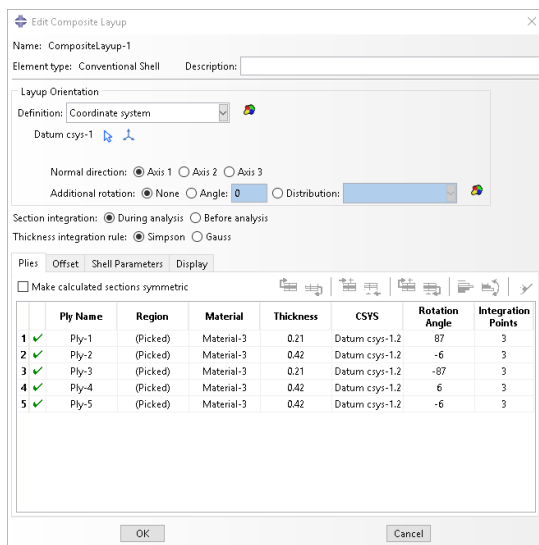
(a) Rod carbon material properties



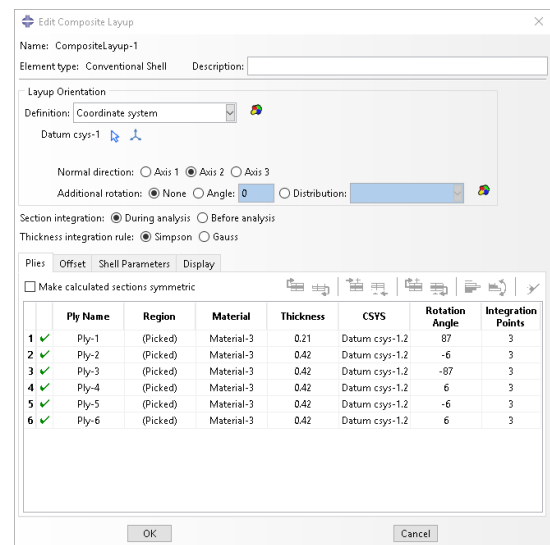
(b) Steel



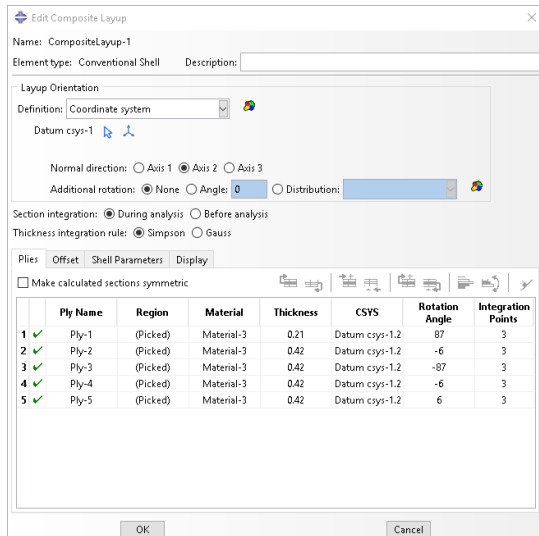
(c) Alumec89



(a) A-Arm layup



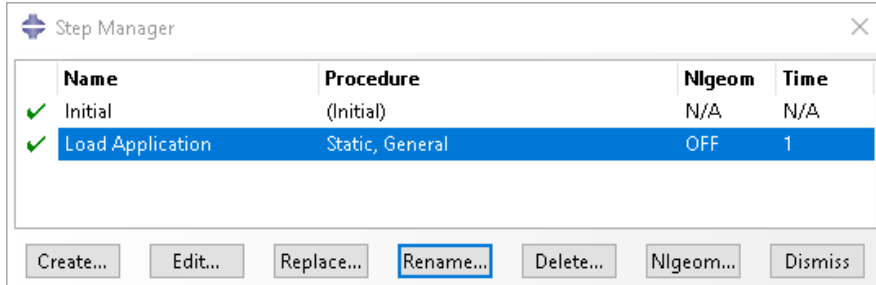
(b) Push Rod Layup



(c) Tie Rod Layup

A.3.3 Assembly and Steps

Like the bellcrank model, the rod model was imported into he Abaqus CAE interface in the correct coordinate system. Only one load application step was made and all standard step settings were kept.



The screenshot shows the 'Step Manager' dialog box. It contains a table with four columns: 'Name', 'Procedure', 'Nlgeom', and 'Time'. There are two rows in the table. The first row is for the 'Initial' step, which is listed under '(Initial)' in the 'Procedure' column and has 'N/A' in both 'Nlgeom' and 'Time' columns. The second row is for the 'Load Application' step, which is listed under 'Static, General' in the 'Procedure' column and has 'OFF' in the 'Nlgeom' column and '1' in the 'Time' column. The 'Load Application' row is highlighted with a blue background. Below the table are several buttons: 'Create...', 'Edit...', 'Replace...', 'Rename...', 'Delete...', 'Nlgeom...', and 'Dismiss'.

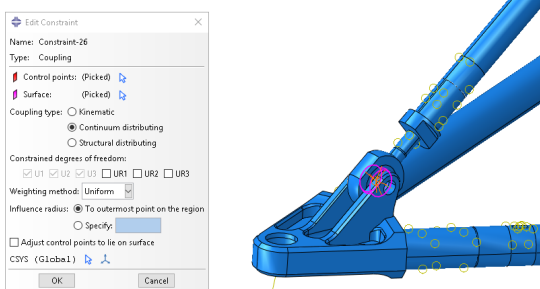
Name	Procedure	Nlgeom	Time
✓ Initial	(Initial)	N/A	N/A
✓ Load Application	Static, General	OFF	1

Buttons at the bottom: Create..., Edit..., Replace..., Rename..., Delete..., Nlgeom..., Dismiss

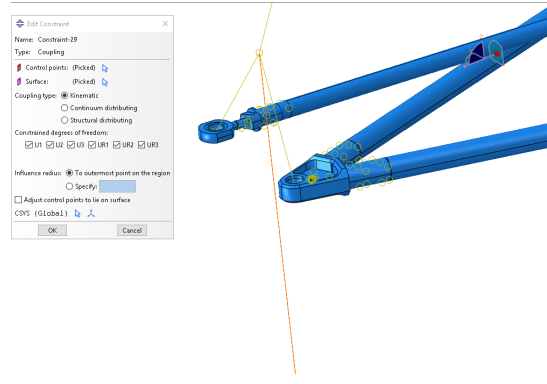
Figure A.20: Steps

A.3.4 Interactions and Contact

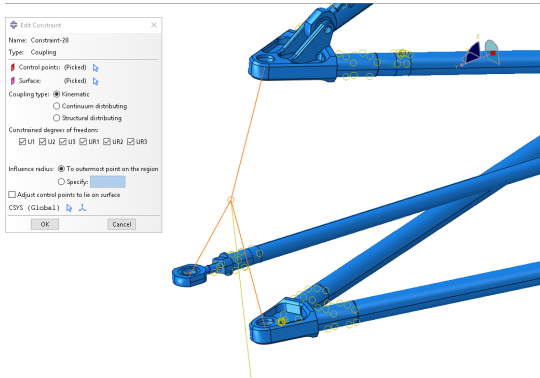
No contact was employed in this model. Interactions used were tie constrains between rods and aluminum parts. Kinematic couplings were used to connect the load application point to the rods and continuum couplings were used to propagate loads instead of spherical bearings.



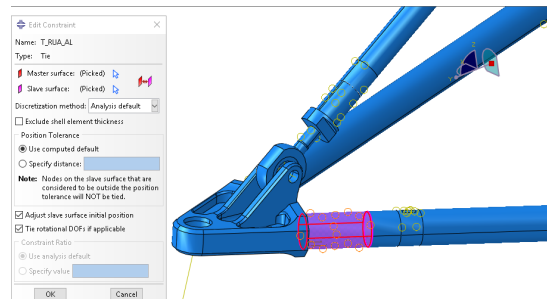
(a) Continuum Coupling



(b) Kinematic Coupling - Wheel



(c) Kinematic Coupling - Upright



(d) Tie - Rod to Aluminum



(e) Spherical Bearing

A.3.5 Loads and Boundary Conditions

Boundary conditions used are pinned.

The model is run with a X-load, y-load and z-load at the contact patch. The loads were not run simultaneously.

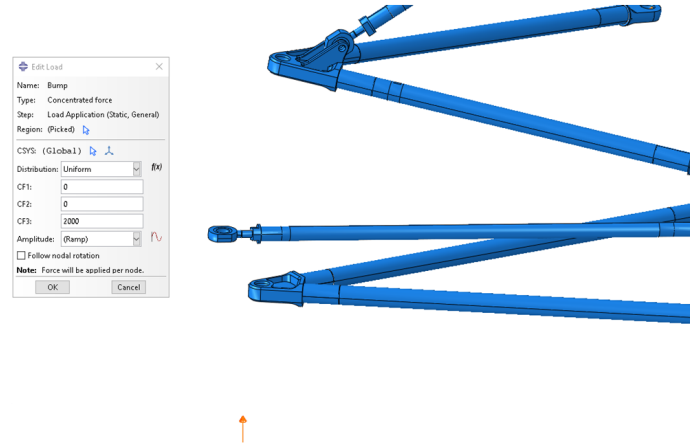


Figure A.22: Load application in Z-direction

A.3.6 Mesh

The mesh used in the model consists of three different types. All aluminum parts are meshed with C3D10, A 10-node quadratic tetrahedron. The rods with gauges were meshed with S8R elements. This is a 8-node doubly curved thick shell element with reduced integration. The elements on the rods without strain gauges are S4R.



Figure A.23: Rod Model Mesh overview

B Formula Student Events

This section details the different formula student events.

Static Events

- **Engineering Design (150 points)**

Students compete present their designs to judges from the automotive, racing industry. Points are scored on solutions, knowledge and design.

- **Cost and Sustainability Analysis (100 points)**

Teams are awarded for designs and solutions yielding the highest cost efficiency

- **Business Presentation (75 points)**

A business plan is presented for selling the vehicle made. Scores are awarded on the best selling solution.

Dynamic Events

- **75 m Acceleration (75 points)** 75 m long acceleration. Test of longitudinal capabilities.

- **Skid Pad (75 points)** Figure eight track. Test of steady state lateral capabilities

- **1 km Autocross (100 points)** Track from start to finish (no laps). Goal to test of overall maximum capabilities of the car.

- **Endurance (325 points)** 22 km endurance race with similar track layout to the autocross, but multiple laps.

C Load Case 2018

-----Tire Load Case-----						
WarmTire						
Comments:						
Acceleration does not take into account motor capabilities only power limit - 80kW power to the ground is conservative						
-----Front wheels-----						
Turn@110kph		Acceleration	Brake@110kph	3gBump	2gBump+Turn@110kph	2gBump+Brake@110kph
Inside Wh.	Outside Wh.					
Fx	0 N	0 N	514 N	3262 N	0 N	3262 N
Fy	670 N	3166 N	0 N	0 N	3166 N	0 N
Fz	280 N	2153 N	507 N	1926 N	1756 N	3324 N
						3097 N
-----Rear wheels-----						
Turn@110kph		Acceleration	Brake@110kph	3gBump	2gBump+Turn@110kph	2gBump+Brake@110kph
Inside Wh.	Outside Wh.					
Fx	0 N	0 N	2463 N	1236 N	0 N	1236 N
Fy	910 N	3182 N	0 N	0 N	3182 N	0 N
Fz	390 N	2195 N	1297 N	583 N	1864 N	3437 N
						1826 N

Figure C.1: Load cases 2018

QUANTUM^X

MX1615B

Strain gauge bridge amplifier

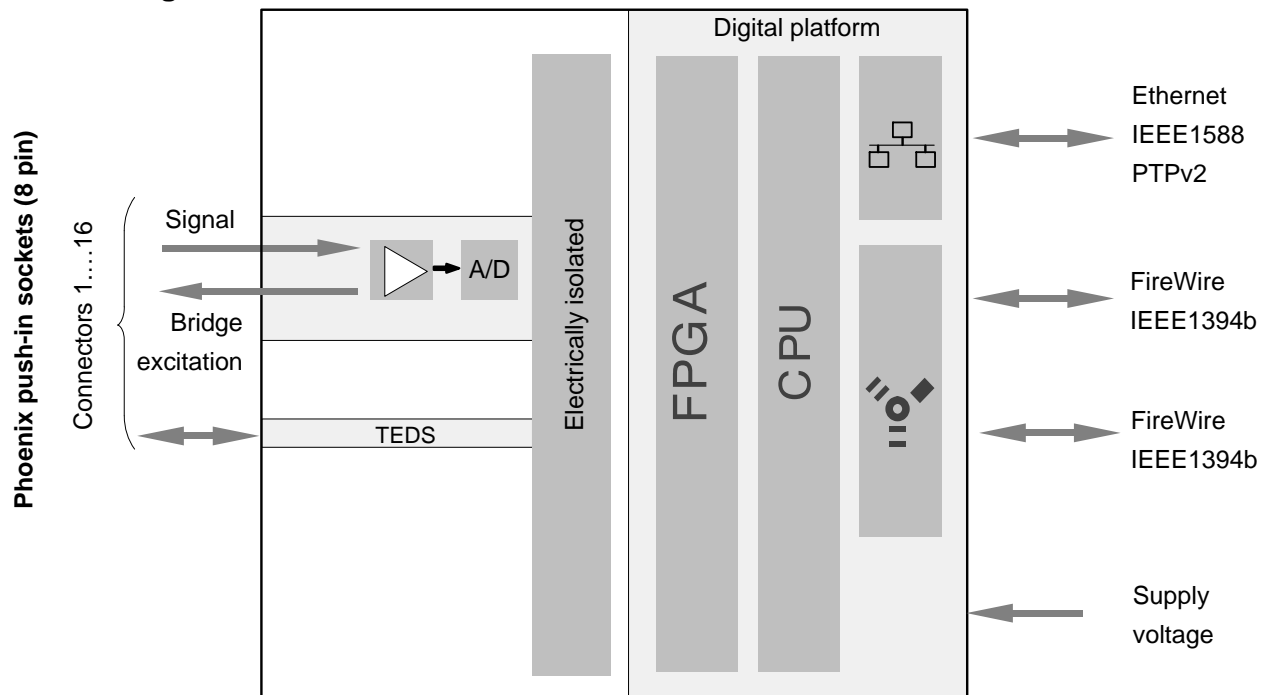
Data sheet



Special features

- 16 individually configurable inputs
- Connection of strain gauges in full-, half-, or quarter-bridge (120 or 350 Ohm)
- Bridge excitation : DC or carrier frequency
- Internal shunt resistor
- Connection of standard voltage, PT100, resistor, Potentiometer
- Individual data rates up to 20 kS/s per channel, active low pass filter
- 24-bit A/D converter per channel for synchronous, parallel measurements

Block diagram



Series Y

With one measuring grid / linear strain gauge

LY11

Linear strain gauge

Temperature response matched to steel
with $\alpha = 10.8 \cdot 10^{-6}/K$

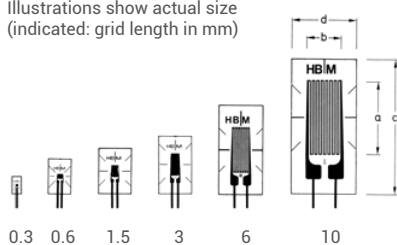
LY13

Temperature response matched to aluminum
with $\alpha = 23 \cdot 10^{-6}/K$

LY1x

Temperature response matched to customer's choice
see page 16

Illustrations show actual size
(indicated: grid length in mm)



Contents per package: 10 pcs.

Steel	Aluminum	Other	Ω	Measuring grid		Meas. grid carrier		Maximum excitation voltage (*)	Sldr. terminals
				a	b	c	d		
				V					
1-LY11-0.3/120		1-LY1x-0.3/120(#)	120	0.3	0.9	2	1.2	0.6	LS 7
1-LY11-0.6/120	1-LY13-0.6/120	1-LY1x-0.6/120(#)	120	0.6	1	5	3.2	1.5	LS 7
1-LY11-1.5/120	1-LY13-1.5/120	1-LY1x-1.5/120	120	1.5	1.2	6.5	4.7	2.5	LS 7
1-LY11-3/120	1-LY13-3/120	1-LY1x-3/120	120	3	1.6	8.5	4.5	4	LS 7
1-LY11-3/120A		1-LY1x-3/120A	120	3	1.6	8.5	4.5	4	LS 7
1-LY11-6/120	1-LY13-6/120	1-LY1x-6/120	120	6	2.7	13	6	8	LS 5
1-LY11-6/120A		1-LY1x-6/120A	120	6	2.7	13	6	8	LS 5
1-LY11-10/120	1-LY13-10/120	1-LY1x-10/120	120	10	4.6	18.5	9.5	13	LS 5
1-LY11-10/120A		1-LY1x-10/120A	120	10	4.6	18.5	9.5	13	LS 5
1-LY11-1.5/350	1-LY13-1.5/350	1-LY1x-1.5/350(#)	350	1.5	1.2	5.7	4.7	4.5	LS 7
1-LY11-3/350	1-LY13-3/350	1-LY1x-3/350	350	3	1.6	8.5	4.5	7	LS 7
		1-LY1x-3/350A	350	3	1.6	8.5	4.5	7	LS 7
1-LY11-6/350	1-LY13-6/350	1-LY1x-6/350	350	6	2.8	13	6	13	LS 5
		1-LY1x-6/350A	350	6	2.8	13	6	13	LS 5
1-LY11-10/350		1-LY1x-10/350	350	10	5.0	18.5	9.5	23	LS 5
		1-LY1x-10/350A	350	10	5.0	18.5	9.5	23	LS 5

(*) Maximum excitation voltage for ferritic steel. For other temperature response matchings, the corresponding value is printed on the data sheet included with delivery.

(#) Types are only available with matching to aluminum, ferritic or austenitic steel

LY21

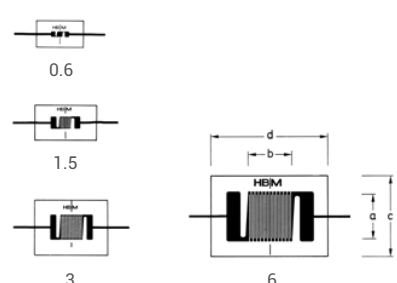
Linear strain gauge

Temperature response matched to steel
with $\alpha = 10.8 \cdot 10^{-6}/K$

LY2x

Temperature response matched to customer's choice
see page 16

Illustrations show actual size
(indicated: grid length in mm)

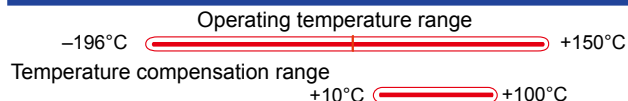


Contents per package: 10 pcs.

Steel	Aluminum	Other	Ω	Measuring grid		Meas. grid carrier		Maximum excitation voltage (*)	Sldr. terminals
				a	b	c	d		
				V					
1-LY21-0.6/120		1-LY2x-0.6/120(#)	120	0.6	0.6	3.5	6.4	1	LS 7
		1-LY2x-1.5/120	120	1.5	1.5	4.7	8.3	2	LS 5
1-LY21-3/120		1-LY2x-3/120	120	3	2.8	7.5	10	6	LS 5
		1-LY2x-6/120	120	6	6	11	16	12	LS 4

(*) Maximum excitation voltage for ferritic steel. For other temperature response matchings, the corresponding value is printed on the data sheet included with delivery.

(#) Types are only available with matching to aluminum, ferritic or austenitic steel



Suffix code for temperature compensation materials
-11: Mild steel ■ -17: Stainless steel ■ -23: Aluminium ■
For ordering, the above suffix code should be added to the basic gauge type.

FOIL STRAIN GAUGES

F Series



Applicable adhesives

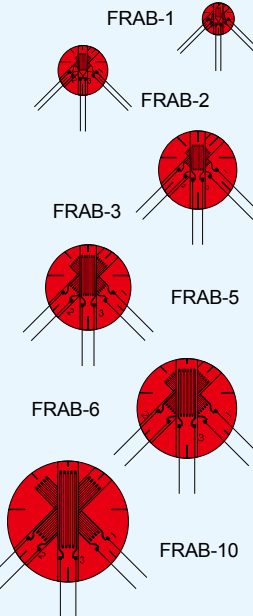
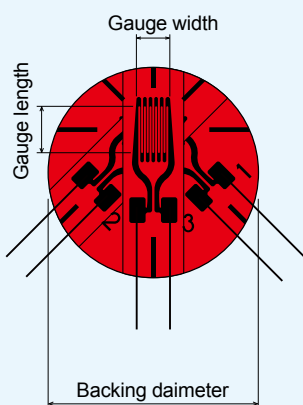
CN	-196 ~ +120°C
P-2	-30 ~ +150°C
EB-2	-60 ~ +150°C

GENERAL USE

Gauge pattern



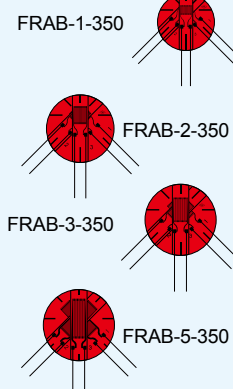
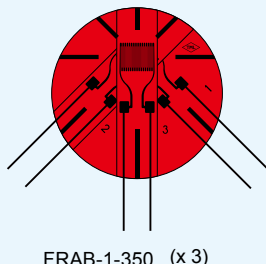
0°/45°/90° 3-element rosette stacked



Each package contains 10 gauges.

FRAB-1	1	0.7	φ 4.5	120
FRAB-2	2	0.9	φ 7	120
FRAB-3	3	1.7	φ 11	120
FRAB-5	5	1.9	φ 12	120
FRAB-6	6	2.4	φ 14	120
FRAB-10	10	2.5	φ 17	120

350Ω 0°/45°/90° 3-element rosette stacked



Each package contains 10 gauges.

FRAB-1-350	1	1.6	φ 8	350
FRAB-2-350	2	1.9	φ 9.5	350
FRAB-3-350	3	2	φ 10	350
FRAB-5-350	5	1.8	φ 10	350